Theory of Plastic and Elastic Properties of Graphite and Silicon Carbide

PhD Thesis

Savini Gianluca

Supervisors:
Prof. Giulio Pozzi

PhD Coordinator:
Prof. Fabio Ortolani

Dott. Pier Giorgio Merli
Prof. Malcolm I Heggie

Contents

Introduction

The mechanical properties describe the elastic and plastic properties under deformations.
Under small strains we have an elastic behaviour; the material returns to its original shape after the load is removed. In this regime the mechanical properties are full described by the elastic constants of the materials itself. Under larger strains we observe a plastic behaviour; the material deform permanently without breaking or rupturing. In this regime the material properties are determined by the nucleation and gliding of dislocations.
In this thesis I have proposed two novel theory on

1. Anomalously enhancement of the dislocation velocity in silicon carbide (SiC);

2. Mesoscale elasticity in graphite.

The first theory is a milestone on the road to implementing robust, high performance SiC devices. Despite the silicon carbide outstanding properties, several studies report a drawback: as soon as the device starts operating, dislocations become anomalously mobile and degrade electrical properties enormously.
It is remarkable to observe that up to now no theory has been able to explain these experimental results. In this study I have studied the dislocation dynamics in Silicon Carbide and I have proposed a new theoretical model which explains in detail all the experimental findings.
In particular I have shown why after the devices begin to operate, dislocations with dangling bonds along the cores become energetically favourable compared with fully bonded (reconstructed cores) and why only some types of dislocations are extremely mobile.

The second theory has profound implications for the new field of graphite/graphene science. First principles density functional calculations within the Local Density Approximation (LDA) have provided highly plausible results, but the folklore of interlayer interactions is that LDA does not include an important part of the

physical interaction between layers (the van der Waals interactions) and therefore should not be relied upon.
This belief is strengthened by the strong disagreement between theory and experiment on the elastic constant value C_{13} (positive for experiment studies, negative for theoretical studies). The sign of this elastic constant is crucial for the elastic properties of the material; a positive (negative) value of C_{13} means that under compression of the parameter lattice a_0, the parameter lattice c_0 tend, to expand (contract). Therefore theory and experiment describe graphite as a material with an opposite elastic behavior.
In this study I have shown that under deformation graphite tends to bend and these bending modes introduce a new class of elastic constants, the so-called *mesoscale elastic constants*.
Further I have demonstrated that LDA performs excellently for graphite and reproduces with precision the all elastic properties.

Outline
Chapter 1 will give a brief overview on density functional theory.
Chapter 2 will present the theory of the dislocation velocity in silicon carbide.
Chapter 3 will explain the mesoscale elasticity in graphite.

Chapter 1

Modeling the Crystal: Theoretical Background

1.1 Introduction

A crystal consist of a periodic array of atoms. An atom is made of a nucleus of charge Z, surrounded by a number of neutralizing electrons.
Core electrons occupy the filled inner shells of the atom and their main effect is screening the nuclear charges from the valence electrons. It is, therefore, tempting to eliminate them by replacing with an effective potential acting on valence electrons. This is the main idea behind the concept of *pseudopotentials*, which will be introduced and discussed in a forthcoming chapter of this thesis.
All the main material properties are due to the electrostatic or Coulombic interactions between valence electrons and nuclei of charge Z. Other interactions arising from the quantum-mechanical character of the electrons are also important. This is the case of *exchange* and *correlation effects*, which act like a glue and without which the atomic bonds are too weak to explain the solid state phase.
In this chapter I will give a brief overview of the theoretical background used in this thesis: the density functional theory (DFT).
This theory represents the most efficient way to tackle the quantum many-body problem and describe period systems or molecules with size up to 1000 atoms.

1.2 The many-body problem

The stationary state of a quantum-mechanical system with Hamiltonian $\widehat{H}$ may be described by the non-relativistic time-independent Schrödinger equation,

$$\widehat{H}\Psi = E\Psi \tag{1.1}$$

In the latter equation E is the eigenvalue or crystal energy and Ψ is the wavefunction describing the system,

$$\Psi \equiv \Psi\left(\mathbf{r}_1, \sigma_1; \mathbf{r}_2, \sigma_2; ..., \mathbf{r}_N, \sigma_N; \mathbf{R}_1, \mathbf{R}_2, ...\mathbf{R}_N\right) \tag{1.2}$$

where $\mathbf{r_i}$ and σ_i are the electron spatial and spin coordinates, while $\mathbf{R_i}$ is the nuclear coordinates of all the atoms in the system.
For a system of N electrons moving in a field of I nuclei of charge Z_α at sites $\mathbf{R}_\alpha$, the Hamiltonian becomes:

$$\begin{aligned} \widehat{H}(\mathbf{r}, \mathbf{R}) &= -\frac{1}{2}\sum_i \nabla_i^2 - \sum_\alpha \frac{1}{2M_\alpha}\nabla_\alpha^2 + \frac{1}{2}\sum_i \sum_{j\neq i} \frac{1}{|\mathbf{r_i} - \mathbf{r_j}|} \\ &+ \frac{1}{2}\sum_\alpha \sum_{\beta\neq\alpha} \frac{Z_\alpha Z_\beta}{|\mathbf{R}_\alpha - \mathbf{R}_\beta|} - \sum_i \sum_\alpha \frac{Z_\alpha}{|\mathbf{r_i} - \mathbf{R}_\alpha|} \end{aligned} \tag{1.3}$$

where all quantities herein are expressed in atomic units (Planck's constant $\hbar$, the electron charge e, the electron mass m and the vacuum permittivity relation $4\pi\varepsilon_0$ are sets to unity). In this coordinate system the unit length is defined with respect to the atomic Bohr radius ($1\,\text{a.u.} = 0.529\,\text{Å}$) and the energy with respect to Hartree ($27.211\,\text{eV}$).
A more simple way to write the latter Hamiltonian is

$$\widehat{H} = \widehat{T}_e + \widehat{T}_i + \widehat{V}_{e-e} + \widehat{V}_{i-i} + \widehat{V}_{e-i} \tag{1.4}$$

where:

$\widehat{T}_i$, $\widehat{V}_{i-i}$: are the kinetic and potential energy operators of the nuclei;
$\widehat{T}_e$, $\widehat{V}_{e-e}$: are the kinetic and potential energy operators of the electrons;
$\widehat{V}_{e-i}$: is the operator describing the interactions between electrons and nuclei.

Using the full Hamiltonian (equation 1.3) the Schrödinger equation contains $3(Z+1)n$ variables, where n is the number of atoms in the crystal. Since $1\,\text{cm}^3$ of crystalline material contains about $5 \cdot 10^{22}$ atoms, even for a light element like carbon ($Z = 6$), the number of variables involved is $\sim 2 \cdot 10^{24}$ per cm^3.
Nowadays, solve this eigenvalue problem is impossible for any system larger than a single hydrogen atom and some approximations must be made. In the next section I describe the simplest one, the Born-Oppenheimer approximation, where the motion of electrons and nuclei are decoupled, inspired by their large difference in masses.

1.3 The Born-Oppenheimer approximation

The adiabatic approximation or the Born-Oppenheimer approximation is due to the small ratio between the masses of nuclei M and electrons m ($\sim 10^{-5}$). It is reasonable to assume that the nuclei (heavy) do not follow the motion of every electron (light), but move only in the averaged field of all the electrons while the electrons move on a much faster time-scale than the nuclei.
If we neglect the kinetic energy of the nuclei, the Hamiltonian becomes:

$$\widehat{H}_e = \widehat{T}_e + \widehat{V}_{e-e} + \widehat{V}_{i-i} + \widehat{V}_{e-i} \tag{1.5}$$

with the associated eigenfunction $\psi(\mathbf{r}, \mathbf{R})$ satisfying

$$\widehat{H}_e \psi(\mathbf{r}, \mathbf{R}) = E_e(\mathbf{R}) \psi(\mathbf{r}, \mathbf{R}) \tag{1.6}$$

In this equation, $\widehat{H}_e$ is the total Hamiltonian in the limit $M \to \infty$, and it is usually called electronic Hamiltonian. The eigenvalue $E_e(\mathbf{R})$ is the energy of the electrons in the field of frozen nuclei. Analytically:

$$E_e(\mathbf{R}) = \int \psi^*(\mathbf{r}, \mathbf{R}) \widehat{H}_e \psi(\mathbf{r}, \mathbf{R}) d\mathbf{r} \tag{1.7}$$

Within the Born-Oppenheimer approximation the term $\widehat{V}_{i-i}$ becomes a simple additive constant of the Hamiltonian $\widehat{H}_e$ and the eigenvalue $E_e(\mathbf{R})$. Then the total Hamiltonian can be written as:

$$\widehat{H} = \widehat{H}_e - \widehat{H}_n = \widehat{H}_e - \sum_\alpha \frac{1}{2M_\alpha} \nabla_\alpha^2 + \widehat{V}_{i-i} \tag{1.8}$$

where the term $\widehat{H}_n$ is the nuclear Hamiltonian. As the ratio $m/M_\alpha$is small, Born and Oppenheimer have shown that $\widehat{H}_n$ can be treated as a small perturbation. In the zero-order Born-Oppenheimer approximation the electrons move in the Coulombian potential field of fixed nuclei and we can therefore decompose the total wavefunction as

$$\Psi(\mathbf{r}, \mathbf{R}) = \Psi_R(\mathbf{r}) \cdot \chi(\mathbf{R}) \tag{1.9}$$

where $\chi(\mathbf{R})$ depends only on the nuclear coordinate R, while $\Psi(\mathbf{r}, \mathbf{R})$ is the solution of the electronic Hamiltonian $\widehat{H}_e$ (equation 1.5).
Replacing the total wavefunction $\Psi(\mathbf{r}, \mathbf{R})$ into the Schrödinger equation 1.1

we obtain:

$$\left\{\sum_{\alpha}\frac{1}{2M_{\alpha}}\nabla_{\alpha}^{2}\chi(\mathbf{R})+E_{e}(\mathbf{R})\chi(\mathbf{R})+\widehat{V}_{i-i}\chi(\mathbf{R})-E(\mathbf{R})\chi(\mathbf{R})\right\}\Psi_{R}(\mathbf{r})$$
$$=\sum_{\alpha}\frac{1}{2M_{\alpha}}\left[\chi(\mathbf{R})\nabla_{\alpha}^{2}\Psi_{R}(\mathbf{r})+2\nabla_{\alpha}\chi(\mathbf{R})\cdot\nabla_{\alpha}\Psi_{R}(\mathbf{r})\right] \quad (1.10)$$

multiplying all the terms by $\Psi_{R}^{*}(\mathbf{r})$ and integrating over all electronic coordinates, we have

$$\left\{\sum_{\alpha}\frac{1}{2M_{\alpha}}\nabla_{\alpha}^{2}+E_{e}(\mathbf{R})+\widehat{V}_{i-i}-E(\mathbf{R})\right\}\chi(\mathbf{R})=$$
$$+\sum_{\alpha}\frac{1}{2M_{\alpha}}\chi(\mathbf{R})\int\Psi_{R}^{*}(\mathbf{r})\nabla_{\alpha}^{2}\Psi_{R}(\mathbf{r})d(\mathbf{r}) \quad (1.11)$$
$$+\sum_{\alpha}\frac{1}{M_{\alpha}}\nabla_{\alpha}\chi(\mathbf{R})\int\Psi_{R}^{*}(\mathbf{r})\nabla_{\alpha}\Psi_{R}(\mathbf{r})d\mathbf{r}$$

Bohr and Oppenheimer (1925) have shown that by neglecting the last two terms of the equation 1.11, we introduce an error in the total energy E not larger than the square root of the masses ratio m/M.
It is important to note that the Bohr-Oppenheimer approximation breaks down for Jahn-Teller systems [6] or more in general when a coupling between electrons and nuclear orbitals occurs. Such even is usually known as a *vibronic* state or in some special case Cooper pair [7].

1.4 Hartree Theory

Using the adiabatic approximation the many-electron wavefunction $\psi(\mathbf{r},\mathbf{R})$ is the solution of the following eigenvalue equation:

$$\left\{\widehat{T}_{e}+\widehat{V}_{e-e}+\widehat{V}_{e-i}\right\}\psi(\mathbf{r},\mathbf{R})=E_{e}(\mathbf{R})\psi(\mathbf{r},\mathbf{R}) \quad (1.12)$$

if the electrons are noninteracting particles ($\widehat{V}_{e-e}=0$), the latter equation can be decoupled in N single-electron equations.
Therefore, it is expedient to study a system of noninteracting particles and try to include the electron-electron term as a correction. This problem has been solved with the introduction of the so-called *autoconsisten electronic field* (Hartree, 1928).

In this approximation the potential V_{e-e} is rewritten as an effective potential of single electron $V^H(\mathbf{r}_i)$ which is the electronic mean field due by all the other electrons,

$$V^H(\mathbf{r}_i) = \sum_{j \neq i}^{N} \int \frac{|\phi_j(\mathbf{r}_j)|^2}{|\mathbf{r}_i - \mathbf{r}_j|} d\mathbf{r}_j = \sum_{j \neq i}^{N} \int \frac{n(\mathbf{r}_j)}{|\mathbf{r}_i - \mathbf{r}_j|} d\mathbf{r}_j \tag{1.13}$$

The single electron Hamiltonian $\widehat{h}_H$can be written as

$$\widehat{h}_H = -\frac{1}{2}\nabla_i^2 + V_{eff}\left(\mathbf{r}_i\right) \tag{1.14}$$

with

$$V_{eff}\left(\mathbf{r}_i\right) = \sum_{\alpha} \frac{Z_\alpha}{|\mathbf{r}_i - \mathbf{R}_\alpha|} + V^H\left(\mathbf{r}_i\right) \tag{1.15}$$

Then the Hartree equations are determinated imposing that the total wavefunctions is the product of the one electron wavefunction, $\phi_\lambda(\mathbf{r})$, each of them subject on its own effective potential.

$$\Psi\left(\mathbf{r}_1 s_1, \ldots, \mathbf{r}_N s_N\right) = \phi_1\left(\mathbf{r}_1 s_1\right) \ldots \phi_N\left(\mathbf{r}_N s_N\right) = \prod_{i=1}^{N} \phi_i\left(\mathbf{r_i} s_i\right) \tag{1.16}$$

and the N single-electron Schrödinger equations for each one electron wavefunction, $\phi_\lambda(\mathbf{r})$ become:

$$\left(-\frac{1}{2}\nabla^2 + V_{eff}\left(\mathbf{r}\right)\right)\phi_i\left(\mathbf{r}\right) = \varepsilon_i \phi_i\left(\mathbf{r}\right) \tag{1.17}$$

these equations are called the autoconsisten Hartree equations. The total energy of the system is then the sum of the respective one electron eigenvalues,

$$E_e = \sum_{i=1}^{N} \varepsilon_i \tag{1.18}$$

The first application of the autoconsisten Hartree equations 1.17 is due to Slater (1930). The main and more obvious lack of the Hartree theory is the Pauli exclusion principle (the single electron functions $\Psi(\mathbf{r})$ must be antisymmetric with respect to the exchange of two particles). Consequently this model neglects the exchange effect due to the interaction of two electrons with the same spin (see section 1.5).

In particular, if we apply the Hartree theory to the *jellium* model[1], the solutions of the autoconsisten Hartree equations are the simple one electron wavefunctions. In this case, the effective potential of single electron $V^H(\mathbf{r}_i)$ is equal with opposite sign to the uniform nuclei potential ($V_{eff}(\mathbf{r}_i) = 0$); therefore the Hartree theory degenerate in the simple Sommerfeld model (noninteracting electron gas).

1.5 Hartree-Fock Theory

The Pauli exclusion principle was implement in the Hartree theory by Fock (1930). In order to take into account this principle, the product of the single electron eigenfunction have to be antisymmetric with respect to the exchange of two electrons. A convenient way to express this anti-symmetrised product of the one electron wavefunctions $\phi_i(\mathbf{r})$ is the Slater determinant (Slater, 1920),

$$\Psi(\mathbf{r}) = \frac{1}{\sqrt{N!}} \begin{vmatrix} \phi_1(\mathbf{r}_1) & \phi_1(\mathbf{r}_2) & \dots & \phi_1(\mathbf{r}_N) \\ \phi_2(\mathbf{r}_1) & \phi_2(\mathbf{r}_2) & \dots & \phi_2(\mathbf{r}_N) \\ \vdots & & & \vdots \\ \phi_N(\mathbf{r}_1) & \phi_N(\mathbf{r}_2) & \dots & \phi_N(\mathbf{r}_N) \end{vmatrix} = \frac{1}{\sqrt{N!}} det\left|\phi_\lambda(\mathbf{r}_\mu)\right| \tag{1.19}$$

with

$$\phi_\lambda(\mathbf{r}) = \phi_i(\mathbf{r})\ \chi_\sigma \quad \text{e} \quad \begin{cases} \sum_s \chi^*_\alpha \chi_\beta = \delta_{\alpha\beta} \\ \\ \int \phi^*_i(\mathbf{r})\,\phi_j(\mathbf{r})\,d\mathbf{r} = \delta_{ij} \end{cases} \tag{1.20}$$

where χ_α is the spin wavefunction, with elements $\alpha = \binom{1}{0}$ for spin-up and $\beta = \binom{0}{1}$ for spin-down while $\phi_i(\mathbf{r})$ is the orbital wavefunction.
The determinant is guaranteed to be anti-symmetric since exchanging two of the single electron spin-orbitals will change $\Psi_{HF}(\mathbf{r})$by a factor -1 while the presence of two identical spin-orbitals will result in $\Psi_{HF}(\mathbf{r}) = 0$.
Using the wavefunction $\Psi_{HF}(\mathbf{r})$ the expectation value of the Hamiltonian is:

$$E_{HF} = \sum_{i=1}^{N} h_i + \frac{1}{2}\sum_{i,j=1}^{N}(J_{ij} - K_{ij}) \tag{1.21}$$

where:

[1] In the *jellium* model, the ionic lattice is described as a uniform and homogeneous distribution of positive charge. For this reason is also called Thomson model for solid.

$$h_i = \int \psi_i^* (\mathbf{x}) \left[-\frac{1}{2} \bigtriangledown_i^2 - \sum_{\alpha=1}^{N} \frac{Z_\alpha}{|\mathbf{r_i} - \mathbf{R}_\alpha|} \right] \psi_i (x)\, dx = \langle i | \, T_e + V_{e-n} \, | i \rangle \quad (1.22)$$

$$J_{ij} = \iint \psi_i^* (\mathbf{x})\, \psi_j^* (\mathbf{x}') \frac{1}{|\mathbf{x} - \mathbf{x}'|} \psi_i (\mathbf{x})\, \psi_j (\mathbf{x}')\, d\mathbf{x}\, d\mathbf{x}' = \langle ij | \, V_{e-e} \, | ij \rangle \quad (1.23)$$

$$K_{ij} = \iint \psi_i^* (\mathbf{x})\, \psi_j^* (\mathbf{x}') \frac{1}{|\mathbf{x} - \mathbf{x}'|} \psi_j (\mathbf{x})\, \psi_i (\mathbf{x}')\, d\mathbf{x}\, d\mathbf{x}' = \langle ij | \, V_{e-e} \, | ji \rangle \quad (1.24)$$

The first term h_i is the single-electron matrix element corresponding to the kinetic and electron-nuclei interaction terms. The second and third terms are usually called direct $J_{\lambda\mu}$ and exchange integrals $K_{\lambda\mu}$ and they represent the electron-electron interaction [7]. In the second quantization formalism, it has been shown that the direct term $J_{\lambda\mu}$ is originated by the creation and annihilation of one electron with same quantum state, while the exchange term $K_{\lambda\mu}$ is due to the swap of two electron with the same spin.
The exchange energy term can be rewritten as

$$E_x = \frac{1}{2} \sum_{\lambda,\mu} \delta_{\sigma_\lambda \sigma_\mu} \delta_{\sigma_\mu \sigma_\rho} \int \int \phi_\lambda^* (\mathbf{r})\, \phi_\tau^* (\mathbf{r}') \frac{1}{|\mathbf{r} - \mathbf{r}'|} \phi_\mu (\mathbf{r})\, \phi_\rho (\mathbf{r}')\, d\mathbf{r} d\mathbf{r}' \quad (1.25)$$

where the Kronecker delta $\delta_{\sigma_\lambda \sigma_\mu}$ensures that the matrix is diagonal (elements with different spins are zero).
The physical meaning of the exchange energy E_x is due to the condition that two electrons with parallel spins cannot be found at the same point in space. As a consequence, the average distance separating the two electrons will be greater lowering the electrostatic repulsion energy by a quantity corresponding to the exchange term. The exchange integral $K_{\lambda\mu}$, has no classical counterpart and should be regarded as a quantum mechanical correction to the Coulomb integral $J_{\lambda\mu}$.
The total energy of the system can be rewritten as

$$E = -\frac{1}{2} \sum_{\lambda} \int \phi_\lambda^* (\mathbf{r})\, \nabla^2 \phi_\lambda (\mathbf{r})\, d\mathbf{r} + \int n (\mathbf{r})\, V_{e-i} d\mathbf{r} + E_H + E_x \quad (1.26)$$

with

$$E_H = \frac{1}{2} \int \frac{n (\mathbf{r}_1)\, n (\mathbf{r}_2)}{|\mathbf{r}_1 - \mathbf{r}_2|} d\mathbf{r}_1 d\mathbf{r}_2 \quad (1.27)$$

The ground state ψ_λ is found applying the variational principle to the 1.26

equation (note that the eigenvalues ψ_λ are orthogonal) using the Lagrange multiplicator $E_{\lambda\mu}$

$$E - \sum_{\lambda\neq\mu} E_{\lambda\mu} \int \psi_\lambda^* \psi_\mu d\mathbf{r} - \sum_\lambda E_\lambda \left\{ \sum_s \int |\psi_\lambda|^2 \, d\mathbf{r} - 1 \right\} \tag{1.28}$$

this equation is minimized with respect to the ψ_λ^*, E_λ, and $E_{\lambda\mu}$ variables. Then rewriting the equation 1.26, we obtain the Hartree-Fock equation for each orbital λ:

$$\left\{ -\frac{1}{2}\nabla^2 + \widehat{V}_{e-i}(\mathbf{r}) + \widehat{V}^H(\mathbf{r}) + \widehat{V}_\lambda^x(\mathbf{r}) - E_\lambda \right\} \psi_\lambda(\mathbf{r}) = \sum_{\lambda\neq\mu} E_{\lambda\mu} \psi_\mu(\mathbf{r}) \tag{1.29}$$

with

$$\widehat{V}^H(\mathbf{r})\,\psi_\lambda(\mathbf{r}) = \frac{\partial E_H}{\partial \psi_\lambda^*} = \int \frac{n(\mathbf{r}_1)\,\psi_\lambda(\mathbf{r})}{|\mathbf{r}-\mathbf{r}_1|} d\mathbf{r}_1 \tag{1.30}$$

$$\widehat{V}_\lambda^x(\mathbf{r})\,\psi_\lambda(\mathbf{r}) = \frac{\partial E_H}{\partial \psi_\lambda^*} = -\sum_\mu \int \psi_\mu^*(\mathbf{r}_1)\,\psi_\lambda(\mathbf{r}_1)\,\frac{1}{|\mathbf{r}-\mathbf{r}_1|}\psi_\mu(\mathbf{r}_1)\,d(\mathbf{r}_1) \tag{1.31}$$

where $\widehat{V}^H$, $\widehat{V}_\lambda^x$ are the Hartree and exchange potentials. Diagonalizing the equation 1.29 the Lagrange multiplicator $E_{\lambda\mu}$ is removed and the equations are solved in an autoconsisten way. The total energy of the system E_{tot} is determinated multiplying the equation 1.29 per $\psi_\lambda^*(\mathbf{r})$ and integrating over $\mathbf{r}$ for all the occupied level λ,

$$E_{tot} = \sum_\lambda E_\lambda - E_H - E_x + E_{i-i} \tag{1.32}$$

where E_λ is the eigenvalue of the HF equations.
The HF equations are solved in an autoconsisten way. First we start from an arbitrary sets of wavefunction ϕ_λ, usually the wavefunction of the single atoms (the Sommerfeld solutions). From the chosen wavefunction we calculate the Hartree and the exchange potential, and from them we solve the HF equations obtaining a new sets of wavefunctions ϕ_λ. This loop is repeated until the initial wavefunctions are equal to the final wavefunctions within an chosen tolerance. The way to solve the HF equations is called autoconsisten loop.

Discussion

This theory has been applied to several atomic systems, with a relative small number of atoms.
In general, comparing the HF results to the respective experimental data, we found that the lattice parameters and the total energy are underestimated, while the normal vibrational modes and the forbidden band gap are overestimate.
This theory neglected the correlation effect between electrons, *i.e.* the probability distribution of the electrons are independed between themself.
The latter neglection has disastrous consequences for several atomic systems. For instance, the HF theory does not predict the bounded state of fluorine molecule F_2, and when applied to the uniform and homogeneous electron gas (jellium approximation), the HF theory predicts a zero density of states at the Fermi energy (non-conductor behavior material). The latter results suggest that also simple metal systems are not well described by the Hartree-Fock theory.
Several efforts have been done in order to include the correlation effects in the HF model. The simplest way to compensate the correlation effects is to include an empirical correction term in order to reproduce some experimental data like the ionization energies and/or heat of formation of molecules. Using this approach we may be able to describe correctly some systems but we obviously lose the transferability and the *beauty* of a real *ab-initio* theoretical method. A better approach is the so called *configuration interaction* (CI) method, where the total wavefunction is builded as a linear combination of different Slater determinants. Although in principle the latter method describes the real eigenfunction of the system, the computational time required is often too large to describe even small systems (the required computational time is increasing as N^4, *i.e.* doubling the number of atoms N the computational time become 16 time longer). Nevertheless, the CI method applied to the HF theory is often used as a *benchmark* for other theoretical approaches based on density functional theory (Briddon *et al.* [85]).

1.6 The Thomas and Fermi model

Thomas (1927) e Fermi (1928) proposed a new scheme based on the electron density of the system, $n(\mathbf{r})$. This original idea is remarkable in the sense that it allows us to replace the complicate N-electron wavefunction $\Psi_{HF}(\mathbf{r})$ with the simpler electron density $n(\mathbf{r})$.

This model assumes that the electronic properties of a real system are similar to those of a non-interacting fermions gas, *i.e.* a classical ensemble of non-correlated electrons. Although this approach has had a limited success in reproducing the properties of atomic systems, the Thomas Fermi (TF) theory represents the first prototype of the density functional theory (both theories focus on $n(\mathbf{r})$, the electronic density quantity).
The general Hamiltonian of any atomic system can be written as:

$$\widehat{H} = -\frac{1}{2}\sum_i \nabla_i^2 + \frac{1}{2}\sum_{j\neq i}\frac{1}{|\mathbf{r}_i - \mathbf{r}_j|} + \sum_i v(\mathbf{r}_i) \tag{1.33}$$

with

$$v(\mathbf{r_i}) = -\sum_\alpha \frac{Z_\alpha}{|\mathbf{r}_i - \mathbf{R}_\alpha|} \tag{1.34}$$

where $v(\mathbf{r}_i)$ is so-called external potential due to the interaction between the electrons and the nuclear frame.
In the Thomas and Fermi approximation, the electron-electron interaction term V_{e-e} is assumed to be due to the merely Coulombic interactions between electrons. The latter term expressed with respect to the electron charge $n(\mathbf{r})$ becomes the found Hartree potential,

$$U_H[n] = \frac{1}{2}\int\int \frac{n(\mathbf{r})\, n(\mathbf{r}')}{|\mathbf{r} - \mathbf{r}'|} d\mathbf{r} d\mathbf{r}' \tag{1.35}$$

The kinetic energy is given by

$$T[n] = \int t[n(\mathbf{r})]\, d\mathbf{r} \tag{1.36}$$

where $t[n(\mathbf{r})]$ is the kinetic energy density for a system of non-interacting electrons with density $n(\mathbf{r})$.
Then the kinetic energy density is derived from the respective value of a homogeneous non-interacting degenerate electron gas ($T = 0$),

$$t = \frac{8\pi}{5}\left(\frac{2m}{h^2}\right)^{\frac{3}{2}} \varepsilon_F^{\frac{5}{2}} \tag{1.37}$$

where ε is

$$n = \frac{4\pi}{3}\left(\frac{2m\varepsilon_F}{h^2}\right)^{\frac{3}{2}} \qquad \longrightarrow \qquad \varepsilon_F = \frac{h^2}{2m}\left(\frac{3n}{8\pi}\right)^{\frac{5}{3}} \tag{1.38}$$

Using the latter equations and rewriting we obtain the Thomas-Fermi ki-

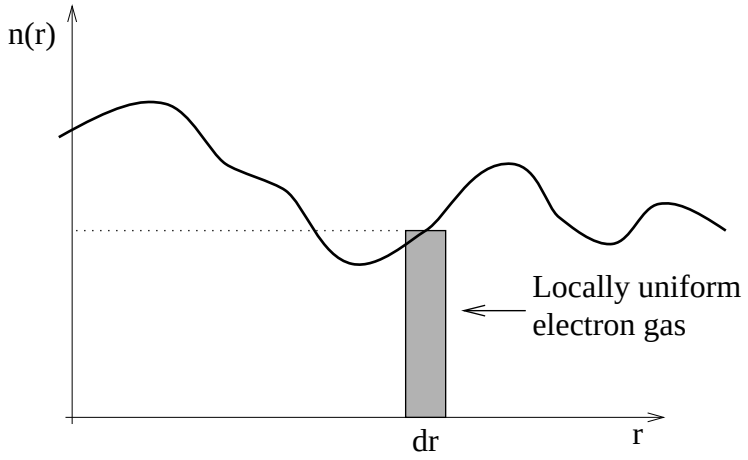

Figure 1.1: *Local density approximation* in the Thomas-Fermi model. For each infinitesimal space region $d\mathbf{r}$, the electron density $n(r)$ of the system is assumed to be equal to the electron density of a homogeneous non-interacting electron gas.

netic energy functional determined with respect to the density $n(r)$,

$$T_0[n] = \frac{3\hbar^2}{10m}\left(3\pi^2\right)^{\frac{2}{3}} \int n(\mathbf{r})^{\frac{5}{3}}\, d\mathbf{r} = C_F \int n(\mathbf{r})^{\frac{5}{3}}\, d\mathbf{r} \tag{1.39}$$

in the atomic unit system the constants C_F is $\frac{3}{10}\left(3\pi^2\right)^{\frac{2}{3}} = 2.871$.
Equation 1.39 is the famous TF kinetic energy functional which Thomas and Fermi dared to apply to electrons in atoms and molecules. Here, we first encounter one of the main important idea in modern DFT: the local density approximation (LDA, see section **??**). In this approximation, electronic properties are determined as functional of the electron density by applying, locally, the respective relations of a homogeneous non-interacting electronic system.
The total electronic energy, $E_{TF}[n, v]$, can now be written as

$$E_{TF}[n, v] = \int v(\mathbf{r})\, n(\mathbf{r})\, d\mathbf{r} + U_H(\mathbf{r}) + C_F \int n(\mathbf{r})^{\frac{5}{3}}\, d\mathbf{r} \tag{1.40}$$

It is important to note that $E_{TF}[n, v]$ is a functional of the external potential $v(\mathbf{r})$ as well as of the electronic density $n(\mathbf{r})$, but does not contain any exchange or correlation terms.
Imposing that the total number of electrons remains constant, the ground-

state density $n(\mathbf{r})$ is determinated by minimizing the equation 1.40 by solving the following Euler-Lagrange equation,

$$\delta\left\{E_{TF}[n,v]-\mu\int n(\mathbf{r})\,d\mathbf{r}\right\}=0 \tag{1.41}$$

where μ is a Lagrange multiplicator playing the role of the chemical potential. This is evident from the form of the variational equation,

$$\delta\left\{E_{TF}[n,v]-\mu N\right\}=0 \qquad \Rightarrow \qquad \mu=\frac{\delta E_{TF}}{\delta N} \tag{1.42}$$

The solution of the Euler-Lagrange equation can be written as:

$$n(\mathbf{r})=\frac{1}{3\pi^2}\left\{2\left[\mu-v_{eff}(\mathbf{r})\right]\right\}^{\frac{3}{2}} \tag{1.43}$$

$$v_{eff}(\mathbf{r})=v(\mathbf{r})+\int\frac{n(\mathbf{r}')}{|\mathbf{r}-\mathbf{r}'|}d\mathbf{r}' \tag{1.44}$$

The latter two equations are called autoconsisten Thomas-Fermi equations. The form of the above equation reveals the attractiveness of the TF model. It allows the determination of $n(r)$ directly from $v(r)$, by-passing the total wavefunction. This is the main achievement of this theory. Of course, the choice of $v(r)$ remains problematic.

Discussion

Although the Thomas-Fermi method suffers from a crude treatment of the kinetic energy (neglecting of exchange energy), this theory contains the two main ideas of the density functional theory (DFT):

- The quantum-mechanical system is described by the electron density $n(\mathbf{r})$,
- *local density approximation* (LDA); electronic properties are determined as a functional of electron density of a simple homogeneous electronic gas system.

This method has been found to give a rough estimative of the real charge density and the electrostatic potential (with respect to HF and DFT based method). Further, the charge density is infinite at the nucleus, and it does not decade exponentially far from the nucleus, but as r^{-6} (Gross *et al* [7]). Another weakness of the TF theory is the lack of atom shell structures,

in other word the observed periodic variation with respect to the atomic number Z is not reproduced; this method predict that the atoms shrink with increasing atomic number Z (Gunnarsson *et al.* [9, 10]).

1.7 Density Functional Theory (DFT)

In DFT, the electron density distribution rather than the many electron wavefunction plays the central role. The essence of the theory is set up in two pioneering papers by Hohenberg and Kohn in 1964 and by Kohn and Sham in 1965. The first proves that the electron charge density, $n(\vec{r})$, uniquely characterises the ground state of a system as exactly and completely as the wavefunction. This is the so-called "basic lemma of Hohenberg-Kohn".
One of the great advantages of this approach is practicality. DFT methods do not handle the two-electron interactions explicitly but rather allow for them using properties of the one-electron density. The system of N atoms, which was a $4N$ variable problem, is reduced to a 3 variable problem. This leads to lower computational cost and therefore a wider range of applicability.
However, it should be pointed out that DFT is a ground state theory. The unnoccupied states are poorly represented and therefore this theory often fails in excited state description and band gap prediction.
In the second paper, a set of self-consistent equations are described in order to solve the many-body problem:

$$\left[-\frac{1}{2}\bigtriangledown^2 + V_{electron-ion} + e^2\int\frac{n(\vec{r'})}{\left|\vec{r}-\vec{r'}\right|}d\vec{r'} + V_{XC}(\vec{r})\right]\psi_i(\vec{r}) = E_i\psi_i(\vec{r}) \quad (1.45)$$

$$n(\vec{r}) = \sum_i^n |\psi_i(\vec{r})|^2 \quad (1.46)$$

$$V_{XC}(\vec{r}) = \frac{\delta E_{XC}[n(\vec{r})]}{\delta n(\vec{r})} \quad (1.47)$$

The equations 1.45, 1.46 and 1.47 are commonly known as the Kohn-Sham equations. They provide an efficient method to minimize the energy with respect to electron density. Solution of the Kohn-Sham equations is based on the variational principle: the correct value of the charge density, $n(\vec{r})$, is the one which gives the minimum energy of the system.
Further approximations are needed in order to give an expression for the

exchange correlation potential. $E_{XC}[n(\vec{r})]$ and $V_{XC}[\vec{r}]$ are the exchange correlation energy and potential, respectively. The main approximations are the Local Density Approximation (LDA) and the Generalised Gradient Approximation (GGA).

1.8 Local Density Approximation (LDA) and Generalised Gradient Approximation (GGA)

Both LDA and GGA use the exchange correlation energy of an homogeneous electron gas to give a tractable expression for the exchange correlation potential of a real system.
In the LDA, the exchange-correlation energy at point $\vec{r}$, $\varepsilon_{XC}[n(\vec{r})]$, is taken equal to the the exchange-correlation energy of an homogeneous electron gas with the same electron density n. The expression for the exchange-correlation energy takes the form:

$$E_{XC}^{LDA}[n] = \int n(\vec{r}) \left[\varepsilon_X^{hom}[n(\vec{r})] + \varepsilon_C^{hom}[n(\vec{r})]\right] d\vec{r} \tag{1.48}$$

where $\varepsilon_X^{hom}[n(\vec{r})]$ and $\varepsilon_C^{hom}[n(\vec{r})]$ are the exchange and the correlation energy terms, respectively, of an homogeneous electron gas of density n.
The approximation to a homogeneous gas represents only a mathematical model, since in all real systems the electronic density is nonuniform. This approach might not properly account for the fact that the charge density in a solid varies spatially . However, this approximation has proved to give very useful results.
The GGA was developed in order to take better into account the nonuniform electronic density of real systems. The exchange correlation energy in the GGA includes terms which depend not only on the electron density but also on its spatial derivative. The expression for the exchange correlation energy takes the form:

$$E_{XC}^{GGA}[n] = \int n(\vec{r}) \varepsilon_X^{hom}[n(\vec{r})] F_{XC}[n(\vec{r}), |\bigtriangledown n(\vec{r})|, ...] d\vec{r} \tag{1.49}$$

where F_{XC} is dimensionless and $\varepsilon_x^{hom}[n(\vec{r})]$ is the exchange energy term of an homogeneous electron gas of density n.
It should be noted that these two approaches fail in describing long range electron-electron interactions such as Van der Waals.

1.9 Pseudopotentials

Electrons in a system can be divided into core and valence electrons. Core electrons are strongly bound to the nuclei and do not play a part in the bonding. Valence electrons form chemical bonds and they govern the properties of the material. Therefore, the Schrödinger equation can be further reduced by incorporating core electrons into the potential of the nuclei to form an effective core potential, a so called pseudopotential.
The pseudopotentials are constructed in such a way that they reproduce the exact all-electron wavefunction at distance from the nucleus greater than a cut-off radius, r_c. Between the nucleus and the cut-off radius the true all-electron wavefunction varies rapidly with many nodes and requires a large number of fitting functions to model accurately. The pseudopotential replaces this core wavefunction by a smooth nodeless function which is easy to represent numerically. Hence, the corresponding pseudo-wavefunctions are equal to the true wavefunctions outside the core region. The integrated charge density inside r_c for the pseudo-wavefunction and the true wavefunction agrees. This is known as norm conservation. This is important because it insures that the total charge in the core region is correct and that the normalized pseudo-orbital is equal to the true orbital outside of r_c.
The radius of the core region determines the quality of the pseudopotential. Large r_c results in quicker calculations but low accuracy. Reducing r_c increases the accuracy of the potential. The core radius is usually chosen to be about half-way between the outermost node and the outermost extremum of the all-electron wavefunction.
There are three types of pseudopotentials implemented in AIMPRO: Bachelet, Hamann and Schlüter (BHS) type, Troullier and Martins (TM) type and Hartwigsen, Goedecker and Hutter (HGH) type [86].

1.10 Basis sets

Since the core electrons have been included in the pseudopotentials, the wavefunction will only include the valence electrons. The valence electron wavefunction, $\psi_\lambda(r)$, must be expanded in terms of the basis set $\phi_i(r)$:

$$\psi_\lambda(r) = \sum_i c_i^\lambda \phi_i(r)$$

where c_i^λ are the expansion coefficients. Usually, the basis set functions are

plane-waves, Slater type or Gaussian type orbitals.
Plane waves have the general form $\exp(i\vec{G}\vec{r})$, where $\vec{r}$ is the position vector and $\vec{G}$ is the propagation vector. Their use is equivalent to making a Fourier transform of the wavefunction. These functions are orthogonal, and the basis functions are not centred on atoms. They are therefore independent of the atom positions and do not bias the distribution of charge density. By including additional plane waves, the quality of the basis set is improved. However, this increases the computational cost.
Slater type atomic orbitals (STO) have exponential radial parts analogous to the hydrogen atom in the form $\exp(-r)$. The one- and two-electron integrals can be evaluated analytically in the two centre case. However, great difficulties were encountered for the 3 and 4-centre cases. Gaussian-type orbitals have the form $\exp(-r^2)$. They have the advantage that they can be evaluated analytically. A single Gaussian function poorly represents atomic orbitals but larger numbers of them can be used for a more accurate description. Gaussian orbitals are localised, *i.e.* the centres of the functions are placed at the nuclei and sometimes also at bond centres. Bond-centred Gaussians can improve the description of high-order angular momentum functions like *d*- orbitals for carbon and *p*-orbitals for hydrogen.
The basis set expansion in AIMPRO is done in the form of localised Gausssians in the following form:

$$\phi_i(r) = (x - R_{ix})^{n_1}(y - R_{iy})^{n_2}(z - R_{iz})^{n_3} e^{-\alpha_i(r-R_i)^2}$$

where n_1, n_2 and n_3 are integers which determine the symmetry of the orbitals. The choice of n_1, n_2 and n_3 sets the orbital type; $n_1 = n_2 = n_3 = 0$ gives spherically symmetric *s*-orbitals, setting one of n_1, n_2 or n_3 =1 gives *p*-orbitals in the *x*, *y or z* directions respectively, while setting $\sum_i n_i = 2$ produces a combination of five *d*- and one *s*-orbital.
The advantage of Gaussian orbitals over plane waves is that a small number of basis functions is required -in this thesis normally 4 radial functions are used. In the case of atoms such as oxygen, additional radial functions can be added to the oxygen atom without changing the basis set of the other atoms. The integration of Gaussian orbitals in calculations of electron-electron interaction can be performed analytically.

1.11 k-point sampling of the Brillouin zone

When periodic boundary conditions are used, the Kohn-Sham equations are usually solved in the reciprocal space, or $k-$space. The reciprocal space is a mathematical construction orthogonal to the real space. The reciprocal space of a real space of lattice vectors $\vec{a}_1$, $\vec{a}_2$ and $\vec{a_3}$ is built on the basis of the vectors $\vec{b_1}$, $\vec{b_2}$ and $\vec{b_3}$, where $\vec{a}_i \cdot \vec{b}_j = 2\pi\delta_{ij}$, δ_{ij} is the Kronecker delta function.
The wavefunction of a free electron is a travelling wave associated with a certain value of the wavevector k:

$$\psi_k \propto e^{i\vec{k}\cdot\vec{r}}$$

The value of k describes the periodicity of the wavefunction. The energy $E(k)$ of a free electron is also uniquely determined by k: $E(k) \propto k^2$. The whole range of possible wavevectors $\vec{k}$ forms the $k-$space.
In the case of a crystal, the wavefunction must reflect the periodicity of the crystal and it takes the form:

$$\psi_k(r) = u_k(r) \cdot e^{i\vec{k}\cdot\vec{r}}$$

where $u_k(r)$ is a function with the periodicity of the crystal.
The plot of the $E(k)$ as function of k is called the band structure. It is not single valued, so bands have an index m.
The region of reciprocal space where all eigenstates of an electron are unique is called the Brillouin zone (BZ) and its shape depends on the symmetry of crystal.
In a supercell DFT calculation, the Kohn-Sham equations are solved for a given point k in the BZ. The charge density at each point r in the cell is found by the sum over all bands m and selected $k-$points in the whole BZ taking into account the occupancy f_{mk} of the each band at the point k:

$$n(r) = \sum_{mk} f_{mk} \left|\psi_{mk}(r)\right|^2$$

The exact estimation of the charge density at each point r corresponds to an integration over the entire BZ. To optimise the calculations, it is a common practice to compute a summation over a sampling of points in the BZ. A careful selection of those "special" points has been proved to be a good representation of the true result. We used the one developed by Monkhorst and Pack [79], which is based on equally spaced points along the

three directions in the reciprocal lattice.
The accuracy of a calculation is related to the density of $k-$points in the reciprocal space. Therefore, the smaller is the supercell the larger is the number of $k-$points required. It should be noted that the computing time greatly increases with the number of atoms and therefore, when possible, it is recommended to reduce the size of the supercell and increase the number $k-$points in order to achieve the same accuracy. It is also important to compute a similar density of $k-$points along the three directions in reciprocal space in order to achieve a uniform level of convergence in k. Therefore, the shorter lattice vector requires the higher number of $k-$points.

1.12 Geometrical optimization method

The optimised structure and its total energy are found through an iterative procedure based on the distribution of charge. An initial charge density matrix is constructed based on the charge density distribution of the isolated atoms. The Kohn-Sham equation

$$\sum_j (H_{ij} - E_\lambda S_{ij}) c_j^\lambda = 0$$

is solved to find the wavefunction expansion coefficients c_i^λ. These coefficients are used to calculated the new charge density. If the new charge density is not equal (or does not fulfil the criteria of convergence required), it is fed into the equation again and the process is repeated. This process is called a self-consistent cycle. At the end of the cycle the charge density obtained by solving the Kohn-Sham equation must be equal to the input charge density (within a pre-defined tolerance). The final self-consistent energy is the minimum energy of the system for the given atomic positions. In order to optimise the atomic positions of the nuclei, the best approach is to compute the forces acting on each atom. Atoms are moved towards their lowest-energy positions, and the structure with the minimum total energy is achieved.
Once the energy has been minimised with regard to the charge density, the eigenstates are known and the forces acting on each atom can be determined. The forces are given by the Hellman-Feynman theorem:

$$F_{Al} = -\frac{\partial E}{\partial R_{Al}}$$

where F_{Al} is the force on atom A in the direction l, E is the energy and R_{Al} is the coordinate of the atom A in the direction l.
The atoms are moved essentially in the direction of the force in order to reduce the total energy of the system. However, AIMPRO uses the conjugate gradient method. In this approach atoms are moved along a direction determined from the forces acting on each atom but orthogonal to all previous directions moved. The energy along the direction of displacement is approximated to a quadratic or cubic function and the amount of atomic motion is chosen to arrive at the position with the minimum energy. This approach finds a local minimum but cannot guarantee to find the global minimum.

1.13 Diffusion methods

The aim of diffusion methods is to locate saddle point structures. A saddle point is a transition structure connecting two equilibrium structures (local or global minima). It is a minimum in all directions except one, the "reaction coordinate". Hence, the second differential of the energy with respect to atomic positions is positive in all directions expect in the direction of the reaction. A saddle point structure is characterised by an imaginary vibrational frequency, as consequence of this negative second differential, which connects the initial and final equilibrium structures.
The location of a saddle point can be a greatly time consuming task. It is particularly difficult in layered materials because the flexibility of the layers may lead to a cusp in the energy *vs.* reaction coordinate profile. A cusp is indicative of a missing part of the reaction path, *i.e.* a faulty reaction coordinate. Whenever such a cusp was found, the reaction coordinate, or the method for finding it was modified to remove it.
A number of methods to define reaction coordinates and find saddle points have been applied through this thesis.

1. **Symmetry constraints**: If the diffusion process is symmetric, it is sometimes possible to trap the system at the saddle point by symmetry. This method is based on the fact that a structure with a symmetry element must be an extremum of energy.

2. **Plane constraints**: This is a series of constrained relaxations where the constrained atom(s) is forced to lie on a plane specified by the vector between two other atoms. These two other atoms are not constrained themselves. The constraint plane for the atom can be stepped along

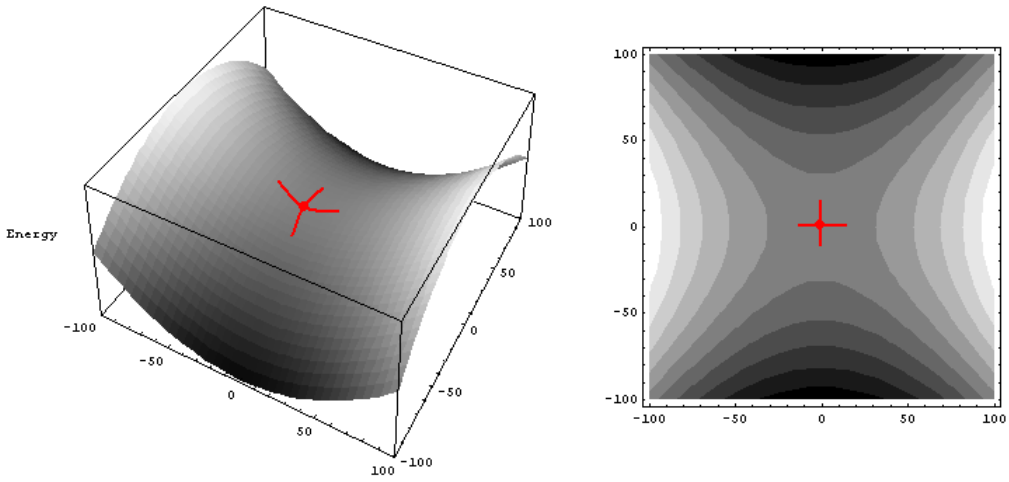

Figure 1.2: Plots of the energy surface $E = x^2 - y^2$. The saddle point is at the point {0,0} and it is indicated in red.

the vector between two other atoms. The constraint plane for the atom A defined with respect to atoms B and C is of the form $c = {r^2}_{AB} - {r^2}_{BC}$, with r_{AB} being the distance from atom A to atom B and c the constraint value. The atoms chosen are often the atoms involved in the diffusion. Normally one constraint is needed per pair of bonds made and broken.

3. **Orthogonal constraints**: This is a series of constrained relaxations stepping between the initial and final structures. A constraining vector, $\vec{v}$, is defined for each atom to be controlled with 3 components for the atoms of interest. This vector points from the initial structure to the final one. The structural configuration is stepped along the vector toward the final structure.

1.14 AIMPRO summary

AIMPRO, *"Ab Initio* Modelling Program", is a quantum package which solves the Schrödinger equation within the approximations of LDA-DFT. The great benefit of the code is its low computing time requirements. AIMPRO is more time efficient than other wave-function packages because the Gaussian Hamiltonian is smaller and sparse. In plane wave packages, all

the cell is analysed with the same expansion. In AIMPRO, the Hamiltonian for real space is smaller because only the enviroment of atoms is taken into account. This advantage makes AIMPRO applicable to supercells of about 200 atoms.
The pseudopotentials used will be BHS and HGH [86] for carbon atoms.
Atom-centred Gaussian basis functions are used to construct the many-electron wavefunction. These functions are labelled by four orbital symbols, where for each symbol all angular momenta are allowed up to maxima p (l=0, 1) and d (l=0, 1, 2), respectively.
Charge density oscillation in part-filled degenerate orbitals during the self-consistency cycle were smoothed using a Fermi occupation function with kT =0.04 eV.
A Bloch sum of these functions is performed over the lattice vectors to satisfy the periodic boundary conditions of the supercell. The Brillouin zone is sampled using the Monkhorst-Pack scheme [79].

Chapter 2

Dislocation glide enhancement in Silicon Carbide

2.1 Introduction

The first step in the discovery of semiconductors took place in 1883 when Michael Faraday observed that in silver sulfide the conductivity increased with an increase in temperature, in contrast to metals which showed a decrease when heated [11].
Over the years many other semiconductors have been found and nowadays these materials are the basic elements of every electronic device.
Semiconductor crystals always contain numerous defects which perturb the perfect lattice periodicity and influence its electrical and mechanical properties. Some defects have useful effects and are crucial for the device design, (*e.g.* doping with impurity atoms to achieve n- or p-type conductivity), while others have a destructive effect on devices and their performances.
Dislocations are often associated with the degradation of the electrical and optical properties of the devices. It is commonly found that dislocations scatter charge carriers, decreasing the carrier lifetime and increasing the resistivity of the materials. Furthermore, dangling bonds can be present along the dislocation line giving rise to energy levels in the forbidden band gap. These levels act as electron hole recombination centers degrading the optical properties of the device and giving a large leakage current when biased.
Since experiments alone often cannot yield information about the exact origin of defect-related effects or about how to suppress unwanted effects or to promote those which are desirable, we need theoretical models and calcula-

tions to interpret the experimental data.
Silicon carbide (SiC) has received special attention in recent years because of its suitability for electronic devices operating under high temperature, high power, high frequency and/or strong radiation conditions where conventional semiconductor materials, like Si and GaAs are considered to have reached their limits.
In comparison with the other semiconductor materials silicon carbide distinguishes itself by a combination of superior properties, such as high thermal conductivity, high thermal stability, high critical breakdown field, a hardness second to diamond and high resistance to radiation. This semiconductor can exist in more than 200 different polytype structures with a wide band gap ranging from 2.4 eV for the 3C-SiC polytype to 3.3 eV for the 4H-SiC polytype [12]. The latter properties make SiC a suitable material for light emitting devices in the visible range, where silicon is useless. The different SiC polytypes are usually describe by the Ramsdell notation, where the first character indicates the total number of formula units contained in the unit cell (reflecting the different stacking sequences) and then the letter C, H or R denotes the lattice type as being cubic, hexagonal or rhombohedral, respectively.
Despite its outstanding properties, several studies report a drawback: an increase in the voltage drop of *p-i-n* diodes under forward bias. In a common diode the forward voltage drop is almost independent with respect to the amount of current passing through the device, so it has a very steep characteristic in the current/voltage (I/V) graph. In SiC the I/V diode characteristics change under forward bias, reflecting an increase in the resistance in the device. Typically the initial forward drop of 3.5 V at 100 A cm^{-1} increase to 3.8 V after a few hours and over 15 V in a few days of constant operation.
Such behaviour renders the SiC diode much less attractive than its real potential characteristics. In particular high-power systems are frequently designed with several diodes connecting in parallel in order to increase the total current rating. The increase in the resistance of one diode would cause an increase in the current flow in the remaining stable components. At some point, the current flowing through the stable diodes could exceed the threshold maximum current of the devices and the system could fail catastrophically.
Recent experiments have shown that the forward voltage drop is due to expansion of stacking faults (SFs) in the active region of the diodes [13, 14,

15]. The SF regions are always bounded by Shockley partial dislocations; therefore the SF expansions are strongly connected with the mobility of the partials [16, 17, 18, 19]. Depending on the angle between the Burgers vector and the dislocation line the Shockley partial dislocations are 30° or 90° partial dislocations either with Si or C termination along the dislocation line in the glide plane, hence the respective labels Si(g) and C(g) (see Figure 2.1).

Under forward bias a broad band gap transition at approximately 1.8 eV is observed simultaneously with the glide of the partials [14]. Latest photoluminescence (PL) spectra [20] obtained from the mobile dislocations confirm the broad radiative band at $\sim$ 1.8 eV, and reveal a further narrow peak at 2.87 eV. Furthermore, electron beam-induced current (EBIC) experiments indicate that both types of 30° partial act as nonradiative centers [21] while optical studies show that the radiative transition rate on the Si(g) partials is much higher than that on the corresponding C(g) core dislocations [22].

Several experimental studies show that not all the partials glide under electron hole plasma injection, but rather that only the Si(g) 30° partials move rapidly, while the others are almost immobile [22, 23, 24]. Under electrical stress (forward bias) or optical excitation (laser beam) the activation energy for the kink migration of the partials is 0.27 ± 0.02 [14] or 0.25 ± 0.05 eV [20], respectively. These values are $\sim$ 10 times lower than the estimated value of 2.5 eV obtained from the temperature dependence of the yield stress [25].

It is commonly believed that recombination-enhanced dislocation glide (REDG)[26, 27, 28] is responsible for the rapid propagation of these planar defects. According to the phonon-kick mechanism, a nonradiative electron-hole recombination center should be present along the dislocation line and the released transition energy transferred into the reaction coordinate for glide migration of the Shockley partials.

The latest excitation spectrometry experiments reveal a nonradiative center at $\sim$ 2.4 eV above the valence band. Furthermore, these experiments clearly show that the latter deep level is responsible for the REDG mechanism on the Si(g) 30° partials [20]. Theoretical studies in 3C and 2H-SiC have pointed out that the C(g) partials are electrically inactive, while the Si(g) gives rise to a band gap level at $E_v + 0.4$ eV. In addition, the activation energy for the glide of the C(g) 30° partial is calculated to be 4.95 eV while that for the Si(g) is 4.60 eV for short dislocation segments [29]. So far, the electrical activity of the 30° partials and the deep level required by the REDG process still remains unclear.

In this work, I have investigated the dislocation core effect on electrical activity and kink migration. I have shown that the symmetric reconstructions along the dislocation line are always electrically active and have glide activation energies lower than the respective asymmetric reconstructions. Further, I have proposed a new model that can explain why the symmetric reconstructions become dynamically more stable under electron hole plasma and suggested why only the Si(g) 30° partials are mainly involved in the enhancement of the dislocation mobility. This model can be applied to any semiconductor material in order to predict the behaviour under electron hole plasma and could inspire new experimental techniques to reduce the degradation mechanism or, in a more fascinating way, to change the destructive effect into a new useful property of semiconductor materials.

2.2 Computational methods

The calculations are based on density functional theory in the local density approximation using the exchange correlation functional as parametrized by Perdew and Wang [30]. The basis sets employed consist of s, p, and d Gaussian orbital functions with four exponents, centered at the atomic sites [31]. Norm-conserving pseudopotentials based on the Hartiwigsen-Goedecker-Hutter [32] scheme were used. The charge density is represented by a plane-wave basis in reciprocal space expanded up to 300 Ryd. To perform the Brillouin zone integrations, I have used a Monkhorst Pack (MP) scheme [33] with 8 k-points along the dislocation line. In order to take into account the possible dispersion of the levels inside the band gap, a metallic filling is used, where the number of electrons at each k-point can differ. The initial atomic positions have been produced within isotropic elastic theory and then relaxed using DFT and the conjugate gradient algorithm.

2.3 Dislocation core structures

In hexagonal SiC the partial dislocations lie in the basal plane with Burgers vector $b_p = \frac{1}{3}\left[1\bar{1}00\right]$ and dislocation line $l = \left[11\bar{2}0\right]$. In order to investigate separately the properties of the single partials, the dislocations have been modelled using the cluster supercell hybrid. The periodicity of the lattice is kept only along the dislocation line (supercell component) while within the $\left\{11\bar{2}0\right\}$ plane, the unit cell is repeated to create a cluster keeping an empty space between the cluster and its images in the neighbouring unit cells of

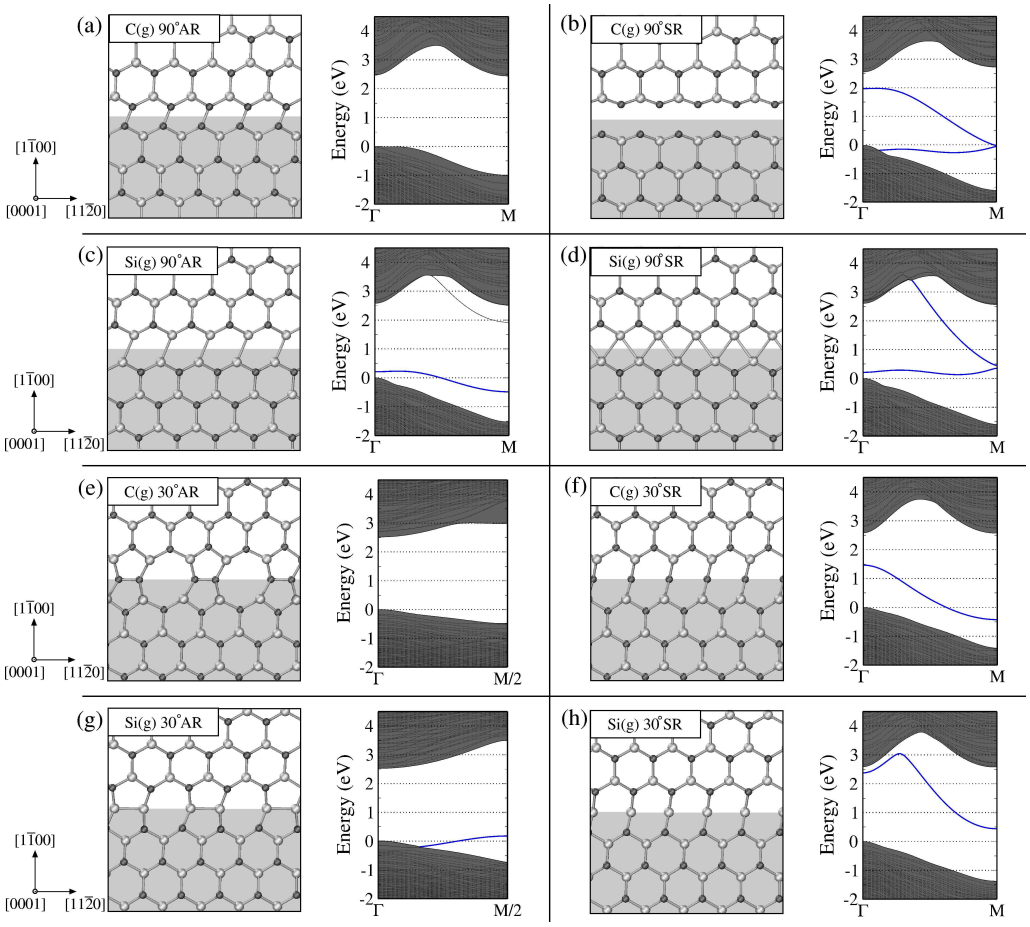

Figure 2.1: Projections on the glide plane {0001} of the partial dislocations, and the respective Kohn-Sham band structures in the neutral charge state. Left: the asymmetric reconstruction (AR); right: the symmetric reconstruction (SR). The intrinsic stacking fault regions accompanying the partials are shaded; (a, b) C(g) core 90° partial; (c, d) Si(g) core 90° partial; (e, f) C(g) core 30° partial; (g, h) Si(g) core 30° partial.

$\triangle = 8$ a.u. The silicon and carbon bonds along the surface are saturated by hydrogen-like atoms. The stoichiometry of the 90° partial unit cells are $Si_{84}C_{84}H_{52}$ with a total of 220 host atoms, while the stoichiometry of the 30° partials are $Si_{90}C_{92}H_{54}$ for the C(g) core and $Si_{92}C_{90}H_{54}$ for the Si(g) core, with a total of 236 host atoms. The lattice parameters of the bulk structure are $a = 3.06$ Å, $c/a = 3.27$ in excellent agreement with experimental values ($a = 3.07$ Å , $c/a = 3.27$ [34]), while the Si-C bond lengths are 1.88 Å.
The possible reconstructions along the dislocation line are shown in Figure 2.1. The symmetrical reconstructions (SRs) are characterized by dangling

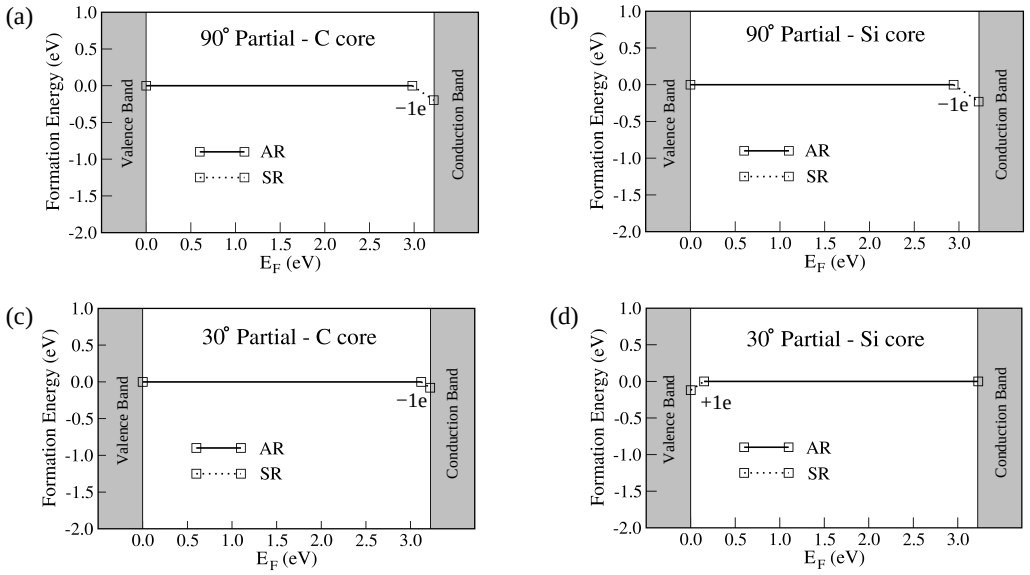

Figure 2.2: Formation energy as a function of the Fermi level. The solid line indicates the asymmetric reconstruction (AR) while the dashed line indicates the symmetric reconstruction (SR). (a) C(g) core 90° partial; (b) Si(g) core 90° partial; (c) C(g) core 30° partial; (d) Si(g) core 30° partial. The figure shows that the AR is always favourable in intrinsic bulk and moderately doped semiconductors, while the SR may become stable in strongly doped material when the Fermi level E_F is approaching the conduction band (a), (b), (c) or valence band (d).

bonds or quasi-fivefold bonded atoms along the dislocation line. In the asymmetrical reconstructions (ARs) the core atoms in pairs form a bond along the dislocation line. The band structure analysis shows that the dangling/weak bonds of the SR give rise to a half-occupied band. In the ARs the strong covalent bond splits the half- filled band, generating a fully occupied band near the top of or inside the bulk valence band (VB), and an empty band near the bottom of or inside the conduction band (CB).
Depending on the position of the Fermi level in the bulk band gap, both partials can sustain either the AR or SR reconstruction along the dislocation line. The electron chemical potential or Fermi level E_F is the energy at which the Fermi Dirac probability of occupation by an electron is exactly one half. The Fermi level represents an important quantity in the analysis of semiconductor behaviour. For intrinsic material the Fermi level lies at the middle of the band gap. In n-type the Fermi level lies closer to the bottom of the conduction band E_c, and the energy difference $(E_c - E_F)$

gives a measure of how strongly n-type the material is. In p-type materials the Fermi level lies closer to the top of the valence band E_v, and the energy difference $(E_F - E_v)$ gives a measure of how strongly p-type the material is. The formation energies of the respective reconstructions in defined [35] by

$$E^q_{form} = E^q_{tot} - E_{bulk} + q\,[E_F + E_v + \Delta V] \tag{2.1}$$

where E^q_{form} is the formation energy of the dislocation in the q charge state, E^q_{tot} is the total energy of the unit cell containing a dislocation with charge q, E_{bulk} is the energy of the bulk with the same stoichiometry and E_F is the Fermi energy with respect to the top of the valence band E_v. The potential $\triangle V$ is a correction term in order to line up the band structures of the different charge states with the bulk [36].
Figure 2.2 shows the formation energy of the most stable charge states for each configuration as a function of Fermi energy. When E_F is approaching the valence band ($E_F = 0$) we are in a strongly p-type regime, while when E_F is approaching the conduction band ($E_F = \triangle E_{gap} = 3.26$ eV) we are in a strongly n-type regime. In general, I have found that the AR (solid line in Figure 2.2) is always favourable in intrinsic bulk and moderately doped semiconductors, while the SR may become stable in strongly doped material (dashed line in Figure 2.2).

2.3.1 C(g) core 90° partial

In the AR the C-C bond length is 1.65 Å, longer by 7.8% than in bulk diamond (1.53 Å), while the C-Si backbonds of the core atoms range from 3.2 to 5.5% compared with the bulk SiC. This reconstruction is not electrically active. In strongly n-type doping the SR may become more stable. In the neutral charge state, the dangling bonds along the dislocation line are separated by 2.56 Å, expanded by 67% from the bulk diamond bond length. As a consequence, the backbonds of threefold coordinate core atoms are shortened (by 2.6%). The dangling bonds localized on the C atoms give rise to a half-filled band ranging from inside the VB to $E_v + 1.97$ eV. The AR is higher in energy than the SR by 1.03 eV/a_0 (a_0 = 3.06 Å is the bulk parameter lattice). In the negative charge state the distance between dangling bond atoms is 2.69 Å, 5.1% longer than the respective neutral charge state, while the backbonds of the C atoms are shortened by 5.1% with respect to the bulk SiC. The band structure analyses show a deep band ranging from $E_v + 0.06$ eV to inside the CB.

2.3.2 Si(g) core 90° partial

In the AR the Si-Si bond length is 2.38 Å, expanded by 1.7% with respect to bulk silicon (2.34 Å), while the backbonds are distorted by 1.6%. The band structure analysis gives a donor level at $E_v + 0.21$ eV at the Γ-point, and opens a little gap at the boundary of the BZ. In heavily n-type doped material the SR may become favourable. In the neutral charge state the Si atoms along the dislocation line are quasi-fivefold coordinate with a bond length of 2.69 Å, expanded by 15.0% with respect to the bulk silicon. The backbonds of the Si core atoms range between 1.0% and 0.4% compared to the bulk SiC. The band structure analysis shows a half-filled band ranging from $E_v + 0.21$ eV to inside the conduction band (CB). The AR is 0.34 eV/a_0 higher in energy than the respective SR. In the negative charge state the bond lengths between like atoms along the dislocation line are 2.58 Å, 4% smaller than in the neutral state. The backbonds are slightly shortened (by 1.9%) with respect to the bulk SiC. The band structure analyses show a deep band ranging from $E_v + 0.38$ eV to inside the conduction band (CB).

2.3.3 C(g) core 30° partial

The AR shows a C-C bond length of 1.67 Å, expanded by 9.2% with respect to bulk diamond, while the backbonds are distorted by between −2.66 and +3.72%. Due to the strong reconstruction, the band structure analysis shows that this dislocation has no deep state. In heavily n-type doped materials the SR can become stable. In the neutral and negative charge states the distance between like atoms along the dislocation line is 3.06 Å, *i.e.* double the bulk diamond bond length. The backbonds of the threefold coordinate atoms are shortened by 3.7% for the neutral SR and by 5.8% for the negative charge state. The dangling bonds give rise to a half-filled band ranging from VB to $E_v + 1.46$ eV for the neutral charge state and from $E_v + 0.21$ eV to the CB for the negative charge state. The neutral AR is 0.51 eV/a_0 higher in energy than the respective SR.

2.3.4 Si(g) core 30° partial

The AR shows a Si-Si bond length of 2.35 Å expanded by 0.4% with respect to bulk silicon, while the backbonds are shortened by 2.0%. The band structure shows a deep band ranging between the VB to $E_v + 0.19$ eV. In heavily p-doped materials the SR can become favourable. In the neutral and positive charge states the distance between dangling bonds along the

	Asymmetric Reconstruction (AR)		Symmetric Reconstruction (SR)	
	Γ-point	$M/2$-point	Γ-point	$M/2$-point
90° C(g)	—	—	$E_v + 0.19$ eV	—
90° Si(g)	$E_v + 0.21$ eV	—	$E_v + 0.19$ eV	—
30° C(g)	—	—	$E_v + 0.19$ eV	—
30° Si(g)	—	$E_v + 0.19$ eV	$E_v + 0.19$ eV	$E_v + 0.19$ eV

Table 2.1: Deep band localized along the dislocation line in the neutral charge state. The top of the valence band is at the Γ-point of the BZ, while the bottom of the CB is at the M-point. Later, in the discussion section, I have proposed that the free energy of the SRs would be dynamically lowered by continuous electron-hole transitions between the respective deep levels and valence/conduction bands. The energy units are in eV.

dislocation line is 3.06 Å, expanded by 31% with respect to the bulk silicon. The respective backbonds are shortened by about 2.4% and 4.3% for the neutral and positive charge state, respectively. These structures are electrically active with a deep band ranging between $E_v + 0.44$ eV at the M-point to $E_v + 2.36$ eV at the Γ-point for the neutral charge state and between the VB and $E_v + 2.01$ eV at the Γ-point for the positive charge state. The neutral AR is 0.55 eV/a_0 higher in energy than the SR.

We observe that the AR of the 90° partials requires a core shear between the unfaulted and stacking fault regions of about $0.8-1.2$ Å for the C(g) core and $1.0 - 1.3$ Å for the Si(g) core dislocations. In the case of the 30° partials, the AR does not require a long ranged shear, but rather only flipping of alternate atoms in the core. Table 2.1 summarises the deep bands found for each dislocation in the neutral charge state. Later, in the discussion section, I will propose that under electron hole plasma injection the free energy of the SRs are dynamically lowered by continuous electron hole transitions between their respective deep levels and valence/conduction bands.
In conclusion for the AR, only the Si(g) core partials give rise to a deep narrow band at $E_v + 0.2$ eV in substantial agreement with those found previously [29] ($E_v + 0.4$ eV). The small difference between the two values can be attributed to the different sizes of the unit cells: 120 host atoms with a $1 \times 1 \times 2$ MP set of k-points in Ref. [29], against $220 - 236$ atoms with $1\times1\times8$ MP grid in the present work. Furthermore, the bond length between like atoms at the core of the Si(g) partials is 2.35 Å, while at the core of the C(g) partial it is 1.67 Å. These results are in very good agreement with the values found by Bernardini and Colombo (2.37 Å for the Si(g) partial, and

1.68 Å for the C(g) partial [37]. In the SR all the partials are electrically active with a half-filled deep band. In particular, the 30° dislocations in the neutral charge state give rise to a deep band ranging between the top of VB to $E_v + 1.46$ eV for the C(g) partial and a deep band ranging between $E_v + 0.44$ eV and $E_v + 2.36$ eV for the Si(g) partial.

2.4 Kink migration

Following the Hirth Lothe model, the mobility of the dislocations is determined by the formation and migration of kinks. The dislocation velocity is given by [38]:

$$v_{dis} = e^{-\frac{Q-T\cdot S}{kT}} \tag{2.2}$$

where Q is the activation energy and S is an entropy term. The latter factor will not be calculated in this work. The activation energy for short dislocation segments is the sum of the formation energy $2F_k$ of a kink pair, and the kink migration energy W_m. The formation energy controls the density of kinks in thermodynamic equilibrium, while W_m determines the expansion of the kinks along the dislocation line.
When the dislocation length is bigger than the mean separation between kinks or between strong obstacles, the activation energy becomes $Q = F_k + W_m$. The latter expression controls the migration velocity for long dislocation segments. Kinks can be formed only in pairs and the formation energy of a kink pair when the separation of the single kinks in $n \cdot b$ is defined as:

$$2F_k = \triangle E_{kink\,pair} + E_{int}\,(n) \tag{2.3}$$

where F_k is the formation energy of a single kink, $\triangle E_{kink\,pair}$ is the formation energy of a kink pair with the smallest possible separation and E_{int} is the kink-kink interaction term.
The latter term is approximately given by elasticity theory. For the 90° partials it is defined by [38]:

$$E_{int}\,(n) = -\frac{\mu b_p^2 h^2}{8\pi n a_0}\frac{1-2\nu}{1+\nu} \simeq -\frac{0.24}{n}\,\text{eV} \tag{2.4}$$

while for 30° partials the kink-kink interaction term is given as [38]:

$$E_{int}\,(n) = -\frac{\mu b_p^2 h^2}{32\pi n a_0}\frac{4+\nu}{1-\nu} \simeq -\frac{0.49}{n}\,\text{eV} \tag{2.5}$$

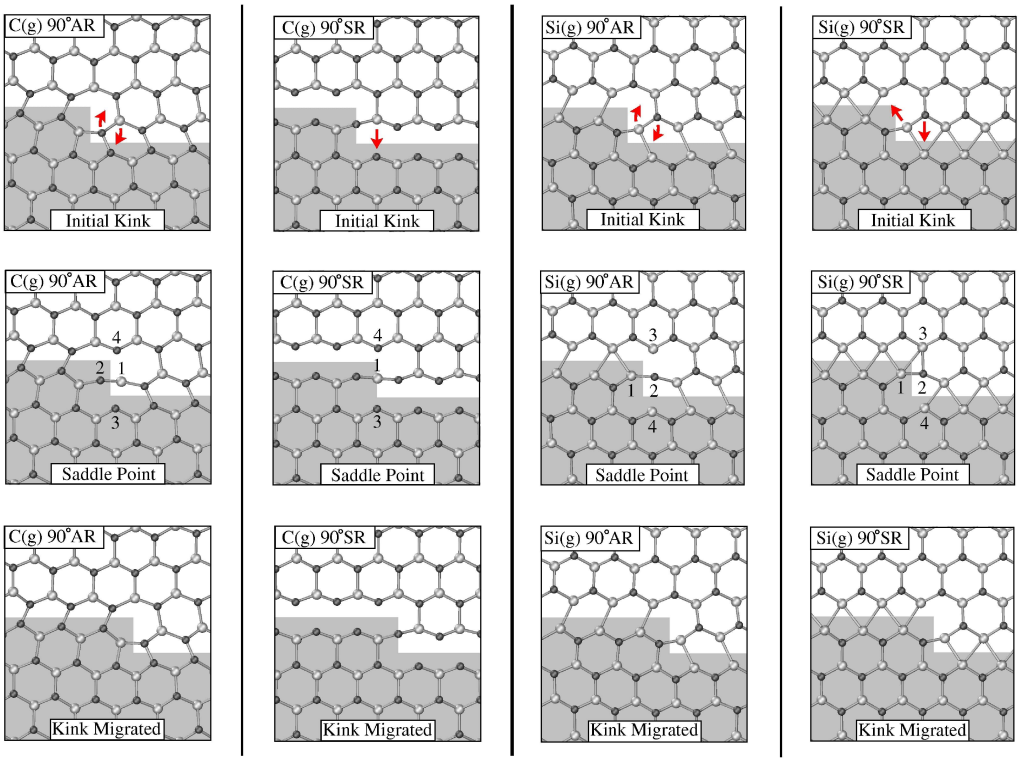

Figure 2.3: Kink migrations for the C(g) core 90° partial dislocation (first column: asymmetric reconstruction, second column: symmetric reconstruction) and Si(g) core 90° partial (third column: asymmetric reconstruction, fourth column: symmetric reconstruction). The shading regions underline the stacking fault expansion associated with the kink migrations. (Top) Initial kink. The arrows indicate the atoms mainly involved during the kink migration. (Centre) Saddle point. The numbers show the atom positions used by the constraints. (Bottom) Kink migrated.

where μ is the shear modulus (1.23 eV/Å [39]), b_p is the modulus of the Burgers vector $(a_0/\sqrt{3})$, ν is Poisson's ratio (0.21 [40]), h is the height of the kink $(a_0/\sqrt{3})$ and $n \cdot a_0$ is the separation between single kinks ($a_0 = 3.06$ Å). The term $\triangle E_{kink\,pair}$ is found by introducing a kink pair along the dislocation line for both the C(g) and Si(g) core dislocations. The formation energies are then found by subtracting the energies of the corresponding straight dislocations.

To model the single kink and kink pair, I have used a hybrid cluster supercell approach, with several layers along the dislocation line (supercell component). The stoichiometry of the unit cells used is $Si_{35}C_{35}H_{24}$ per layer for the 90° partials, while the stoichiometry of the 30° partials is $Si_{27}C_{28}H_{21}$

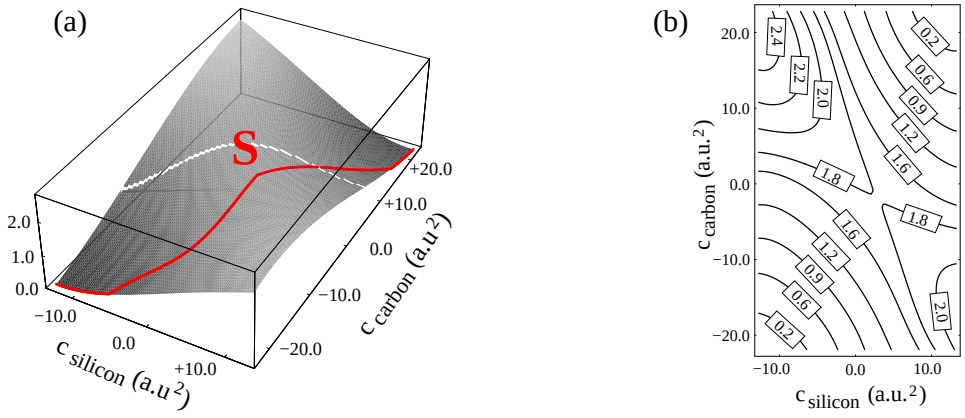

Figure 2.4: (a) Surface energy and (b) contour plot of the kink migration for the C(g) core 90° partial dislocation. The two global minima represent the energy of the initial and migrated kink, while the maximum of the migration path (indicated with S) represents the saddle point.

per layer for the C(g) core and $Si_{28}C_{27}H_{21}$ per layer for the Si(g) core. In order to check the convergence of the calculated energies I have increased the number of layers along the dislocation line up to 9. Test calculations have shown that $6-7$ layers along the dislocation line are large enough to describe the quantum-mechanically bonds of the kinked dislocations. In the following discussion, I have described the kink migration of the AR and SR reconstructions in their more stable charge state, *i.e.* the neutral charge state for the AR, the negative charge state for the SR 90° partials and SR C(g) core 30° partial, and the positive charge state for the SR Si(g) core 30° partial. In this way the reconstructions under investigation are always the global minimum energy reconstruction.
The elementary step of single kink migration was found by rotating the central Si and C atoms (arrows in Figure 2.3, 2.5, 2.6) by about 90° along an axis normal to the glide plane. This causes a kink migration along the dislocation and a consequent expansion of the stacking fault region associated with the partials. To investigate the intermediate structures between the initial and migrated kink I have defined two variables, or constraints, $c_{silicon}$ and c_{carbon} associated with the two central atoms, R_1 and R_2:

$$c_{silicon} = |R_1 - R_4|^2 - |R_1 - R_3|^2$$

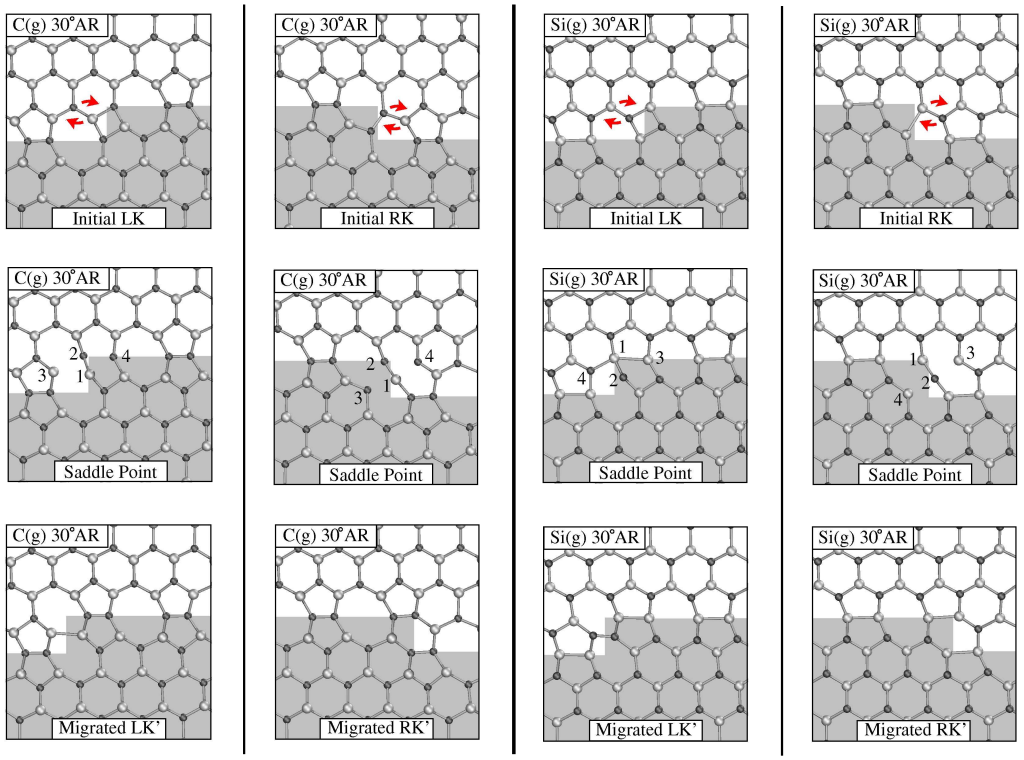

Figure 2.5: Kink migration paths for the 30° partial in the asymmetric reconstructions. The migration path of the C(g) core dislocations (first column: left kink, second column: right kink) and the migration path of the Si(g) core dislocations (third column: left kink, fourth column: right kink). The shading regions underline the stacking fault expansion associated with the kink migrations. (Top) Initial kink. The arrows indicate the atoms mainly involved during the kink migration. (Centre) Saddle point. The numbers show the atom positions used by the constraints. (Bottom) Kink migrated.

$$c_{carbon} = |R_2 - R_3|^2 - |R_2 - R_4|^2$$

where R denotes the coordinate of the atom and the subscript indicates the atom as depicted in Figure 2.3, 2.5, 2.6. In some of the SRs it is only one atom that is mainly involved in the migration process, therefore only one constraint is used. Then meshes of 10×10 intermediate points were used to model the single kink migrations. For each set of fixed values of the two constrains all the structures were relaxed using the conjugate gradient method. Figure 2.3 shows the projection into the basal plane of the elementary kink migration steps for the respective 90° partial dislocations. For the 90° partial dislocations the initial and kinked structures are quantitatively equivalent

in terms of bond lengths and strains. Figure 2.4 shows the two-dimensional energy surface for the kink migration of the C(g) core 90° partial.
For the AR 30° partials four topologically different types of kinks can be generated. Figure 2.5 shows the structure of the left kink (LK) and the right kink (RK) in the asymmetric reconstructions. Each of the two kinks has its alternate configurations, depending on the kink position along the dislocation line. In general the alternative kinks, named LK' and RK', have higher formation energies than the normal kinks and act as intermediate steps during the kink migrations. All atoms in these different types of kinks are fourfold coordinate. I observed that the migrated left kinks form a reconstructed bond, of the opposite type to the reconstruction bonds of the respective partial, *i.e.* the C(g) partial LK' presents an alien Si-Si bond and the Si(g) partial LK' presents an alien C-C bond (see Figure 2.5).
For the 30° partials SR, the normal and alternative kinks are topologically equivalent, reflecting their single periodicity along the dislocation line (see Figure 2.6). Considering that the dislocation motion is dominated by the kinks that migrate at the fastest rate [41] I have chosen the lowest migration energy W_m between the LK and RK saddle point energies.

2.4.1 C(g) core 90° partial

In the AR the C-C bonds closest to the kink step are slightly compressed with lengths of 1.64 Å, while the others reproduce the bond length of the straight dislocation (1.65 Å). The backbonds range between $1.81 - 2.04$ Å, representing strains of up 9%. I have found a saddle point near the origin of the constraint $c_{silicon}$, c_{carbon} with migration energy W_m of 1.78 eV. The formation energy $2F_k$ for the corresponding kink pair is 0.36 eV. This yields an activation energy Q of 2.14 eV for short segment dislocations. In the SR the distance between dangling bond atoms closest to the kink step are 2.83 Å, while the others far from the kink step reproduce the value of the straight dislocation (2.69 Å). The migration barrier W_m is found exactly at the origin of the constraint with saddle point energy of 0.21 eV. The formation energy $2F_k$ for the corresponding double kink is 0.40 eV. Therefore the activation energy Q for the migration of short segment dislocations is 0.61 eV.

2.4.2 Si(g) core 90° partial

In the AR, the Si-Si bonds close to the kink step are 2.37 Å (only 0.4% compressed with respect to the straight dislocation) and 2.45 Å (3% stretched

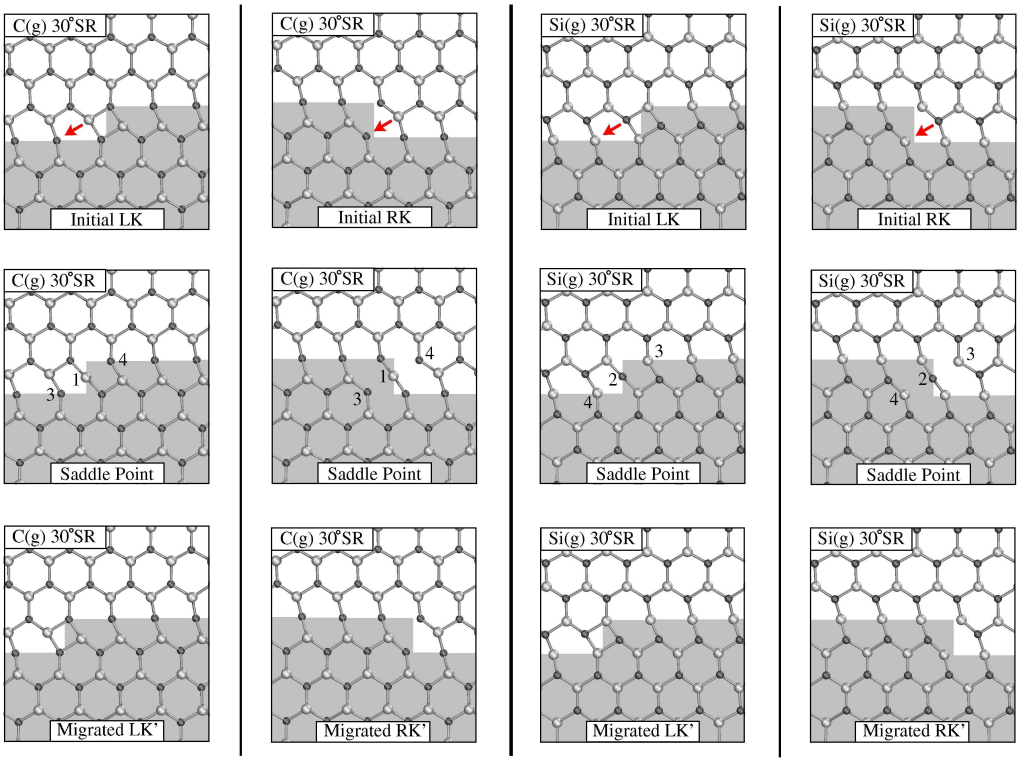

Figure 2.6: Kink migration for the 30° partial in the symmetric reconstructions. The migration path of the C(g) core dislocations (first column: left kink, second column: right kink) and the migration path of the Si(g) core dislocations (third column: left kink, fourth column: right kink). The shading regions underline the stacking fault expansions associated with the kink migrations. (Top) Initial kink. The arrow indicates the atoms mainly involved during the kink migrations. (Centre) Saddle point. The numbers show the atom positions used by the constraints. (Bottom) Kink migrated.

with respect to the straight dislocations). The backbonds have lengths ranging between $1.84 - 1.92$ Å, representing strains of up to 2%. The difference in energy between the double kink and the straight dislocation is 0.10 eV, and the corresponding formation energy $2F_k$ is 0.34 eV. The saddle point barrier for the kink migration is 1.85 eV, which gives an activation energy Q of 2.19 eV for short dislocation segments. For the SR, the lengths between dangling bond like atoms close to the single kink are 2.57 Å (expanded by 8% with respect to the straight dislocation). The backbonds have lengths between $1.84 - 1.92$ Å, representing strains of up to 2% (exactly the same of the AR). The saddle point energy W_m is 0.34 eV while the formation energy $2F_k$ is 1.21 eV. This yields the corresponding activation energy Q of 1.55 eV

for short dislocation segment.

2.4.3 C(g) core 30° partial

In the AR structures, the C-C bond lengths close to the kink steps range between $1.62 - 1.70$ Å, representing strains of up to 11%, whereas the backbonds have lengths ranging between $1.80 - 2.15$ Å, representing strains of up to 14%. The alien Si-Si bonds present in the LK' have roughly the same length of the bulk Si. The intermediate LK' and RK' structures are 2.51 and 0.33 eV higher in energy than the initial LK and RK structures. The barrier heights are calculated to be 2.98 and 1.47 eV for the LK and RK migrations, while the formation energy of the LK+RK kink pair, $2F_k$, is 1.78 eV. Then the corresponding activation energy Q for the fastest kink (RK) is 3.25 eV. In the case of the SR, the C-Si bonds range between $1.76 - 2.00$ Å, representing strains of up to 6%. The saddle point energies are found to be 0.09 and 0.22 eV for the LK and RK migrations, while the formation energy of a kink pair is found to be 1.48 eV. Therefore both the LK and RK have fairly equivalent activation energies, with values of 1.57 eV for the LK and 1.70 eV for the RK.

2.4.4 Si(g) core 30° partial

In the ARs, the Si-Si bond lengths close to the kink steps range between $2.31 - 2.41$ Å, representing strains of up to 3%, while the backbonds have lengths ranging between $1.79 - 2.02$ Å, representing strains of up to 7%. The alien C-C bond length in the LK' structure is 1.62 Å, expanded by 6% with respect to the bulk diamond. The intermediate structure LK' is 2.07 eV higher in energy than the LK structures, while the structures RK and RK' have roughly the same energy (the difference between the two formation energies is less than 0.03 eV). The saddle point energies are 2.47 and 2.17 eV for the LK and RK respectively, while the formation energy of the LK + RK kink pair is 2.26 eV. The corresponding activation energy for the fastest kink (LK) is 4.43 eV. For the SR, the C-Si bonds range between $1.78 - 2.02$ Å. The saddle point energies are calculated to be 0.08 and 0.06 eV for the LK and RK migrations, while the formation energy of the LK+RK kink pair is 2.12 eV. Therefore, both the LK and RK have fairly equivalent activation energies, with values of 2.20 eV for the LK and 2.18 eV for the RK.

For all the partials, the dislocation dynamics of the ARs are controlled by the kink migration barrier W_m ($W_m > F_k$), while for the SRs the dislocation

dynamics are governed by the kink formation energy F_k ($F_k > W_m$) (see Table 2.2). In general, I have found that the SR dislocations are always more mobile than the AR ones, but in both reconstructions the C(g) partial possesses the lower activation energy. Furthermore, in all the dislocations the 90° partials present higher mobility than the 30° partials. Therefore, at high temperature and when large obstacles are not present, the C(g) core 90° partial is clearly the most mobile dislocation, which is in agreement with the results found by Blumenau *et al.* [29].

Dislocation	Core	$\triangle E_{kink\,pair}$	$2F_k$	W_m	$Q = 2F_k + W_m$
C(g) 90°	AR (0 e)	0.12	0.36	1.78	2.14
	SR (−1 e)	0.16	0.40	0.21	0.61
Si(g) 90°	AR (0 e)	0.10	0.34	1.85	2.19
	SR (−1 e)	0.97	1.21	0.34	1.55
C(g) 30°	AR (0 e)	1.29	1.78	1.47	3.25
	SR (−1 e)	0.99	1.48	0.09	1.57
Si(g) 30°	AR (0 e)	1.77	2.26	2.17	4.43
	SR (+1 e)	1.63	2.12	0.06	2.18

Table 2.2: Kink formation energies $2F_k$ and migration barriers W_m for the 90° partial dislocations in the ARs (neutral charge state) and SRs (negatively or positively charge state). The resulting glide activation energies $Q = 2F_k + W_m$ are relevant for short segment dislocations (the respective energy are in eV).

2.5 Discussion

Before describing the new model, I briefly summarise what so far is suggested to explain the enhancement of the dislocation velocity in SiC. To the best of my knowledge, two main models have been proposed:

1. REDG between Si(g) core partial and SF band level [29]:
   These authors have shown that only the Si(g) core partials are electrically active with a band gap level at $E_v + 0.4$ eV. Because the SFs formed under electron-hole plasma are predominantly of the single-layer type [17, 18], with a narrow band at $E_c + 0.2$ eV [42, 43] this model predicts a nonradiative recombination center at about ~ 2.7 eV (with a band gap of 3.3 eV). This model is not able to explain the electrical activity of both the 30° partials, and in particular, the 1.8 eV radiative emission found under forward bias remains inexplicable.

2. Soliton model: (proposed by Pirouz *et al.* [20]):
   A soliton is always associated with a dangling bond along the dislocation line and can act as a preferential site for nucleation of kink pairs (Heggie *et al.* [44]). Since the Si(g) core dislocation gives rise to a band gap at $E_v + 0.4$ eV and assuming that the soliton dangling bond gives rise to a deep level $E_v + 2.4$ eV acting as both a radiative and a non-radiative site, this model can explain the radiative transition at ~ 2.0 eV and provide a level deep enough for the REDG theory (~ 2.4 eV). The possible weakness of this model is the soliton formation energy. For example, in silicon the formation energy of a soliton [45, 46, 47] is $1.2 - 1.4$ eV, and the Boltzmann probability of having a density of soliton sites n_S along the dislocation line of length l becomes

$$n_S = e^{-\frac{F_S}{kT}} \cdot \frac{l}{a_0} \tag{2.6}$$

   where a_0 is the unitary repeat distance along the dislocation line (3.06 Å). With the temperature range of the measured [14, 20] dislocation glide velocity in SiC of $300 - 500$ K ($k_BT = 0.026 - 0.043$ eV), and a formation energy of $F_S = 1.2$ eV, we need a dislocation line of length ranging between $\sim 10^8 - 1$ km in order to have $\sim 3 - 2$ solitons in thermal equilibrium (Boltzmann constant $k_B = 8.617 \times 10^{-5}$ eV K^{-1}). In a later study I will show that the Si(g) soliton formation energy in 4H-SiC is less than a soliton in Si but still too large to explain the enhancement of the dislocation velocity alone.

My theoretical study shows that both dislocations can support the symmetric and asymmetric reconstructions. In the AR only the Si(g) dislocation is electrically active with an energy level of ~ 0.2 eV above the VB. The SRs characterized by dangling bonds on like atoms along the dislocation line are always electrically active. In the neutral charge state the C(g) 90° partial gives rise to a deep band ranging from the top of the VB to $E_v + 1.97$ eV, while the Si(g) gives rise to a band ranging from $E_v + 0.21$ eV to the top of the CB. In a similar way, the C(g) 30° partial also gives rise to a deep band ranging from the bottom of the VB to $E_v + 1.46$ eV, while the Si(g) core gives rise to a deep band ranging from $E_v + 0.44$ eV to $E_v + 2.36$ eV.
The kink migration analysis shows that the SRs are always more likely to move. For C(g) 90° partials, the activation energy Q is lowered from 2.14 eV for the AR to 0.61 eV for the SR, while for the Si(g) core dislocations, the activation energy Q is lowered from 2.19 eV for the AR to 1.55 eV for

the SR. For 30° partials, the activation energy Q is lowered from 3.25 eV for the AR to 1.57 eV for the SR, while for the Si(g) core dislocations, the activation energy Q is lowered from 4.43 eV for the AR to 2.18 eV for the SR.
My results show that the AR does not possess band gap levels deep enough, as required by the REDG mechanism. Therefore, the AR dislocations cannot explain the enhancement of the dislocation mobility. For SR dislocations the C(g) 90° partial and both the 30° partials present deep levels that can act as electron-hole recombination center, as required by REDG theory. At this stage I can only observe that Si(g) 30° partials possess a $E_v + 2.36$ eV deep level at the Γ-point, very close to the nonradiative center revealed by excitation spectrometry experiment (~ 2.4 eV above the valence band).
Therefore, the following model is presented:

- **New model: Savini model**

Under electron-hole plasma injections, the free energy of the SR 30° partials are dynamically lowered by continuous electron-hole transitions between the respective deep levels and valence/conduction bands.
To stabilize the SR 90° partials, a shear between the unfaulted and stacking fault regions at the core of the partials along the dislocation line is required, while for the 30° partials the AR does not require a long ranged shear, but rather only requires flipping of alternate atoms in the core. Therefore, only for the 30° partials does the SR dislocation line becomes more stable than the AR with a strong dynamic charge screening provided by the continuous electron-hole plasma injections. The deep levels provided by the SR are dynamically positive (hole recombination) and negatively (electron recombination) charged. However, the strong charge screening of the dislocation line surrounded by an electron hole plasma freezes the deep levels inside the band gap, *i.e.* the 30° partial deep levels correspond to the respective neutral band structures.
The Si(g) 30° partials provide a deep band ranging from $D_1 = E_v + 2.36$ eV at the Γ-point of the Brillouin zone to $D_2 = E_v + 0.44$ eV at the M-point of the Brillouin zone. The level D_1 explains the latest optical activation energy for the dislocation glide at ~ 2.4 eV above the VB [20]. This deep level acts as the electron-hole recombination center as required by the REDG theory and explains why the Si(g) dislocations move under forward bias/optical excitation. A radiative transition of 2.82 eV between the bottom of the conduction band ($E_c - E_v = 3.26$ eV) and D_2 explains the narrow peak at ~ 2.87 eV found by the photoluminescence spectra [20], while the radiative

transition of 1.9 eV between D_1 and D_2 (here called T_{Si}) explains the ~ 1.8 eV electroluminescence peak found during the growing of the stacking faults [14, 20].
The C(g) 30° partials provide a deep band ranging from $D_{C(g)} = E_v + 1.46$ eV to the top of the VB. This level can provide a radiative/nonradiative transition of 1.8 eV between the bottom of the CB to $D_{C(g)}$ (here called T_C) and a nonradiative transition of 1.46 eV between the top of the VB to $D_{C(g)}$. These results are in agreement with the latest EBIC experiment reporting that both types of 30° partials act as nonradiative centers [21].
However, optical studies show that the radiative transition rate of the Si(g) partials is much higher than the corresponding C(g) core dislocations [22]. Here I observe that both the respective radiative transitions T_{Si} and T_C are of indirect type, *i.e.* with electron phonon coupling. In particular, the two transitions involve the creation of phonons at different points of the Brillouin zone. I suggest that the reason why the radiative transition rate on the Si(g) partials is higher than the corresponding C(g) core dislocations is due to the different kind of phonons created that could hinder/increase the stability of the SR dislocation line. The same reason can explain why only the Si(g) core 30° partials are mobile under electron-hole plasma injection.

2.6 Conclusions

First-principle calculations show that both the dislocations can support the symmetric and asymmetric reconstructions. In the AR only the Si(g) core partials present a band gap level, while all the SR dislocations are electrically active. In particular, I have shown that the Si(g) 30° partials can explain the optical activation energy for the dislocation glide at ~ 2.4 eV above the VB, the narrow peak at 2.87 eV and the broad band at ~ 1.8 eV found in photoluminescence spectra.
Therefore, I have proposed a theoretical model, which can explain in details all the following experimental evidence:

• Why under forward bias the dislocations can be electrically active:

Under electron-hole plasma injections (*i.e.* under forward bias), the free energy of the SR dislocations is dynamically lowered by continuous electron-hole transitions between the respective deep levels and valence/conduction

• Why the 90° partials are immobile while the 30° partials can move:

To stabilize the SR 90° partials, a shear between the unfaulted and stacking

fault regions along the dislocation line is required, while for the 30° partials the AR does not require a long ranged shear, but rather only requires flipping of alternate atoms in the core. Therefore, only for the 30° partials does the SR dislocation line becomes more stable than the AR with a strong dynamic charge screening provided by the continuous electron hole plasma injections. The deep levels provided by the SR are dynamically positive (hole recombination) and negatively (electron recombination) charged.
However, the strong charge screening of the dislocation line surrounded by electron-hole plasma freezes the deep levels inside the band gap, *i.e.* the 30° partial deep levels correspond to the respective neutral band structures. Therefore, both the 30° partials can provide band-gap level deep enough as required by the REDG mechanism.

• Why only the Si(g) 30° dislocations move:

The band structure analysis have shown that both the 30° partials allow electrical transitions of indirect type, *i.e.* with electron-phonons coupling. These transitions can involve the creation of phonons at different points of the Brillouin zone. I have suggested that the reason why only the Si(g) 30° dislocations are mobile under electron-hole plasma injection is due to the different kind of phonons created that could hinder (for the C(g) 30° dislocations) or increase (for the Si(g) dislocations) the stability of the SR dislocation line.
The same reason explains why the radiative transition rate on the Si(g) dislocations is higher than the corresponding C(g) dislocations.

In conclusions my theoretical model can explain the anomalously enhancement of the dislocation mobility in SiC. This model can be applied to any semiconductor materials in order to predict the behaviour under electron-hole plasma and could inspire new experimental technique to reduce the degradation mechanism.

Chapter 3

Elastic Theory in Graphite

3.1 Introduction

First principles density functional calculations within the Local Density Approximation have provided highly plausible results, but the folklore of interlayer interactions is that LDA does not include an important part of the physical interaction between layers (the van der Waals interactions) and therefore should not be relied upon.
Contradicting this belief, I have demonstrated that LDA performs excellently for graphite and reproduces with precision the all elastic properties (*i.e.* the elastic constants).
The main disagreement between theory and experiment is the value of the elastic constant C_{13} (positive for experiment studies and negative for theoretical studies).
The sign of this elastic constant is crucial for the elastic properties of the material; a positive (negative) value of C_{13} means that under compression of the parameter lattice a_0, the parameter lattice c_0 tend, to expand (contract). Therefore theory and experiment describe graphite as a material with an opposite elastic behavior.
This chapter is organized as follow:

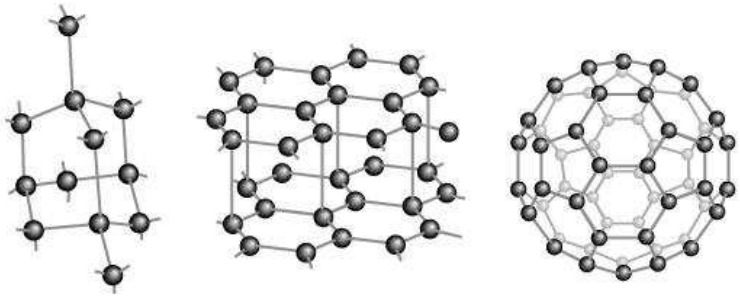

Figure 3.1: Carbon is found free in nature in three allotropic forms: diamond, graphite and fullerene.

Section 3.2: General overview of the graphite properties.

Section 3.3: I have studied the *"classical"* second and third order elastic constants.

Section 3.4: I have developed the theory of a bent plane and studied the mesoscale elastic properties of a single plane of graphite (graphene).

Section 3.5: I have worked up the graphite case and shown the full sets of mesoscale elastic constants.

3.2 Literature review

Graphite properties

Carbon is found free in nature in three allotropic forms: graphite, diamond, and fullerene (see Figure 3.2). The element carbon has an atomic weight of 12.010 consisting of two stable isotopes with atomic weights 12 (C_{12} abundance: 98.9 %) and 13 (C_{13} abundance: 1.1%).

The ideal crystal structure of graphite consists of layers in which the carbon atoms are arranged in an open honeycomb network containing two atoms per unit cell in each layer (labelled α and β in Figure 3.2).

The stacking of the graphene layers is arranged such that the α and α' atoms on consecutive layers are on the top of one another, while the β atoms in one plane are over the unoccupied centers of the adjacent layers, and similarly for the β' atoms on the other plane. This gives rise to two distint planes, which are labeled by A and B.

These distint planes are stacked in the $ABAB$ Bernal stacking[1], with a in-

[1]This hexagonal structure was proposed by Hull in 1917 and then it was confirmed by Bernal

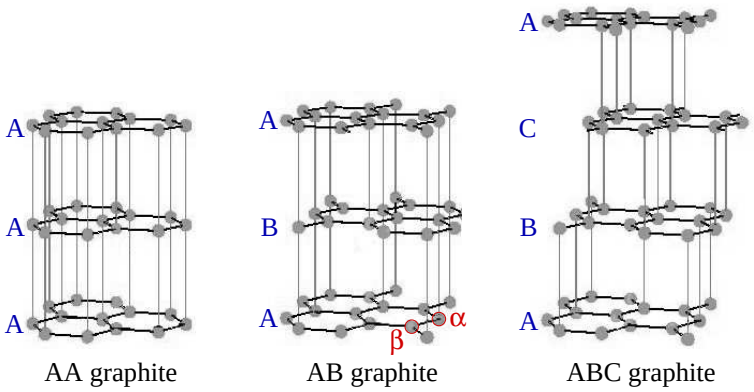

Figure 3.2: The three allotropic structures of graphite, AA stacking, AB Bernal stacking (or hexagonal graphite), ABC stacking (or rhombohedral graphite). The turbostratic graphite does not possess a regular periodicity along the c-axes and therefore it is not shown.

plane lattice constant $a_0 = 2.462$ Å, a c-axis lattice constant $c_0 = 6.708$ Å. This crystal structure is consistent with the D^4_{6h} ($P6_3/mmc$) space group and possesses 4 carbon atoms per primitive unit cell.
The atomic number of carbon atom is 6, with electronic structure $1s^2 2s^2 2p^2$. The intralayer bonding is due to an overlap between sp^2-hybridized orbital forming σ-bonds between nearest-neighbor C atoms. In addition, π-bonding takes place between the remaining p_z-orbitals on each atom that point perpendicularly to the layer [55].
Several experimental evidence (X-ray spectrum, electron diffraction and transmission electron microscopy studies) indicate the existence of a second allotropic form of graphite: the rhombohedral graphite. In this structure, the third layer has the same stacking order as the second to the first and the resulting stacking ABC is formed along the c-axis. The ratio of rhombohedral/hexagonal stacking can be increased by deformation processes such as grinding or powdering. However, by heating up to 3000 °C the hexagonal structure is completely restored [52].
The third allotropic form of graphite is the so called turbostratic graphite, a peculiar stacking of parallel graphitic mono-layers with no periodicity along the c-axis. In this structures the layers are randomly shifted and rotated and the interlayer spacing is changing from plane to plane.
The fourth allotropic form is the AA graphite, where the carbon atoms are directly located on top of each other, leading to an AA stacking sequence (see

in 1924 [49, 65].

Figure 3.2). This structure is highly instable in pure graphite, nevertheless in Lithium intercalated graphite this structure becomes the most energetically favourable [66]. Moreover, a recent work has shown that regions of AA stacking should be present along the graphite Moire patter [48].
Several sources of crystalline graphite are available, but differ somewhat in their overall characteristics. Nowadays the graphite samples frequently used are:

- Natural single crystal flakes: natural graphite is found in many parts of the world including United Kingdom, United States, Italy, Madagascar and Siberia. The flakes are usually small in size (typically much less than 0.1 mm in thickness), and contain defects in the form of twinning planes and screw dislocations. They also may contain chemical impurities like iron and other transition metals [50].

- Kish graphite: this synthetic type is obtained by cooling a carbon-saturated iron melt, and then purifying the graphite in flowing halogen gas at high temperature. Kish graphite flakes are often larger than natural graphite flakes, which makes kish graphite the chosen material when large single-crystal flakes are needed. However, like natural graphite these samples may contains chemical impurity [64].

- Highly Oriented Pyrolytic Graphite (HOPG): nowadays these samples are the most commonly used high-quality graphitic material. The HOPG is prepared by the pyrolysis of hydrocarbons above 2000 °C and the resulting pyrolytic carbon is subsequently heat treated to higher temperature to improve its crystalline order. When stress annealed above 3300 °C, the HOPG exhibits electronic, transport, thermal, and mechanical properties close to those of single-crystal graphite, showing a very high degree of c-axis alignment [50, 49].

Elasticity in Graphite

The elastic behavior of a completely asymmetric material is specified by 21 independent elastic constants, while for an isotropic material, the number is reduced to 2. In between these limits the necessary number is determined by the symmetry of the material. In case of hexagonal crystals (graphite) the number of the second order elastic constants is 5.
The elastic constants in graphite fall in three groups depending on which bonding type is mainly involved:

	Second Order Elastic Constants C_{ij} (GPa):					
	C_{11}	C_{12}	C_{33}	C_{44}	C_{13}	$C_{11}+C_{12}$
Trickey [71]	—	—	13	—	—	—
Hasegawa [72]	—	—	30.4	—	—	—
Yin [70]	—	—	54	—	—	—
Boettger [69]	—	—	40.8	—	-0.5	1279.6
Jansen [73]	—	—	56	—	-12	1430
Mounet [68]	1118	235	29	4.5	-2.8	1353
Blakslee [56]	1060 ± 20	180 ± 20	36.5 ± 1	$0.018 - 0.035$	15 ± 5	1240 ± 40
Zhao [60]	—	—	—	—	22 ± 2	—
Grimsditch [57]	—	—	—	5.05 ± 0.35	—	—
Rev. Exp. [74]	1060 ± 20	180 ± 20	36.5 ± 1	5.05 ± 0.35	7.9 ± 3.5	1240 ± 40

Table 3.1: The second order elastic constants. The bottom (top) side of the table is referring to the experimental results (theoretical results: density functional theory within LDA approximation). The last column is the revised experimental elastic constant that are belied to be the most reliable [74].

C_{11}, C_{12}: sp^2 bonding interactions within the graphene planes
C_{33}, C_{44}: π bonding between planes
C_{13} : sp^2 bonding interactions within the graphene planes with respect to the π bonding between planes

The most complete experimental study on the graphite elastic constants is the work of Blakslee *et al.* [56]. These authors have determined the full sets of second order elastic constants by ultrasonic, sonic resonance and static test methods.

The graphite samples used by Blakslee *et al.* were turbostratic graphite (plane randomly oriented[2]). Pyrolytic graphite was annealed under a compressive stress perpendicular to the basal plane in order to promote crystalline growth (up to $20 - 50\ \mu m$) and aligns within $0.1^\circ - 0.5^\circ$ along the c-axis.

Among the 5 elastic constants found by Blakslee *et al.*, two of them (C_{44}, C_{13}) have been revised [74].

The reported values for C_{44} ranged from 0.018 to 0.035 GPa [56]. Baker *et al* [75] have shown that these low values are due to the gliding of basal dislocations (the Peierls stress or these dislocation is quasi zero [54]). These

[2]Because second order elasticity is isotropic in the basal plane, the random plane orientations does not affect the elastic constants [56]. This isotropy does not extend to the third-order elastic constant [74].

authors have shown that a light dose of neutron irradiation at relatively low-temperature pins the dislocations and thereby increase the C_{44} value up to 5.05 ± 0.35 GPa [57, 58]. The latter elastic constant is the revised value for C_{44}.
A new value for C_{13} was proposed by Zhan *et al* [60]. In this work X-ray diffraction data have been obtained on polycrystalline graphite and using the linear bulk modulus the authors suggested a higher value of C_{13} of 22 ± 2 GPa. Unfortunately they inadvertently used the expression for the planar bulk modulus and not the linear bulk modulus. If their procedure was carried through correctly, the value of C_{13} is lowered to 7.9 ± 3.5 GPa [74]. The latter elastic constant is the revised value for C_{13}.
In Table 3.1 are resumed the second order elastic constants measured using different experimental techniques (bottom side of the table) and calculated within the local density functional theory (top side of the table). The last column resume the revised experimental elastic constants that are believed to be the most reliable [74].
As I pointed out in the introduction, the value of the C_{13} elastic constant is positive (negative) for experimental (theoretical) studies, respectively.

3.3 Elastic Constants in Graphite

The elastic energy per unit volume w of a crystal under strain ε_i can be Taylor expanded in powers of the strain tensor in the following way:

$$w = \frac{1}{2!}\sum_{i=1}^{6}\sum_{j=1}^{6} C_{ij}\varepsilon_i\varepsilon_j + \frac{1}{3!}\sum_{i=1}^{6}\sum_{j=1}^{6}\sum_{k=1}^{6} C_{ijk}\varepsilon_i\varepsilon_j\varepsilon_k \tag{3.1}$$

where C_{ij}, C_{ijk} are the second and third order elastic constants respectively and ε_i are the components of the strain vector $\vec{\varepsilon} = (\varepsilon_1, \varepsilon_2, \varepsilon_3, \varepsilon_4, \varepsilon_5, \varepsilon_6)$. The latter equation is called the Lagrangian strain energy.
For hexagonal graphite I have 15 independent elastic constants (5 second order and 10 third order), while the remaining constants are related to them by crystal symmetries (see Table 3.2).
Thus the elastic energy per unit volume becomes:

$$w = +\frac{1}{2}\left(\varepsilon_1^2 + \varepsilon_2^2 + \frac{1}{4}\varepsilon_6^2\right) C_{11} + \left(\varepsilon_1\varepsilon_2 - \frac{1}{4}\varepsilon_6^2\right) C_{12} + \frac{1}{2}\varepsilon_3^2 C_{33} + (\varepsilon_1\varepsilon_3 + \varepsilon_2\varepsilon_3)\, C_{13}$$

$$+\frac{1}{2}\left(\varepsilon_4^2+\varepsilon_5^2\right)C_{44}+\frac{1}{2}\left(\frac{1}{3}\varepsilon_1^3+\frac{1}{2}\varepsilon_1^2\varepsilon_2+\frac{1}{2}\varepsilon_1\varepsilon_2^2+\frac{1}{3}\varepsilon_2^3\right)C_{111}+\frac{1}{6}\varepsilon_3^3 C_{333}$$
$$+\left(\frac{1}{2}\varepsilon_1^2\varepsilon_3+\varepsilon_1\varepsilon_2\varepsilon_3+\frac{1}{2}\varepsilon_2^2\varepsilon_3\right)C_{113}+\frac{1}{2}\left(-\varepsilon_1^2\varepsilon_2-2\varepsilon_1\varepsilon_2^2+\frac{1}{3}\varepsilon_2^3+\varepsilon_1\varepsilon_6^2\right)C_{166}$$
$$+\frac{1}{2}\left(\varepsilon_3\varepsilon_4^2+\varepsilon_3\varepsilon_5^2\right)C_{344}+\frac{1}{2}\left(\varepsilon_1\varepsilon_4^2+\varepsilon_2\varepsilon_5^2-\varepsilon_4\varepsilon_5\varepsilon_6\right)C_{144}+\frac{1}{2}\left(\varepsilon_1\varepsilon_3^2+\varepsilon_2\varepsilon_3^2\right)C_{133}$$
$$+\frac{1}{2}\left(-3\varepsilon_1^2\varepsilon_2-\varepsilon_1\varepsilon_2^2-\frac{1}{3}\varepsilon_2^3+\varepsilon_2\varepsilon_6^2\right)C_{266}+\frac{1}{2}\left(-4\varepsilon_1\varepsilon_2\varepsilon_3+\varepsilon_3\varepsilon_6^2\right)C_{366}$$
$$+\frac{1}{2}\left(e_2e_4^2+e_1e_5^2+e_4e_5e_6\right)C_{244} \tag{3.2}$$

The elastic constants are then calculated by applying different strains ε_i to the equilibrium lattice configuration. The primitive lattice vectors of the hexagonal graphite are defined by:

$$\begin{pmatrix} a_1 \\ a_2 \\ a_3 \end{pmatrix} = \begin{pmatrix} \frac{1}{2}a_0 & -\frac{\sqrt{3}}{2}a_0 & 0 \\ \frac{1}{2}a_0 & \frac{\sqrt{3}}{2}a_0 & 0 \\ 0 & 0 & c_0 \end{pmatrix} \tag{3.3}$$

where a_0, c_0 are the lattice parameters. Under strain the primitive vectors a_i are transformed into the new lattice vectors a_i' by:

$$\begin{pmatrix} a_1' \\ a_2' \\ a_3' \end{pmatrix} = \begin{pmatrix} a_1 \\ a_2 \\ a_3 \end{pmatrix}(I+\varepsilon) \tag{3.4}$$

where ε is the strain tensor[3] and I is the identity matrix. The strain tensor ε is linked with the strain components ε_i by:

$$\varepsilon = \begin{pmatrix} \varepsilon_1 & \frac{1}{2}\varepsilon_6 & \frac{1}{2}\varepsilon_5 \\ \frac{1}{2}\varepsilon_6 & \varepsilon_2 & \frac{1}{2}\varepsilon_4 \\ \frac{1}{2}\varepsilon_5 & \frac{1}{2}\varepsilon_4 & \varepsilon_3 \end{pmatrix} \tag{3.5}$$

Therefore for any strain tensor ε I get a relationship between the energy per unit volume and the elastic constants.
In hexagonal graphite I have 5 second order elastic constants and 10 third order elastic constants, giving a total of 15 unknown variables. Because

[3] I have used ε to denote the strain tensor, $\vec{\varepsilon}$ for the strain vector and ε_i to denote the strain components.

C_{11}	$C_{22} = C_{11}$	C_{111}	$C_{112} = C_{111} - C_{166} - 3C_{266}$
C_{12}	$C_{23} = C_{13}$	C_{113}	$C_{122} = C_{111} - 2C_{166} - 2C_{266}$
C_{13}	$C_{55} = C_{44}$	C_{133}	$C_{222} = C_{111} + C_{166} - C_{266}$
C_{33}	$C_{66} = \frac{1}{2}(C_{11} - C_{12})$	C_{333}	$C_{123} = C_{113} - 2C_{366}$
C_{44}		C_{144}	$C_{223} = C_{133}$
		C_{244}	$C_{233} = C_{133}$
		C_{344}	$C_{155} = C_{244}$
		C_{166}	$C_{255} = C_{144}$
		C_{266}	$C_{355} = C_{344}$
		C_{366}	$C_{456} = \frac{1}{2}(C_{244} - C_{144})$

Table 3.2: The symmetry of the elastic constants in hexagonal graphite. The odd columns contain the components of each constant that have been selected as independent and the even columns contain the relationship between them and the remaining non-zero components [62].

the 2^{nd} and 3^{rd} order elastic constants are uncoupled, I need at least 10 linear independent equations in order to determinate the full sets of elastic constants.
Before describing the calculation details, I have shown some simple relations between the elastic constants and the lattice parameters.

- $C_{11} + C_{12}$: Distortion that changes the size of the parameter lattice a_0 (changing the size of the basal plane)

$$e = (\delta_a, \delta_a, 0, 0, 0, 0) \qquad \longmapsto \qquad w = \frac{E}{V} = (C_{11} + C_{12}) \cdot \delta_a^2 \tag{3.6}$$

where $\delta_a = a/a_0$ represents the relative displacement with respect to the parameter lattice a_0. As the volume of the primitive unitcell is:

$$V = \frac{\sqrt{3}}{2} \cdot a_0^2 c_0 \tag{3.7}$$

the latter relationship can be rewritten as:

$$d\delta_a^2 = 2\frac{da^2}{a_0^2} \qquad \longmapsto \qquad C_{11} + C_{12} = \frac{1}{V}\frac{d^2E}{d\delta_a^2} = \frac{1}{\sqrt{3}c_0}\frac{d^2E}{da^2} \tag{3.8}$$

Therefore the sum $C_{11} + C_{12}$ represents how the energy changes with respect to the parameter lattice a_0.

- C_{33}: Distortion that changes the size of the parameter lattice c_0:

$$e = (0, 0, 0, 0, 0, \delta_c) \qquad \longmapsto \qquad w = \frac{E}{V} = \frac{1}{2} \cdot C_{33} \cdot \delta_c^2 \tag{3.9}$$

where $\delta_c = c/c_0$ represents the relative displacement with respect to the parameter lattice c_0. The latter relationship can be written as:

$$d\delta_c^2 = 2\frac{dc^2}{c_0^2} \qquad \longmapsto \qquad C_{33} = \frac{2}{V}\frac{d^2E}{d\delta_c^2} = \frac{2 \cdot c_0}{\sqrt{3}a_0^2}\frac{d^2E}{dc^2} \tag{3.10}$$

Therefore the elastic constants C_{33} represents how the energy changes with respect to the parameter lattice c_0.

- C_{13}: Distortion that changes the sizes of the lattice parameters a_0 and c_0 (preserves the symmetry but changes the volumes)

$$e = (\delta_a, \delta_a, 0, 0, 0, \delta_c) \quad \longmapsto \quad w = (C_{11} + C_{12})\,\delta_a^2 + \frac{1}{2}C_{33}\delta_c^2 + 2C_{13}\delta_a\delta_c \tag{3.11}$$

The latter relationship can be written as:

$$d\delta_a = \frac{da}{a_0}\ ,\ d\delta_c = \frac{dc}{c_0} \qquad \longmapsto \qquad C_{13} = \frac{1}{2V}\frac{d^2E}{d\delta_c d\delta_a} = \frac{1}{\sqrt{3}a_0}\frac{d^2E}{dadc} \tag{3.12}$$

Therefore the elastic constants C_{13} represents the second derive of the energy with respect to both the parameter lattices.

The second and third order elastic constants have been determined by applying different strain vector $\vec{\varepsilon}$ to the 4-atoms primitive unitcell. The strain vector used in this work have been chosen with the criteria that the relationships between strain energy and elastic constants is the simplest one. In this way it is easier to check the convergence for each elastic constant separately with respect to the calculations accuracy (k-points mesh, basis set sizes, cut-off energies) and sizes of the applied strains.
The strains chosen are listed in Table 3.3 where δ is the amount of uniaxial lattice distortion, with $\delta > 0$ in case of expansion and $\delta < 0$ in case of compression. The 1^{st} and 3^{rd} selected strains (rows in Table 3.3) are linearly dependent on the others and they are used to double-check the calculations. Then the elastic constants are found by fitting the strain energies w with the respective energy values obtained by *ab-initio* simulations.
The calculations are based on density functional theory in the local density approximation using the exchange-correlation functional as parametrized by Perdew and Wang [84]. Norm-conserving pseudopotentials with non-

ε	w	C_{ij}, C_{ijk}
$(0,0,0,\delta,\delta,0)$	$\delta^2 C_{44}$	C_{44}
$(\delta,0,0,0,0,0)$	$\frac{1}{2}\delta^2 C_{11} + \frac{1}{6}\delta^3 C_{111}$	C_{11}, C_{111}
$(0,0,0,0,0,\delta)$	$\frac{1}{4}\delta^2 C_{11} - \frac{1}{4}\delta^2 C_{12}$	C_{12}
$(0,0,\delta,0,0,0)$	$\frac{1}{2}\delta^2 C_{33} + \frac{1}{6}\delta^3 C_{333}$	C_{33}, C_{333}
$(0,\delta,0,0,0,0)$	$\frac{1}{2}\delta^2 C_{11} + \frac{1}{6}\delta^3 C_{111} + \frac{1}{6}\delta^3 C_{166} - \frac{1}{6}\delta^3 C_{266}$	C_{166}, C_{266}
$(\delta,\delta,0,0,0,0)$	$\delta^2 C_{11} + \delta^2 C_{12} + \frac{4}{3}\delta^3 C_{111} - \frac{4}{3}\delta^3 C_{166} - \frac{8}{3}\delta^3 C_{266}$	
$(\delta,0,0,\delta,0,0)$	$\frac{1}{2}\delta^2 C_{11} + \frac{1}{2}\delta^2 C_{44} + \frac{1}{6}\delta^3 C_{111} + \frac{1}{2}\delta^3 C_{144}$	C_{144}
$(\delta,0,0,0,\delta,0)$	$\frac{1}{2}\delta^2 C_{11} + \frac{1}{2}\delta^2 C_{44} + \frac{1}{6}\delta^3 C_{111} + \frac{1}{2}\delta^3 C_{244}$	C_{244}
$(0,0,\delta,\delta,0,0)$	$\frac{1}{2}\delta^2 C_{33} + \frac{1}{2}\delta^2 C_{44} + \frac{1}{6}\delta^3 C_{333} + \frac{1}{2}\delta^3 C_{344}$	C_{344}
$(0,0,\delta,0,0,\delta)$	$\frac{1}{4}\delta^2 C_{11} - \frac{1}{4}\delta^2 C_{12} + \frac{1}{2}\delta^2 C_{33} + \frac{1}{6}\delta^3 C_{333} + \frac{1}{2}\delta^3 C_{366}$	C_{366}
$(\delta,0,\delta,0,0,0)$	$\frac{1}{2}\delta^2 C_{11} + \delta^2 C_{13} + \frac{1}{2}\delta^2 C_{33} + \frac{1}{6}\delta^3 C_{111} + \frac{1}{2}\delta^3 C_{113} + \frac{1}{2}\delta^3 C_{133} + \frac{1}{6}\delta^3 C_{333}$	C_{13}
$(\delta,0,-\delta,0,0,0)$	$\frac{1}{2}\delta^2 C_{11} - \delta^2 C_{13} + \frac{1}{2}\delta^2 C_{33} + \frac{1}{6}\delta^3 C_{111} - \frac{1}{2}\delta^3 C_{113} + \frac{1}{2}\delta^3 C_{133} - \frac{1}{6}\delta^3 C_{333}$	C_{113}, C_{133}

Table 3.3: The Lagrangian strain energy w for each strain vector $\vec{\varepsilon} = (\varepsilon_1, \varepsilon_2, \varepsilon_3, \varepsilon_4, \varepsilon_5, \varepsilon_6)$. Each relationship is used to calculate the respective elastic constants showed in the third column.

local core corrections based on the Hartiwigsen-Goedecker-Hutter scheme [86] were used. The charge density is represented by a plane-wave basis in reciprocal space expanded up to 2000 Ryd while the Brillouin zone integrations are performed with a Monkhorst-Pack [32] scheme with mesh up to $128 \cdot 128 \cdot 16$ k-points. The basis sets employed consist of s, p and d Gaussian orbital functions with four exponents, centered at the atomic sites [85]. Typical basis set used are *pppp*, *pdpp*, *pddp*, *pdddp*.
Here the elasticity of graphite and graphene is studied using the basis set *pdpp*, a k-points mesh of $16 \cdot 16 \cdot 6$ and a charge density cut-off of 600 Ryd. Test calculation have shown that even if the total energy is 5 mRyd/atom higher than the convergence value (basis set *pdddp*, k-points mesh of $128 \cdot 128 \cdot 16$, charge density cut-off of 2000 Ryd), the lattice parameters and respective elastic constants are still well convergent (due to cancellation of errors between energy differences).
The lattice parameters found are $a = 2.444$ Å and $c = 6.63$ Å in good agreement with the respective experimental values $a = 2.452$ Å, $c = 6.67$ Å [60, 80, 81].
The calculated second-order elastic constant are shown in Table 3.4.
This work confirm the previous theoretical studies [68] and in general slightly improve the agreements with respect the revised experimental data. The elastic constants C_{11}, C_{12}, C_{44} and the value $C_{11} + C_{12}$ are well in agreement

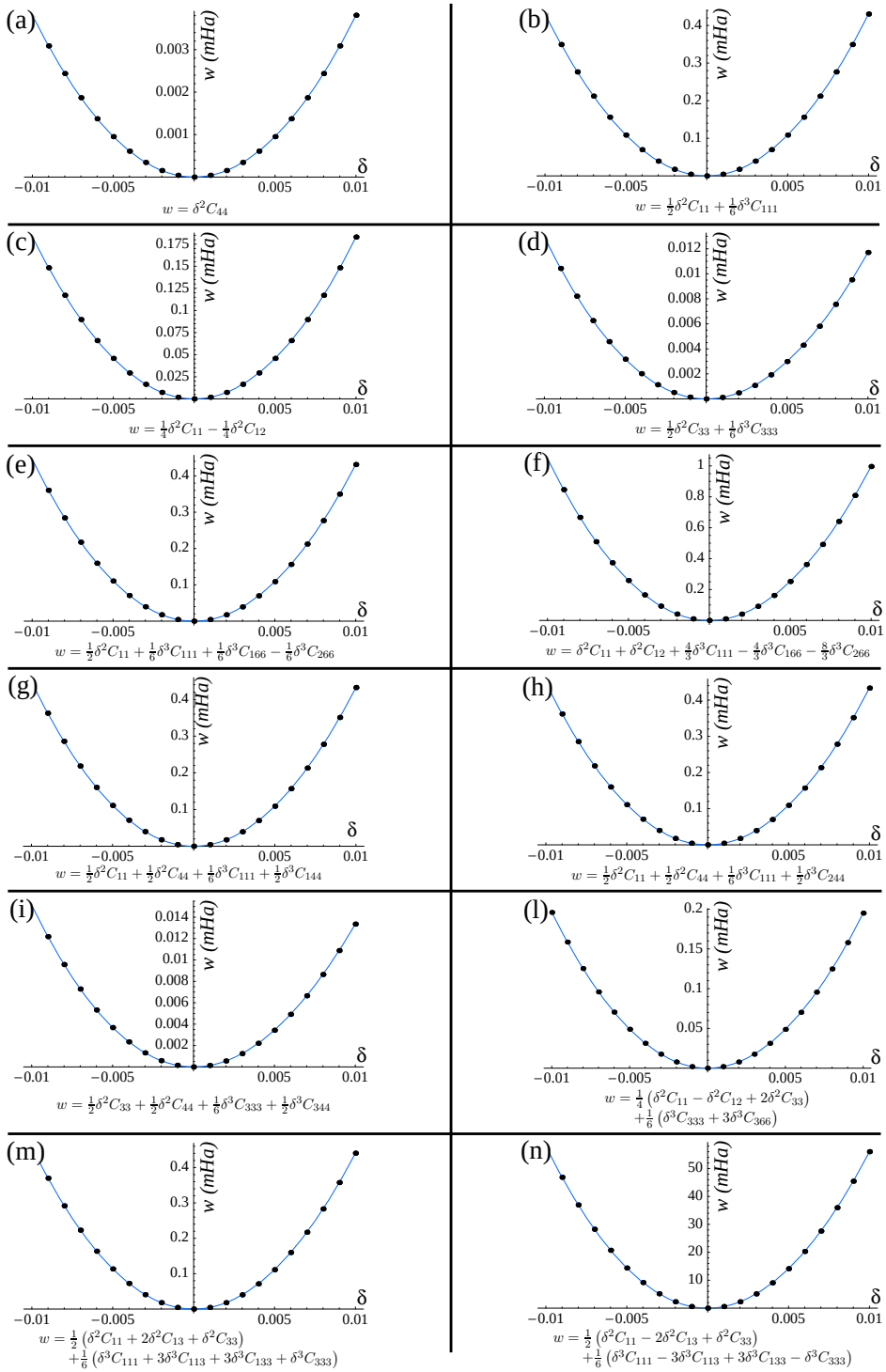

Figure 3.3: Strain energy per unit volume w as a function of the lattice distortion δ, for the twelve different strains defined in the Table 3.3. On the bottom of each picture is shown the relation strain w with respect to the chosen lattice distortions δ. The blue curves represent the functions $w(\delta)$ fitting the *ab-initio* data (black points).

	Second Order Elastic Constants C_{ij} (GPa):					
	C_{11}	C_{12}	C_{33}	C_{44}	C_{13}	$C_{11}+C_{12}$
Trickey [71]	—	—	13	—	—	—
Hasegawa [72]	—	—	30.4	—	—	—
Yin [70]	—	—	54	—	—	—
Boettger [69]	—	—	40.8	—	−0.5	1279.6
Jansen [73]	—	—	56	—	−12	1430
Mounet [68]	1118	235	29	4.5	−2.8	1353
Present work	1105	182	30.5	4.8	−2.3	1286.4
Rev. Exp. [74]	1060 ± 20	180 ± 20	36.5 ± 1	5.05 ± 0.35	7.9 ± 3.5	1240 ± 40

Figure 3.4: The resulting second-order elastic constants calculated via density functional theory within LDA approximations. In the bottom row are shown the revised experimental elastic constants [74] (the units are in GPa).

with the experiment while the value of C_{33} and in particular C_{13} show a remarkable difference of about 14% and 129%, respectively.
I observe than in graphite C_{33} is 36.5 GPa, a mere 3% of its diamond equivalent $C_{33} = C_{11} = 1215$ GPa, while the combination that relates to uniform strain within layers, $C_{11}+C_{12}$ is 1274 GPa in cubic diamond. Thus graphite is as stiff as diamond along the planes but 30 times more compliant between layers.
In diamond and semiconductor materials the theoretical and experimental elastic constants are in agreement within a range of ±15%. The temperature effect and/or the presence of point defects can easily explain the ±15% difference in values between theory and experiment, nevertheless a disagreement of 129% is far to be explained and a more elaborate explanation should be require.
Later in the last section of this chapter I will show that the values of the mesoscale elastic constant C_{33}^M and C_{13}^M are both in agreement with experiment within a range of ±11%.
At the present, no experimental data are available on the third-order elastic constants.
The ultrasonic and sonic resonance technique cannot measure the third-order elasticity of compression-annealed pyrolytic graphite. This material consists consists of layers that are stacked with high precision (c-axes parallel within 0.5°) but whose a-axis are distributed at random. In spite of this it is still possible to find the second order elastic constants because second order elasticity is isotropic in the basal plane, rendering the randomness invisible.

	Third Order Elastic Constants C_{ijk} (GPa):				
	C_{111}	C_{113}	C_{133}	C_{333}	C_{144}
Cousin *et al.*	-11690.5	-7.4	-120.0	-572.0	-8.6
present work	-6949.1	-10.8	103.4	-417.4	-2534.8
	C_{244}	C_{344}	C_{166}	C_{266}	C_{366}
Cousin *et al.*	-4.8	-74.7	-6786.8	972.0	3.4
present work	-2337.38	-66.3	-4618.3	90.7	158.3

Figure 3.5: The calculated third-order elastic constants compared with a previous study based on the empirical Keating model [74]. The calculated C_{113}, C_{333}, C_{344}, C_{166} are in agreement with the previous study within a range of $13-47\%$, while larger disagreements are found between the remaining elastic constants. These results suggest that at least one parameter used in the Keating model should be not reliable (the C_{ijk} units are in GPa).

This isotropy does not extend to the third order elastic constants. Since the latter are usually measured by determining the uniaxial stress dependence of ultrasonic wave velocities thought single crystals it is unlikely that they will be determined directly in the foreseeable future.
A possible way to measure the third-order elasticity is by compression of graphite powder following the changes in the lattice parameters by x-ray diffraction technique [63]. With this technique both second and third order elastic constants may be determined.
Table 3.5 show the third-elastic constants calculated in this work compared with the only previous study based on the empirical Keating model [74]. The calculated C_{113}, C_{333}, C_{344}, C_{166} are in agreement with the previous study within a range of $13-47\%$, while larger disagreement are found between the remaining elastic constants (up to 972% in case of C_{266}). In the Keating model the experimental second-order elastic constants, their pressure derivatives and the zone-centre optic mode frequencies are used as input parameters in order to determinate the third-order elasticity. The large disagreement found here suggest that at least one these parameters should be not reliable.

3.4 Mesoscale Elastic Properties of Graphene

3.4.1 Introduction

The recent discovery of graphene, a single planar layer of sp^2 bonded carbon atoms has struck the research community with its unusual properties and potential practical applications [**?**]. The true cause of the compelling interest is that graphene provides a powerful test-bed on which to explore the validity of some of the core concepts of solid-state physics.
Several years ago Peierls and Landau showed that thermal fluctuations should destroy the long-range order of any planar crystals and therefore a strictly two-dimensional crystal should not exist. Nevertheless graphene does exist and recent transmission electron images showed that its structure is not perfectly flat, but rather exhibits an intrinsic static roughening (bending) with an estimated height of about 1 nm and spatial length ranging from 1 nm to 25 nm [83].
Before to study the mesoscale elasticity of graphite, it is simplier to start the analysis with a single isolated graphite-plane (*i.e.* graphene).
The conclusion of this work will give new insight on the real physical structure of graphene.

3.4.2 The formation energy of a bent thin plate

In this section I study the energy of a thin bent plate. When I speak of a thin plate, I mean that its thickness is small compared with its dimensions in the other directions. We take a coordinate system with the origin on the surface of the thin plate with the z-axis normal to the surface. The xy-plane is that of the undeformed plate (see Figure 3.6).
I denote by ζ the vertical displacement of a point on the surface of the undeformed plate, *i.e.* its z coordinate. The components of its displacements in the xy-plane are evidently second order in ζ, and therefore I neglect them. Thus the components of the displacement vector for any point on the surface of the plate are:

$$u_x = u_y = 0 \qquad \text{and} \qquad u_z = \zeta\,(x, y)$$

The strain energy per unit volume w is the product of stress σ_{ij} times strain u_{ij} for each components,

$$w = \frac{1}{2}\sigma_{ij}u_{ij} \tag{3.13}$$

Within the isotropic elasticity the stress tensor is given in terms of the strain tensor by the following general relation:

$$\sigma_{ik} = \frac{E}{1+\sigma}\left(u_{ik} + \frac{\sigma}{1-2\sigma}u_{ll}\delta_{ik}\right) \tag{3.14}$$

where δ_{ik} is the Kronecker delta. In component form the stress tensor becomes:

$$\begin{cases} \sigma_{xx} &= \dfrac{E}{(1+\sigma)(1-2\sigma)}\left[(1-\sigma)u_{xx} + \sigma\left(u_{yy}+u_{zz}\right)\right] \\ \sigma_{yy} &= \dfrac{E}{(1+\sigma)(1-2\sigma)}\left[(1-\sigma)u_{yy} + \sigma\left(u_{xx}+u_{zz}\right)\right] \\ \sigma_{zz} &= \dfrac{E}{(1+\sigma)(1-2\sigma)}\left[(1-\sigma)u_{zz} + \sigma\left(u_{xx}+u_{yy}\right)\right] \\ \sigma_{xy} &= \dfrac{E}{(1+\sigma)}u_{xy} \\ \sigma_{xz} &= \dfrac{E}{(1+\sigma)}u_{xz} \\ \sigma_{yz} &= \dfrac{E}{(1+\sigma)}u_{yz} \end{cases} \tag{3.15}$$

where E is the Young modulus and σ is the Poisson ratio.
As the plate is thin, comparatively small forces on its surface are needed to bend it[4]. I can therefore neglect the forces on the surface, leaving

$$\sigma_{jk} \cdot n_k = 0 \tag{3.16}$$

Since the plate is only slightly bent, I can suppose that the normal vector n remains along the z-axis. Thus I must have on both the surfaces of the plate $\sigma_{xz} = \sigma_{yz} = \sigma_{zz} = 0$ and use these stress conditions to determine the components of the strain tensor.
Imposing the stress conditions I get

$$\begin{aligned} \sigma_{zx} = 0 \quad &\longmapsto \quad u_{zx} = 0 \\ \sigma_{zy} = 0 \quad &\longmapsto \quad u_{zy} = 0 \\ \sigma_{zz} = 0 \quad &\longmapsto \quad u_{zz} = -\frac{\sigma}{(1-\sigma)}\left(u_{xx}+u_{yy}\right) \end{aligned} \tag{3.17}$$

[4]Later I will apply forces only parallel to the plane and therefore this approximation will be further reinforced.

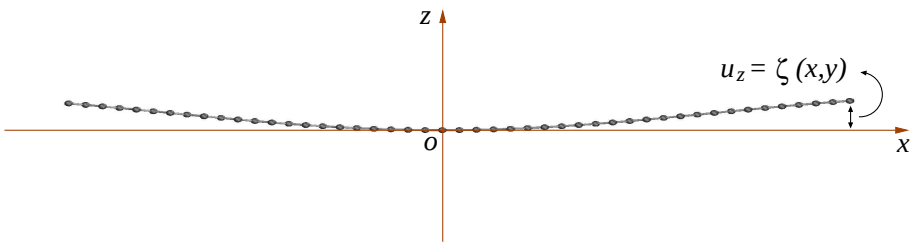

Figure 3.6: Bending of a graphene plane. The origin of the coordinate system is on the surface of the thin plate with the z-axis normal to the surface. The xy-plane is that of the undeformed plane. Each atom on the surface of the plane is displaced by $u_z = \zeta\,(x, y)$.

For small deformations, the strain tensor is given by the general equation:

$$u_{ik} = \frac{1}{2}\left(\frac{\delta u_i}{\delta x_k} + \frac{\delta u_k}{\delta x_i}\right) \tag{3.18}$$

thus from the first two of the equations **??**, I obtain

$$\frac{\delta u_x}{\delta z} = -\frac{\delta u_z}{\delta x} \qquad \text{and} \qquad \frac{\delta u_y}{\delta z} = -\frac{\delta u_z}{\delta y} \tag{3.19}$$

replacing u_z with $\zeta\,(x, y)$ I have,

$$u_x = -z \cdot \frac{\delta \zeta}{\delta x} \qquad \text{and} \qquad u_y = -z \cdot \frac{\delta \zeta}{\delta y} \tag{3.20}$$

where the constants of integration are set equal to zero in order to satisfy the following initial condition:

$$u_x = u_y = 0 \qquad \text{for} \qquad z = 0 \tag{3.21}$$

knowing u_x and u_y the components of the strain tensor are

$$\begin{cases} u_{xx} &= -z \cdot \dfrac{\delta^2 \zeta}{\delta x^2} \\ u_{yy} &= -z \cdot \dfrac{\delta^2 \zeta}{\delta y^2} \\ u_{zz} &= \dfrac{\sigma}{1-\sigma} \cdot z \cdot \left(\dfrac{\delta^2 \zeta}{\delta x^2} + \dfrac{\delta^2 \zeta}{\delta y^2} \right) \\ u_{xy} &= -z \cdot \dfrac{\delta^2 \zeta}{\delta x \delta y} \\ \\ u_{xz} &= u_{yz} = 0 \end{cases} \tag{3.22}$$

I can now determine the free energy w per unit volume of the plate:

$$\begin{aligned} w &= \frac{1}{2} \sigma_{ij} u_{ij} = \\ &= \frac{1}{2} \left(2 \cdot \sigma_{xx} u_{xx} + 2 \cdot \sigma_{yy} u_{yy} + 2 \cdot \sigma_{zz} u_{zz} + \sigma_{xy} u_{xy} + \sigma_{yx} u_{yx} \right) = \\ &= \frac{E}{(1+\sigma)(1-2\sigma)} \left[(1-\sigma) u_{yy}^2 + \sigma \left(u_{xx} - \frac{\sigma}{1-\sigma} (u_{xx} + u_{yy}) \right) u_{yy} \right] \\ &\quad + \frac{E}{(1+\sigma)(1-2\sigma)} \left[(1-\sigma) u_{xx}^2 + \sigma \left(u_{yy} - \frac{\sigma}{1-\sigma} (u_{xx} + u_{yy}) \right) u_{xx} \right] \\ &\quad + \frac{E}{1+\sigma} \cdot u_{xy}^2 = \\ &= \frac{E}{1-\sigma^2} \left\{ (u_{xx} + u_{yy})^2 + 2(1-\sigma) \left[\frac{1}{2} \cdot u_{xy}^2 - u_{xx} u_{yy} \right] \right\} \end{aligned} \tag{3.23}$$

replacing the strain components u_{xx}, u_{yy} and u_{xy} I have

$$w = z^2 \frac{E}{1-\sigma^2} \left\{ \left(\frac{\delta^2 \zeta}{\delta x^2} + \frac{\delta^2 \zeta}{\delta y^2} \right)^2 + 2(1-\sigma) \left[\left(\frac{\delta^2 \zeta}{\delta x \delta y} \right)^2 - \frac{\delta^2 \zeta}{\delta x^2} \frac{\delta^2 \zeta}{\delta y^2} \right] \right\} \tag{3.24}$$

The total energy of the plate is obtained by integrating over the volume. The integration over z is from $-1/2\ h$ to $+1/2\ h$, where h is the thickness of the plate, and over the surface of the plate (xy plane). Therefore the total free energy of a deformed plate become

$$E_{bend} = \frac{E \cdot h^3}{24(1-\sigma^2)} \cdot \iint \left\{ \left(\frac{\delta^2 \zeta}{\delta x^2} + \frac{\delta^2 \zeta}{\delta y^2} \right)^2 + 2(1-\sigma) \left[\left(\frac{\delta^2 \zeta}{\delta x \delta y} \right)^2 - \frac{\delta^2 \zeta}{\delta x^2} \frac{\delta^2 \zeta}{\delta y^2} \right] \right\} dx dy \tag{3.25}$$

where the quantity ζ is the vertical displacement of any point on the plate. The bending modes of a graphene plate are periodic with a sine or cosine behavior depending on the initial conditions. Here I consider the simplest solution of the latter equation; a pure sinusoidal bending mode along only one direction (the x-axis):

$$u_z = \zeta(x,y) = \bar{a} \cdot \sin\left(\frac{2\pi \cdot x}{\lambda}\right) \tag{3.26}$$

where $\bar{a}$ is the amplitude[5] and λ is the wavelength of the bending mode. Later in section 3.4.5 I will demonstrate:

- the simplest solution is the lowest in formation energy (the fundamental one);
- the 1-dimensional bending is energetically favoured over 2-dimensional bending;

taking in account the solution of equation 3.26, the formation energy of a bent plate becomes

$$\begin{aligned} E_{bend} &= \frac{E \cdot h^3 \cdot \triangle y}{24\left(1-\sigma^2\right)} \int \left(\frac{\delta^2 \zeta}{\delta x^2}\right)^2 dx = \\ &= \frac{E \cdot h^3 \cdot \triangle y}{24\left(1-\sigma^2\right)} \left(-\frac{2\pi}{\lambda}\right)^4 \bar{a}^2 \int_0^{\lambda} \sin^2\left(\frac{2\pi \cdot x}{\lambda}\right) dx = \\ &= \frac{E \cdot h^3 \cdot \triangle y}{24\left(1-\sigma^2\right)} \left(-\frac{2\pi}{\lambda}\right)^4 \frac{\lambda}{2} \cdot \bar{a}^2 = \\ &= \frac{\pi^4 \cdot E \cdot h^3 \cdot \triangle y}{3\left(1-\sigma^2\right)} \cdot \frac{\bar{a}^2}{\lambda^3} \end{aligned} \tag{3.27}$$

Therefore the formation energy of a bent plate is proportional to

$$E_{bend} = Const \cdot \frac{\bar{a}^2}{\lambda^3} \qquad \text{with} \qquad Const = \frac{\pi^4 \cdot E \cdot h^3 \cdot \Delta y}{3\left(1-\sigma^2\right)} \tag{3.28}$$

where $\bar{a}$ is the amplitude and λ is the wavelength of the bending mode. From this result I can say that the most favourable bending mode will always possess the largest wavelength and the smallest amplitude.
In order to study the elasticity of a bent plate I need to correlate the amplitude $\bar{a}$ with the strain ε. In the next section I shall give the exact numerical relation and some useful approximate analytical solutions.

[5] I use $\bar{a}$ to indicate the amplitude while a to indicate the in-plane parameter lattice.

3.4.3 The relationship between amplitude and strain

The relationship between the amplitude $\overline{a}$ and the stress ε of a bent plane along the x-axis with wavelength λ is given by the following elliptical integral

$$\int_0^{\lambda} \sqrt{1 + \left(\frac{\delta\zeta(x)}{\delta x}\right)^2}\, dx = L_c \tag{3.29}$$

where $\zeta(x)$ is the function describing the displacement of the atoms on the basal plane along the $[10\overline{1}0]$ direction (the x-axis). The value of this integral corresponds to L_c, the arc length of the plate along the x direction.
In the general case the strain ε of a plate may contain two different components; the strain homogeneously applied on all the atoms of the plate ε_{bond} and the strain due only to the bending ε_{bend}.

- ε_{bond}: the homogeneous compression or expansion of the plate.
  In this case all the distance between atoms along the x-axis are equally compressed or expanded by the amount ε_{bond}.
- ε_{bend}: the compression due only to the bending.
  In this case all the atoms of the plate lie on a sinusoidal surface with the distance between atoms along the x-axis unchanged. The compression ε_{bend} is due only to the bending with amplitude $\overline{a}$ and wavelength λ.

Therefore the total strain ε applied to the plate is the sum over the two components: $\varepsilon = \varepsilon_{bond} + \varepsilon_{bend}$. The bending wavelength becomes $\lambda = L \cdot (1 + \varepsilon)$ and the arc length is $L_c = L \cdot (1 + \varepsilon_{bond})$, where L indicates the length of the unstrained plane (along the x-axis).
Taking the simplest sinusoidal solution

$$\zeta(x) = \overline{a} \cdot \sin\left(\frac{2\pi \cdot x}{\lambda}\right) \tag{3.30}$$

equation 3.29 becomes

$$\int_0^{\lambda} \sqrt{1 + \left(\frac{2\pi \cdot \overline{a}}{\lambda} \cos\left(\frac{2\pi \cdot x}{\lambda}\right)\right)^2}\, dx = L_c \tag{3.31}$$

Although this integral has no analytical solution and therefore can be solved only in a numerical way I can still find useful approximate analytic solutions. Before discussing the approximate solutions of the latter equation let's see a useful property of the elliptical integral.

Proposition
Doubling the length L of the plane doubles the amplitude $\overline{a}$ and the wavelength λ. Expressed algebraically:

$$\begin{array}{cc} \textit{Hypothesis} & \textit{Thesis} \\ \\ \begin{array}{c} L' = 2L \\ \varepsilon'_{bend} = \varepsilon_{bend} \\ \varepsilon'_{bond} = \varepsilon_{bond} \end{array} \quad \Longrightarrow & \begin{array}{c} \lambda' = 2\,\lambda \\ \overline{a}' = 2\,\overline{a} \end{array} \end{array}$$

Demonstration:
The starting point is the the elliptical integral in the variables λ', L'_c, $\overline{a}'$, x'

$$\int_0^{\lambda'} \sqrt{1 + \left(\frac{2\pi \cdot \overline{a}'}{\lambda'} \cos\left(\frac{2\pi \cdot x'}{\lambda'}\right)\right)^2}\, dx' = L'_c \tag{3.32}$$

if I assume that $L' = 2L$ with the strain components ε_{bond}, ε_{bend} unchanged I automatically assume that also the arc length L_c and the wavelength λ are doubled:

$$\begin{aligned} L'_c &= L'\,(1 + \varepsilon'_{bond}) = 2L\,(1 + \varepsilon_{bond}) = 2L_c \\ \lambda' &= L'\,(1 + \varepsilon'_{bond} + \varepsilon'_{bend}) = 2L\,(1 + \varepsilon_{bond} + \varepsilon_{bend}) = 2\lambda \end{aligned} \tag{3.33}$$

Therefore the equation 3.32 becomes

$$\int_0^{2\lambda} \sqrt{1 + \left(\frac{2\pi \cdot \overline{a}'}{2\lambda} \cos\left(\frac{2\pi \cdot x'}{2\lambda}\right)\right)^2}\, dx' = 2L_c \tag{3.34}$$

changing the variable x in

$$x' = 2x \qquad \text{with} \qquad dx' = 2\,dx \tag{3.35}$$

I have

$$2\int_0^{\lambda} \sqrt{1 + \left(\frac{2\pi \cdot \overline{a}'}{2\lambda} \cos\left(\frac{2\pi \cdot x}{\lambda}\right)\right)^2}\, dx = 2L_c \tag{3.36}$$

the latter equation can only be satisfied if:

$$\overline{a}' = 2 \cdot \overline{a} \tag{3.37}$$

q.e.d

Now I try to find an approximate analytical solution of the elliptical integral,

$$\int_0^{\lambda} \sqrt{1 + \left(\frac{2\pi \cdot \overline{a}}{\lambda} \cos\left(\frac{2\pi \cdot x}{\lambda} \right) \right)^2} dx = L_c \tag{3.38}$$

For small values of $\overline{a}/\lambda \approx 0$ ($z \approx 0$) I can expand the square root in a Taylor series:

$$\sqrt{1+z^2} = 1 + \frac{z^2}{2} - \frac{z^4}{8} + \frac{z^6}{16} + O\left[z\right]^8 \tag{3.39}$$

taking the expansion to second order, the approximate elliptical integral becomes

$$\int_0^{\lambda} \left(1 + \frac{2\pi^2 \cdot \overline{a}^2}{\lambda^2} \cdot \cos^2\left(\frac{2\pi \cdot x}{\lambda} \right) \right) dx = L_c \tag{3.40}$$

with the following simple solution

$$\lambda + \frac{\pi^2}{\lambda}\overline{a}^2 = L_c \qquad \longmapsto \qquad \overline{a} = \frac{\sqrt{(L_c - \lambda)\,\lambda}}{\pi} \tag{3.41}$$

using the relations $\lambda = L \cdot (1 + \varepsilon)$ and $L_c = L \cdot (1 + \varepsilon_{bond})$ I get a simple relationship between the amplitude $\overline{a}$ and the strains ε, ε_{bend}:

$$\overline{a}_{2^{nd}} = \frac{\sqrt{(L_c - \lambda)\,\lambda}}{\pi} = \frac{L}{\pi}\sqrt{-\varepsilon_{bend}\,(1+\varepsilon)}$$

The latter equation represents the 2^{nd} order approximate solution. Taking the n^{th}-order expansion of the Taylor series (from the equation 3.39) I can find further, better approximations to the elliptical integral.
Here I list the 4^{th} and 6^{th} order approximate solutions:

$$\overline{a}_{4^{th}} = \frac{L}{\pi}\sqrt{\frac{2}{3}\,(1+\varepsilon)\left((1+\varepsilon) - \sqrt{(1+\varepsilon)\,(1+\varepsilon-3\varepsilon_{bend})}\right)} \tag{3.42}$$

$$\overline{a}_{6^{th}} = \frac{L}{\pi}\sqrt{\frac{1}{15}(1+\varepsilon)\left(3(1+\varepsilon) - \frac{17\cdot\sqrt[3]{9}(1+\varepsilon)^2}{\sqrt[3]{A}} + \sqrt[3]{3\cdot A}\right)} \tag{3.43}$$

where the term A is

$$A = -531(1+\varepsilon)^3 + 450(1+\varepsilon)^2(1-\varepsilon_{bend}+\varepsilon) + 10\sqrt{3}(1+\varepsilon)^2 \cdot \sqrt{989(1+\varepsilon)^2 - 1593(1+\varepsilon)(1-\varepsilon_{bend}+\varepsilon) + 675(1-\varepsilon_{bend}+\varepsilon)^2} \tag{3.44}$$

In table 3.4 I compare the different n^{th}-order approximations with respect to the exact numerical solution $\overline{a}$. As I increase the order of the approximation the calculation time increases. Later in the elastic analysis, test calculations have shown that the 6^{th}-order approximation is a good compromise between precision and calculation time. For simplicity in the following analysis I have used the simple 2^{nd}-order approximation.

	amplitude (Å)	$(\overline{a}_{n\,\text{order}} - \overline{a})/\overline{a}$
$\overline{a}_{2^{\text{nd}}}$	0.5220149858	$-2.638\cdot10^{-3}$
$\overline{a}_{4^{\text{th}}}$	0.5234121245	$+3.143\cdot10^{-5}$
$\overline{a}_{6^{\text{th}}}$	0.5233954186	$-4.875\cdot10^{-7}$
$\overline{a}_{8^{\text{th}}}$	0.5233956783	$+8.745\cdot10^{-9}$
$\overline{a}_{10^{\text{th}}}$	0.5233956736	$-1.496\cdot10^{-10}$
$\overline{a}$	0.5233956737	

Table 3.4: Different n^{th}-order approximate amplitudes with respect to the exact numerical solution $\overline{a}$. In the last column are shown the respective relative errors. As I increase the order of the Taylor series the approximate amplitude tends to the exact numerical solution. These approximations are better as much as the ratio $\overline{a}/\lambda$ is smaller. In these calculations the ratio $\overline{a}/\lambda$ is 0.027 (the plane length along the x-axis is $L = 19.7$ Å, while the strain components are $\varepsilon_{bend} = -0.007$ and $\varepsilon_{bond} = -0.003$).

3.4.4 The elasticity of a bended plate

The formation energy of a 1-dimensional bent plate along the x-axis is

$$E_{bend} = Const \cdot \frac{\bar{a}^2}{\lambda^3} \tag{3.45}$$

where the wavelength λ is related to the length of the plane L along the x direction by the relation $\lambda = L(1+\varepsilon)$. Taking the 2^{nd}-order approximation for the amplitude $\bar{a}$ I have

$$E_{bend} = \frac{\pi^4 \cdot E \cdot h^3 \cdot \triangle y}{3(1-\sigma^2)} \cdot \frac{\bar{a}^2}{\lambda^3} = \frac{\pi^4 \cdot E \cdot h^3 \cdot \triangle y}{3(1-\sigma^2)} \cdot \frac{1}{L^3(1+\varepsilon)^3} \cdot \frac{-L^2 \varepsilon_{bend}(1+\varepsilon)}{\pi^2} =$$

$$= \frac{\pi^2 \cdot E \cdot h^3 \cdot \triangle y}{3(1-\sigma^2)} \cdot \frac{-\varepsilon_{bend}}{L \cdot (1+\varepsilon)^2} = Const \cdot \frac{-\varepsilon_{bend}}{L(1+\varepsilon)^2} \tag{3.46}$$

the negative sign of the formation energy reflects the physical meaning of the bending; it is possible to bend only in compression region ($\varepsilon_{bend} < 0$). In the expanded region the energy becomes negative and lacks any physical meaning (the amplitude $\bar{a}$ becomes imaginary).
This simple relation show powerfully that for small deformations the formation energy of a thin bent plate is linearly proportional to the bending strain ε_{bend} and inversely proportional to the length of the plate L.
Then the total energy of the plate is the sum of the bending energy component E_{bent} and the energy due to the homogeneously compression or expansion of the plate E_{bond}:

$$E = E_{bend} + E_{bond} = Const \cdot \frac{-\varepsilon_{bend}}{L(1+\varepsilon)^2} + C_{11} \cdot \varepsilon_{bond}^2 \tag{3.47}$$

Therefore when I compress a graphene plane I can have the following three scenarios:

1. *Homogeneously compressed flat plate:* In this case all the atoms of the plate lie on the same plane and the distances between atoms along the x-axis are equally compressed. In this regime the formation energy of the graphene plane is:
$$E = C_{11} \cdot \varepsilon^2 \tag{3.48}$$

2. *Pure uncompressed bent plate:* In this case all the atoms of the plate lie on a sinusoidal surface with the bonds between atoms equal to the perfect graphene bond length. In this regime the formation energy of the graphene plane is:
$$E = Const \cdot \frac{-\varepsilon}{L(1+\varepsilon)^2} \tag{3.49}$$

3. *Homogeneously compressed bent plate:* In this case all the atoms of the plate lie on a sinusoidal surface with the distance between atoms along the x-axis equally compressed. In this regime the formation energy of the graphene plane is:

$$E = Const \cdot \frac{-\varepsilon_{bend}}{L\left(1+\varepsilon\right)^2} + C_{11} \cdot \varepsilon_{bond}^2 \tag{3.50}$$

with the condition that the total strain applied is $\varepsilon = \varepsilon_{bend} + \varepsilon_{bond}$.

The first and third regimes are shown in the Figure 3.7 (right and left respectively).
The question now that arise is:
"Is it possible to have a strain region in which I have a pure uncompressed bent plate?"
The answer is no and I proved it in the following:

Proposition
In small compression regime a thin plate is always homogeneously compressed (bent or flat), but is never a purely uncompressed bent plate.

Demonstration:
The general formula of the plate energy is

$$E = Const \cdot \frac{-\varepsilon_{bend}}{L\left(1+\varepsilon\right)^2} + C_{11} \cdot \varepsilon_{bond}^2 \tag{3.51}$$

for any values of the applied strain ε. The latter equation can be re-written in terms of the strains ε_{bend} and $\varepsilon = \varepsilon_{bond} + \varepsilon_{bend}$:

$$E\left(\varepsilon_{bend}\right) = Const \cdot \frac{-\varepsilon_{bend}}{L\left(1+\varepsilon\right)^2} + C_{11} \cdot \left(\varepsilon - \varepsilon_{bend}\right)^2 \tag{3.52}$$

now for any strain value ε I want to find the strain component ε_{bend} that minimizes the total energy $E\left(\varepsilon_{bend}\right)$. In formula I have to impose:

$$\frac{\delta E\left(\varepsilon_{bend}\right)}{\delta \varepsilon_{bend}} = 0 \qquad \text{with the condition} \qquad \frac{\delta^2 E\left(\varepsilon_{bend}\right)}{\delta \varepsilon_{bend}^2} > 0 \tag{3.53}$$

taking the first derivative of the energy with respect to the strain component ε_{bend} I have:

$$\frac{\delta E\left(\varepsilon_{bend}\right)}{\delta \varepsilon_{bend}} = 0 \qquad \longmapsto \qquad \varepsilon_{bend} = \varepsilon + \frac{Const}{2 \cdot L \cdot C_{11}\left(1+\varepsilon\right)^2} \tag{3.54}$$

while the second derivative of the energy with respect to the strain component ε_{bend} is:

$$\frac{\delta^2 E\left(\varepsilon_{bend}\right)}{\delta \varepsilon_{bend}^2} > 0 \qquad \longmapsto \qquad 2C_{11} > 0 \tag{3.55}$$

as the second derivative is always positive this solution minimizes the bending energy $E\left(\varepsilon_{bend}\right)$.
For simplicity I define a useful[6] constant K

$$K = \frac{Const}{2 \cdot L \cdot C_{11}} \tag{3.56}$$

As the terms $Const$, L, C_{11} are positive, so the constant K is always positive. Once I know the stress component ε_{bend} I automatically know also the stress components $\varepsilon_{bond} = \varepsilon - \varepsilon_{bend}$:

$$\begin{cases} \varepsilon_{bend} = \varepsilon + \dfrac{K}{\left(1+\varepsilon\right)^2} \\ \varepsilon_{bond} = -\dfrac{K}{\left(1+\varepsilon\right)^2} \end{cases} \qquad \forall\ \varepsilon \leq \varepsilon_{critical} \tag{3.57}$$

As the strain components ε_{bend} must be always negative[7] these equations represent a solution only when the total strain ε is under the critical value $\varepsilon_{critical}$. Above the critical strain I have $\varepsilon_{bend} = 0$ and therefore:

$$\begin{cases} \varepsilon_{bend} = 0 \\ \varepsilon_{bond} = \varepsilon \end{cases} \qquad \forall\ \varepsilon \geq \varepsilon_{critical} \tag{3.58}$$

where the critical strain $\varepsilon_{critical}$ is found imposing the condition $\varepsilon_{bend} = 0$

$$\varepsilon_{bend} = \varepsilon + \frac{K}{\left(1+\varepsilon\right)^2} = 0 \tag{3.59}$$

Re-writing the latter equation I have:

$$\varepsilon\left(1+\varepsilon\right)^2 + K = 0 \tag{3.60}$$

Imposing a real negative[8] solution I have:

[6] Later I will show that the critical strain $\varepsilon_{critical} \sim -K$ for small K.
[7] A positive value implies an imaginary amplitude with no physical meaning.
[8] Negative because I am in the compression region.

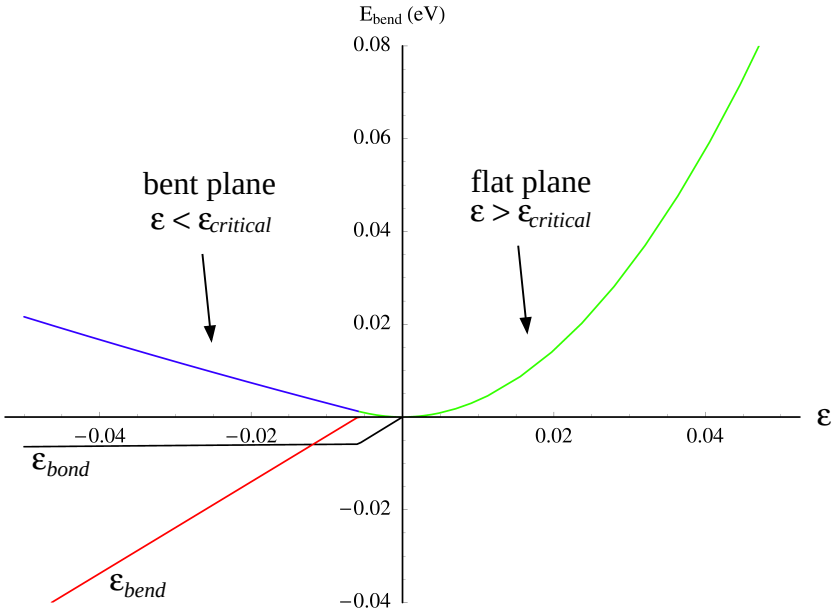

Figure 3.7: The formation energy of a graphene plane when compressed ($\varepsilon < 0$) or expanded ($\varepsilon > 0$). The green and blue curves represent the formation energies when the strain ε is above or under the critical strain $\varepsilon_{critical}$, respectively. The red line represents the strain component ε_{bend}, while the black line represents ε_{bond} (For simplicity both are shown only in the compression region).

$$\varepsilon_{critical} = -\frac{2}{3} + \frac{1}{3}\sqrt[3]{\frac{2}{2 - 27K + 3\sqrt{3}\sqrt{-4K + 27K^2}}} + \\ + \frac{1}{3}\sqrt[3]{\frac{2 - 27K + 3\sqrt{3}\sqrt{-4K + 27K^2}}{2}} \tag{3.61}$$

above the critical strain $\varepsilon_{critical}$ the plane is <u>flat</u> $\varepsilon_{bend} = 0$ and $\varepsilon_{bond} = \varepsilon$, while under the critical strain the plane starts to bend $\varepsilon_{bend} = \varepsilon - \varepsilon_{critical}$ and $\varepsilon_{bond} = \varepsilon_{critical}$.
Later I will show that in general the value of K is small, therefore I can expand the critical strain in a Taylor series and get the following approximate solution,

$$\varepsilon_{critical} = -K - 2K^2 - 7K^3 - 30K^4 - 143K^5 - 728K^6 + o\left(K^6\right) \tag{3.62}$$

$$\sim -K = -\frac{Cost}{2 \cdot L \cdot C_{11}} \tag{3.63}$$

Now I demonstrate that the plate is never a purely uncompressed bent plate. The proof is splits into two possible cases and demonstrated via *reductio ad absurdum* (in both cases the contradiction of the proposition is found):

1. Case: $\varepsilon \geq \varepsilon_{critical}$
   i.e. flat plate homogeneously compressed or expanded.

I suppose that the formation energy of a purely uncompressed bent plate is lower than the energy of a homogeneously compressed plate (left side of the following inequality):

$$\begin{aligned} C_{11}\varepsilon^2 &> Cost \cdot \frac{-\varepsilon}{L\left(1+\varepsilon\right)^2} \\ \varepsilon^2 &> \frac{Cost}{L \cdot C_{11}} \frac{-\varepsilon}{\left(1+\varepsilon\right)^2} \\ \varepsilon^2 &> -2\varepsilon \cdot \frac{K}{\left(1+\varepsilon\right)^2} \end{aligned} \tag{3.64}$$

If $\varepsilon \geq \varepsilon_{critical}$ I have the following relation (see equation 3.59):

$$\varepsilon_{bend} > 0 \qquad \longmapsto \qquad \frac{K}{\left(1+\varepsilon\right)^2} > -\varepsilon \tag{3.65}$$

therefore

$$\varepsilon^2 > -2\varepsilon \cdot \frac{K}{\left(1+\varepsilon\right)^2} > 2\varepsilon^2 \qquad \longmapsto \qquad 1 > 2 \tag{3.66}$$

The latter inequality is obviously impossible, therefore when $\varepsilon \geq \varepsilon_{critical}$ the plate is always homogeneously compressed or expanded.

2. Case: $\varepsilon \leq \varepsilon_{critical}$,
   i.e. bent and homogeneously compressed plate.

I suppose that exist a range of values ε where the formation energy of a pure uncompressed bended plane is lower than the energy of a homogeneously compressed bended plane (left member of the following inequity):

$$Const \cdot \frac{-\varepsilon_{bend}}{L\left(1+\varepsilon\right)^2} + C_{11} \cdot \left(\varepsilon_{bond}\right)^2 > Const \cdot \frac{-\varepsilon}{L\left(1+\varepsilon\right)^2} \tag{3.67}$$

using the relations of the equation 3.57 I have

$$Const \cdot \frac{-\varepsilon}{L\left(1+\varepsilon\right)^2} - Const \cdot \frac{K}{L\left(1+\varepsilon\right)^4} + C_{11} \cdot \frac{K^2}{\left(1+\varepsilon\right)^4} > Const \cdot \frac{-\varepsilon}{L\left(1+\varepsilon\right)^2}$$

$$-Const \cdot \frac{K}{L\left(1+\varepsilon\right)^4} + C_{11} \cdot \frac{K^2}{\left(1+\varepsilon\right)^4} > 0$$

$$K^2 - \frac{Const}{L \cdot C_{11}} \cdot K > 0$$

$$K^2 - 2K^2 > 0$$

$$-K^2 > 0 \tag{3.68}$$

The latter inequality is obviously impossible. Therefore a graphite plane cannot be a purely uncompressed bent plate but it is always homogeneously compressed.

q.e.d

3.4.5 Discussion

In this section I have summarise the results obtained so far and their generality. In particular I have shown:

1. The simplest solution is already the fundamental one *i.e.* the solution that minimizes the formation energy:

$$\zeta\left(x\right) = \overline{a} \cdot \sin\left(\frac{2\pi \cdot x}{\lambda}\right) \tag{3.69}$$

2. 1-dimensional bending is always more favourable than the 2-dimensional bending mode.

Summary of the results so far obtained: A graphene plane can be flat or bent depending on the value of the applied strain ε:

- *Above the critical strain:* $\varepsilon \geq \varepsilon_{critical}$

  The energy of the strained flat plane is:

$$E = C_{11} \cdot \varepsilon^2 \tag{3.70}$$

- *Under the critical strain:* $\varepsilon \leq \varepsilon_{critical}$

  The plane is bent and homogeneously compressed with energy:

$$E = Const \cdot \frac{-\varepsilon_{bend}}{L\left(1+\varepsilon\right)^2} + C_{11} \cdot \varepsilon_{bond}^2 \tag{3.71}$$

  with

$$\begin{cases} \varepsilon_{bend} = \varepsilon - \varepsilon_{critical} \\ \varepsilon_{bond} = \varepsilon_{critical} \end{cases} \qquad \forall\ \varepsilon \leq \varepsilon_{critical} \tag{3.72}$$

  using the latter relations I found another way to write the formation energy with respect to the critical strain $\varepsilon_{critical}$,

$$E = Const \cdot \frac{-\varepsilon + \varepsilon_{critical}}{L\left(1+\varepsilon\right)^2} + C_{11} \cdot \varepsilon_{critical}^2 \tag{3.73}$$

The formation energy describing the behavior of a graphene plane under *any* applied strain ε can be written as:

$$E = \left\{ Const \cdot \frac{-\varepsilon + \varepsilon_{critical}}{L\left(1+\varepsilon\right)^2} + C_{11} \cdot \varepsilon_{critical}^2 \right\} \cdot \vartheta\left(-\varepsilon + \varepsilon_{critical}\right) +$$

$$+ C_{11}\varepsilon^2 \cdot \vartheta\left(\varepsilon - \varepsilon_{critical}\right) \tag{3.74}$$

where I have used the Heaviside step function $\vartheta\left(x\right)$ defined by

$$\vartheta\left(x\right) = \begin{cases} 0 & x < 0 \\ 1/2 & x = 0 \\ 1 & x > 0 \end{cases} \tag{3.75}$$

Now I demonstrate the generality of the results found. The first step is the following:

Proposition
The simple solution

$$\zeta\left(x\right) = \overline{a} \cdot \sin\left(\frac{2\pi \cdot x}{\lambda}\right) \tag{3.76}$$

is already the fundamental general solution of the bent plate equation.

Demonstration:

The general solution of the equation 3.25 is periodic with respect to the wavelength λ.
Here for simplicity I discuss only 1-dimensional bending (along the x-axis). A general way to represent periodic functions is by the Fourier series: an expansion of a real function in sines and cosines terms such as

$$\zeta(x) = \frac{a_0}{2} + \sum_{n=1}^{\infty} a_n \cos\left(\frac{2\pi \cdot n \cdot x}{\lambda}\right) + \sum_{n=1}^{\infty} b_n \sin\left(\frac{2\pi \cdot n \cdot x}{\lambda}\right) \tag{3.77}$$

Imposing the boundary condition:

$$\zeta(0) = 0 \tag{3.78}$$

I have only the odd components,

$$\zeta(x) = \sum_{n=1}^{\infty} b_n \sin\left(\frac{2\pi \cdot n \cdot x}{\lambda}\right) \tag{3.79}$$

As the plane is homogeneous I can require that the positive and negative values of the function $\zeta(x)$ are symmetric[9]:

$$\zeta(x)|_{0 \le x \le \pi} = -\zeta(x)|_{\pi \le x \le 2\pi} \tag{3.80}$$

therefore only odd n are allowed. The general solution becomes:

$$\zeta(x) = b_1 \sin\left(\frac{2\pi \cdot x}{\lambda}\right) + b_3 \sin\left(3 \cdot \frac{2\pi \cdot x}{\lambda}\right) + b_5 \sin\left(5 \cdot \frac{2\pi \cdot x}{\lambda}\right) + b_7 \sin\left(7 \cdot \frac{2\pi \cdot x}{\lambda}\right) \ldots$$

$$= \sum_{n=1}^{\infty} b_{2n-1} \sin\left[(2n-1)\frac{2\pi \cdot x}{\lambda}\right] \tag{3.81}$$

where the first term represents the "carrier" wave while the following terms should be regarded as small corrections to the carrier wave.
The second derivative of the displacement function is:

$$\frac{\delta^2 \zeta(x)}{\delta x^2} = \sum_{n=1}^{\infty} b_{2n-1} \frac{\delta^2}{\delta x^2} \sin\left[(2n-1)\frac{2\pi \cdot x}{\lambda}\right] = \tag{3.82}$$

[9] This observation simplifies the mathematical handling of the equations. Nevertheless without this simplification, the following treatment remains valid with the same conclusions.

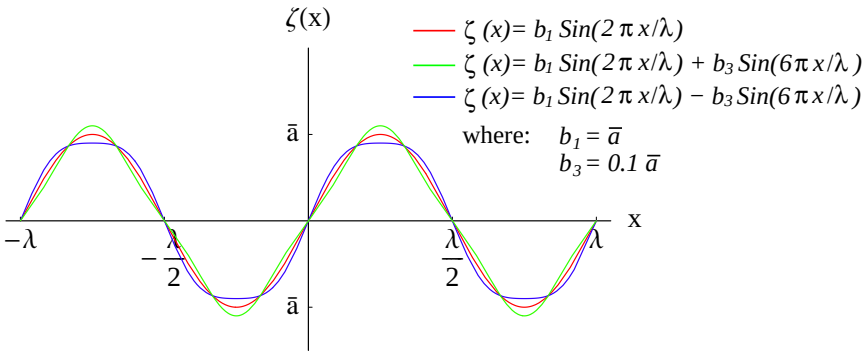

Figure 3.8: The displacement function $\zeta(x)$ for different values of the constants b_1 and b_3. The red function is the "carrier" wave. All the different displacement functions are solutions of the 2^{nd} order differential equation describing the bending energy, but only the fundamental one possesses the lowest energy.

$$= -\sum_{n=1}^{\infty} b_{2n-1} \left((2n-1) \cdot \frac{2\pi}{\lambda} \right)^2 \sin \left[(2n-1) \cdot \frac{2\pi \cdot x}{\lambda} \right] \tag{3.83}$$

Thus the formation energy of a bent plate becomes:

$$E_{bend} = \frac{E \cdot h^3 \cdot \triangle y}{24\left(1-\sigma^2\right)} \int_0^{\lambda} \left(\frac{\delta^2 \zeta\left(x\right)}{\delta x^2}\right)^2 dx =$$

$$= \frac{E \cdot h^3 \cdot \triangle y}{24\left(1-\sigma^2\right)} \int_0^{\lambda} \left(-\sum_{n=1}^{\infty} b_{2n-1} \left((2n-1)\cdot\frac{2\pi}{\lambda}\right)^2 \sin\left[(2n-1)\cdot\frac{2\pi\cdot x}{\lambda}\right]\right)^2 dx =$$

$$= \frac{E \cdot h^3 \cdot \triangle y}{24\left(1-\sigma^2\right)} \frac{8\pi^4}{\lambda^3} \sum_{n=1}^{\infty} b_{2n-1}^2 \left(2n-1\right)^4 =$$

$$= \frac{\pi^4 \cdot E \cdot h^3 \cdot \triangle y}{3\left(1-\sigma^2\right)} \cdot \frac{\sum_{n=1}^{\infty} b_{2n-1}^2 \left(2n-1\right)^4}{\lambda^3} =$$

$$= Const \cdot \frac{\sum_{n=1}^{\infty} b_{2n-1}^2 \left(2n-1\right)^4}{\lambda^3} \tag{3.84}$$

where the firsts few terms of the bending energy are:

$$E_{bend}\left(b_n\right) = Const \cdot \frac{1}{\lambda^3}\left(b_1^2 + 3^4 b_3^2 + 5^4 b_5^2 + 7^4 b_7^2 + 9^4 b_9^2 + 11^4 b_{11}^2 \ldots\right) \tag{3.85}$$

if only $b_1 \neq 0$, I re-find the earlier relationship

$$E_{bend} = Const \cdot \frac{\bar{a}^2}{\lambda^3} \qquad \text{with} \qquad \bar{a} = b_1 \tag{3.86}$$

Then the bending energy (equation 3.85) is minimized with respect to the constants b_i with the condition that the arc length along the x-axis is L_c:

$$\int_0^{\lambda} \sqrt{1 + \left(\frac{\delta\zeta\left(x\right)}{\delta x}\right)^2}\, dx = L_c \tag{3.87}$$

where the first derivative of the displacement function is

$$\frac{\delta\zeta\left(x\right)}{\delta x} = \sum_{n=1}^{\infty} b_{2n-1} \frac{\delta}{\delta x} \sin\left[(2n-1)\frac{2\pi\cdot x}{\lambda}\right] =$$

$$= \sum_{n=1}^{\infty} b_{2n-1} \left((2n-1)\cdot\frac{2\pi}{\lambda}\right) \cos\left[(2n-1)\cdot\frac{2\pi\cdot x}{\lambda}\right] \tag{3.88}$$

Minimizing the bending energy $E_{bend}\left(b_n\right)$ and requiring that arc length is equal to L_c I have found which set of b_n gives the lowest formation energy[10].

[10] As the arc length condition requires the solution of an elliptical integral (with no analytical expression), the minimization analysis was carried out precisely in a numerical way.

The minimization analysis was carried out numerically using a finite Fourier expansion ($n = 5, 10, 20, 50$) for several plane lengths ($L = 20, 40, 100, 2000$ Å) and strain components (ε_{bend}, ε_{bond} ranging from -0.1 to -0.001 with increment -0.001). In all the cases the most energetically favourable set b_n are:

$$b_1 \neq 0 \qquad \text{and} \qquad b_i = 0 \qquad i \geq 2 \tag{3.89}$$

The *physical meaning* of this result is the following:

> The bending energy is proportional to the curvature of the plane. As I increase the curvature I also increase the corresponding energy. The carrier wave $i = 1$ is the lowest curvature function while the following terms b_i increase the curvature and therefore the energy (see Figure 3.8). Therefore the fundamental solution is:

$$\zeta(x) = \overline{a} \cdot \sin\left(\frac{2\pi \cdot x}{\lambda}\right) \tag{3.90}$$

In order to get a mathematical feeling of this result I will prove it taking the simple 2^{nd} order approximation for the elliptical integral. Defining the following function $f(x)$:

$$f(x) = \sqrt{1 + \left(\frac{\delta\zeta(x)}{\delta x}\right)^2} \tag{3.91}$$

Its Taylor series when $b_n/\lambda \approx 0$ becomes:

$$\sqrt{1 + \left(\frac{\delta\zeta(x)}{\delta x}\right)^2} = \sum_{m=0}^{\infty} \frac{\delta^m f(0)}{\delta x^m} \left(\frac{\delta\zeta(x)}{\delta x}\right)^m =$$

$$= \sum_{m=0}^{\infty} \frac{\delta^m f(0)}{\delta x^m} \left(\frac{2\pi}{\lambda} \sum_{n=0}^{\infty} b_{2n-1}(2n-1) \cos\left[(2n-1) \cdot \frac{2\pi \cdot x}{\lambda}\right]\right)^m \tag{3.92}$$

Integrating the Taylor series the approximate elliptical integral becomes:

$$\int_0^{\lambda} \sqrt{1 + \left(\frac{\delta\zeta(x)}{\delta x}\right)^2} dx =$$

$$= \lambda + \int_0^{\lambda} \sum_{m=1}^{\infty} \frac{\delta^m f(0)}{\delta x^m} \left(\frac{2\pi}{\lambda} \sum_{n=1}^{\infty} (2n-1) \cdot b_{2n-1} \right)^m dx \tag{3.93}$$

taking the 2^{nd} order approximation of the elliptical integral and imposing that the arc length is equal to L_c I have

$$\lambda + \frac{\pi^2}{\lambda} \left(b_1^2 + 3^2 b_3^2 + 5^2 b_5^2 + 7^2 b_7^2 + 9^2 b_9^2 \ldots \right) = L_c$$

$$\left(b_1^2 + 3^2 b_3^2 + 5^2 b_5^2 + 7^2 b_7^2 + 9^2 b_9^2 \ldots \right) = \frac{(L_c - \lambda)\lambda}{\pi^2} = \bar{a}^2 \tag{3.94}$$

where the second member of this equation is called $\bar{a}^2$. Now the bending energy becomes:

$$E_{bend}(b_n) = Const \cdot \frac{1}{\lambda^3} \left(b_1^2 + 3^4 b_3^2 + 5^4 b_5^2 + 7^4 b_7^2 + 9^4 b_9^2 + 11^4 b_{11}^2 \ldots \right)$$

$$= Const \cdot \frac{1}{\lambda^3} \left(\bar{a}^2 + \left(3^4 - 3^2\right) b_3^2 + \left(5^4 - 5^2\right) b_5^2 + \left(7^4 - 7^2\right) b_7^2 + \ldots \right)$$

$$= Const \cdot \frac{1}{\lambda^3} \left(\bar{a}^2 + \sum_{n=2}^{\infty} \left((2n-1)^4 - (2n-1)^2 \right) \cdot b_n^2 \right) \tag{3.95}$$

as the sum terms are always positive, the only way to minimize the formation energy is to set $b_n = 0 \quad \forall\, n \neq 1$. Therefore

$$\bar{a} = b_1 \qquad \text{and} \qquad b_n = 0 \quad \forall\, n \neq 1 \tag{3.96}$$

and I re-find the physical meaning of amplitude of the simplest solution.

$$\zeta(x) = b_1 \cdot \sin\left(\frac{2\pi \cdot x}{\lambda} \right) = \overline{a} \cdot \sin\left(\frac{2\pi \cdot x}{\lambda} \right) \tag{3.97}$$

Therefore the latter solution minimizes the formation energy of a bent plane.

q.e.d

Proposition

The formation energy of 2-dimensional bending mode where bends are orthogonal to each other is double the formation energy of a 1-dimensional bending:

$$E_{bend}^{1d} = 2 \cdot E_{bend}^{2d}$$

Demonstration:
If I have two bending modes orthogonal to each other with the same wavelength λ the displacement function can be written:

$$\zeta(x,y) = \overline{a} \cdot \sin\left(\frac{2\pi \cdot x}{\lambda}\right) \cdot \sin\left(\frac{2\pi \cdot y}{\lambda}\right) \tag{3.98}$$

As the bending energy of a plate is

$$E_{bend}^{2d} = \frac{E \cdot h^3}{24(1-\sigma^2)} \cdot \int_0^{\lambda}\int_0^{\lambda} \left\{ \left(\frac{\delta^2\zeta}{\delta x^2} + \frac{\delta^2\zeta}{\delta y^2}\right)^2 + 2(1-\sigma)\left[\left(\frac{\delta^2\zeta}{\delta x \delta y}\right)^2 - \frac{\delta^2\zeta}{\delta x^2}\frac{\delta^2\zeta}{\delta y^2}\right] \right\} dxdy \tag{3.99}$$

The single terms of the integral are

$$\left(\frac{\delta^2\zeta}{\delta x^2} + \frac{\delta^2\zeta}{\delta y^2}\right)^2 = \left(-\frac{2^3\pi^2 \cdot \overline{a}}{\lambda^2} \cdot \sin\left(\frac{2\pi \cdot x}{\lambda}\right) \cdot \sin\left(\frac{2\pi \cdot y}{\lambda}\right)\right)^2 \tag{3.100}$$

$$\left(\frac{\delta^2\zeta}{\delta x \delta y}\right)^2 = \left(\frac{4\pi^2 \cdot \overline{a}}{\lambda^2} \cdot \cos\left(\frac{2\pi \cdot x}{\lambda}\right) \cdot \cos\left(\frac{2\pi \cdot y}{\lambda}\right)\right)^2 \tag{3.101}$$

$$-\frac{\delta^2\zeta}{\delta x^2}\frac{\delta^2\zeta}{\delta y^2} = -\frac{16\pi^4 \cdot \overline{a}^2}{\lambda^4} \cdot \sin^2\left(\frac{2\pi \cdot x}{\lambda}\right) \cdot \sin^2\left(\frac{2\pi \cdot y}{\lambda}\right) \tag{3.102}$$

The sum of the latter two terms is

$$\left(\frac{\delta^2\zeta}{\delta x \delta y}\right)^2 - \frac{\delta^2\zeta}{\delta x^2}\frac{\delta^2\zeta}{\delta y^2} = \frac{8\pi^4 \cdot \overline{a}^2}{\lambda^4} \cdot \cos\left(\frac{4\pi \cdot x}{\lambda}\right) \cdot \cos\left(\frac{4\pi \cdot y}{\lambda}\right) \tag{3.103}$$

as the integral is over the whole period λ of cosine functions this sum does not contribute to the total formation energy. Therefore the bending energy becomes (see equation 13):

$$E_{bend}^{2d} = \frac{E \cdot h^3}{24(1-\sigma^2)}\left(\frac{2^3\pi^2 \cdot \overline{a}}{\lambda^2}\right)^2 \int_0^{\lambda}\int_0^{\lambda} \sin^2\left(\frac{2\pi \cdot x}{\lambda}\right) \cdot \sin^2\left(\frac{2\pi \cdot y}{\lambda}\right) dxdy =$$

$$= \frac{E \cdot h^3}{24(1-\sigma^2)}\left(\frac{2^3\pi^2 \cdot \overline{a}}{\lambda^2}\right)^2 \frac{\lambda^2}{2^2} = \frac{\pi^2 \cdot E \cdot h^3}{3(1-\sigma^2)} \cdot \frac{2\overline{a}^2}{\lambda^2} \tag{3.104}$$

the latter equation represents the energy of a bent plate initially flat in the xy plane.

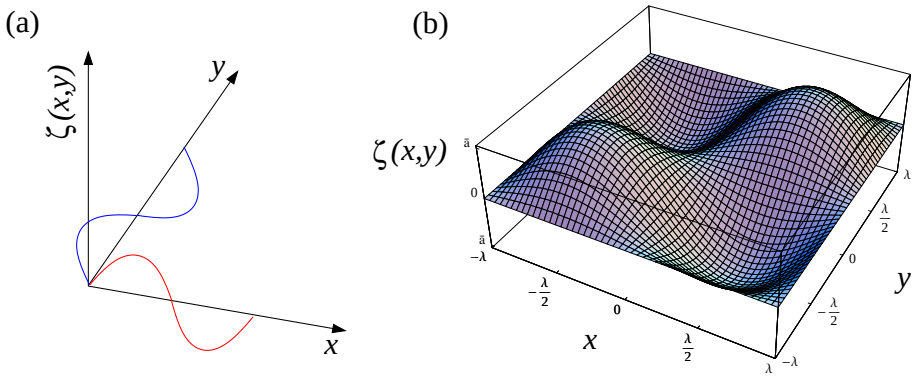

Figure 3.9: Two bending modes orthogonal to one an other. (a) Plot of two independent sine functions along the x (red curve) and y axis (blue curve). The combination of these two bending modes gives the following interference pattern: (b) Plot of the displacement function $\zeta(x, y)$ along the xy-plane.

The thickness of the plate along the z-axis is h while the wavelengths along the x, y directions are λ. Comparing with the formation energy of a 1-dimensional bent plate (see equation 3.28) with the same wavelength λ (along the x-axis) and sizes $\triangle y$ (along y-axis), h (along z-axis)

$$E_{bend}^{1d} = \frac{\pi^2 \cdot E \cdot h^3 \cdot \triangle y}{3\left(1-\sigma^2\right)} \cdot \frac{\overline{a}^2}{\lambda^3} \tag{3.105}$$

imposing the same length along the y-axis ($\triangle y = \lambda$) I have:

$$E_{bend}^{2d} = \frac{\pi^2 \cdot E \cdot h^3}{3\left(1-\sigma^2\right)} \cdot \frac{2\overline{a}^2}{\lambda^2} \tag{3.106}$$

$$E_{bend}^{1d} = \frac{\pi^2 \cdot E \cdot h^3}{3\left(1-\sigma^2\right)} \cdot \frac{\overline{a}^2}{\lambda^2} = 2 \cdot E_{bend}^{2d} \tag{3.107}$$

therefore the formation energy of 2-dimensionally bent plate is double that of a 1-dimensionally bent plate, *ceteris paribus*.

q.e.d

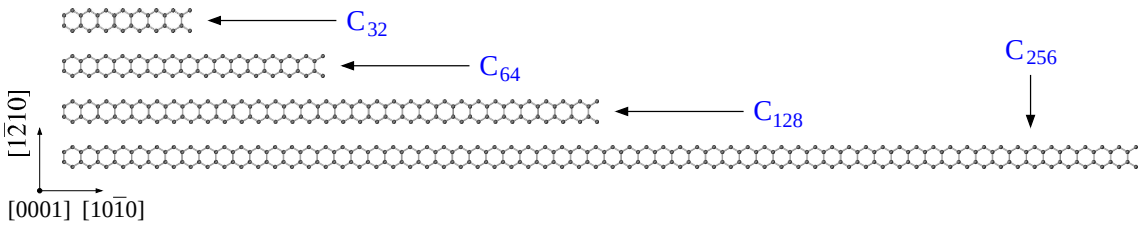

Figure 3.10: The mesoscale elastic properties of graphene are studied using different unitcell sizes. The stoichiometry of the unit cell are C_{32}, C_{64}, C_{128}, C_{256}.

3.4.6 Simulation of the mesoscale elasticity of graphene

In this section I have studied the mesoscale elasticity via density function theory and the meso-elastic theory previously developted.
The exchange-correlation energy is parametrized within the local density approximation using the Perdew and Wang functional [84]. The wavefunction basis sets used is *pdpp*, the same basis used previously for the *classical* elastic theory. Norm-conserving pseudopotentials based on the Hartiwigsen-Goedecker-Hutter scheme were used [86]. The charge density is represented by a plane-wave basis in reciprocal space expanded up to 600 Ryd. To perform the Brillouin zone integrations I use a Monkhorst-Pack scheme [?] with mesh $1 \times 10 \times 8$ k-points. In order to take into account the possible dispersion of the levels inside the band gap, a metallic filling is used, where the number of electrons at each k-point can differ.
I have used different unitcell size with stoichiometry C_{32}, C_{64}, C_{128}, C_{256} (see Figure 3.10). The unitcell lattice vectors are orthogonal between each other with length

$$\begin{cases} l_x = 8 \cdot a_0 \cdot (32 - n_{atom}) \\ l_y = \sqrt{3} \cdot a_0 \end{cases} \tag{3.108}$$

where n_{atom} is the number of atoms of each unitcells. Along the c-axis the distance between the unitcell and its image is set to 12 Å. The latter distance assure no interaction between the neighbour unitcells and at the same time a good compromise with its sizes[11].
The bending of the graphene plane is simulated by appling different strains ε_1 along the [1$\bar{2}$10] direction. The strains chosen are 21 ranging between ± 0.02 with increment 0.001.

[11] Increase the distance along the c-axis means larger vacuum regions and therefore longer computational time.

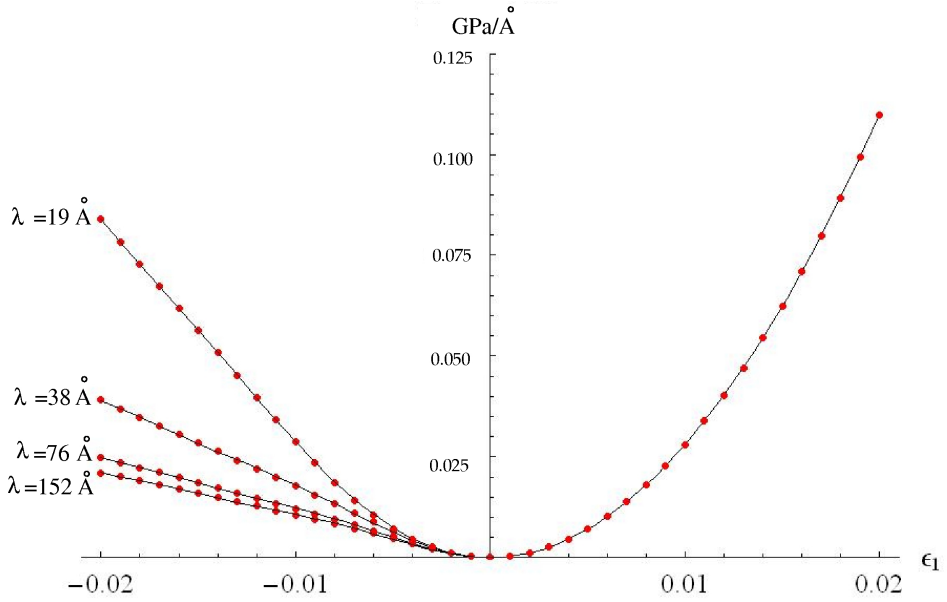

Figure 3.11: The formation energy per unit volume with respect to strain increments ε_1 along the $[1\bar{2}10]$ direction for the different unitcells shown in Figure 3.10. The linear behavior in the compression region is due to the bending of the planes.

In Figure 3.11 are shown the results. The red points represent the *ab-initio* formation energies of the respective unitcells (see Figure 3.10) while the black curves are the numerical results of the meso-elastic theory developted previously.
At the second-order approximation I have found that the formation energy describing the behaviour under any applied strain ε is:

$$E = \left\{ Const \cdot \frac{-\varepsilon + \varepsilon_{critical}}{L\left(1+\varepsilon\right)^2} + C_{11} \cdot \varepsilon_{critical}^2 \right\} \cdot \vartheta\left(-\varepsilon + \varepsilon_{critical}\right) + \\ + C_{11}\varepsilon^2 \cdot \vartheta\left(\varepsilon - \varepsilon_{critical}\right) \tag{3.109}$$

where C_{11} is the *classical* elastic constants (C_{11}=1100 GPa) while $Const$ represents the in-plane bending constant defined as:

$$Const = \frac{\pi^4 \cdot E \cdot h^3 \cdot \Delta y}{3\left(1-\sigma^2\right)} \tag{3.110}$$

as we do not know the Young modulus E and the Poisson ratio σ the value of the bending constant is found by interpolation the *ab-initio* data of the

	L_x	$\varepsilon_{critical}$	$E(\varepsilon_{critical})$	$E(\varepsilon_{critical}) \cdot \frac{L_x}{L_y}$
C_{32}	19 Å	0.022	0.532401	1.0648021
C_{64}	19 Å	0.0017	0.003190	0.0063580
C_{128}	19 Å	0.0003	0.000561	0.0011220
C_{512}	19 Å	0.00005	0.000003	0.0000055

Table 3.5: Critical strains and energies as a function of the different unit cell sizes. (1^{st} column) stoichiometry of the unitcell; (2^{nd} column) length L_x ; (3^{rd} column) critical formation energy; (4^{rd} column) the corresponding critical formation energy of a square graphite plane with size $L_x \cdot L_x$.

C_{32} unitcell. The resulting fitted value is $Const = 250$ GPa/Å^2. Then I have used this value to predict the behavior of longer unitcells C_{64}, C_{128}, C_{256}, C_{512}.
As showed in Figure 3.11 the agreement between the *ab-initio* data (black points) and analytic theory (blue curve) is excellent with a maximum error of $\pm 5 \cdot 10^{-4}$ eV. This neglectful disagreement can be further reduced up to $\pm 1 \cdot 10^{-4}$ eV by increasing the order of the approximation or better using the exact numerical value (as explained in section 3.4.3).
These results clearly show that under compression the graphene plane tend to bend as mush as we increase the length L_x.
The critical strain separating the homogeneously compressed flat plane (parabolic behaving in Figure 3.11) and the compressed bent plate (linear behaving in Figure 3.11) was defined as:

$$\varepsilon_{critical} = -\frac{2}{3} + \frac{1}{3}\sqrt[3]{\frac{2}{2 - 27K + 3\sqrt{3}\sqrt{-4K + 27K^2}}} + \\ + \frac{1}{3}\sqrt[3]{\frac{2 - 27K + 3\sqrt{3}\sqrt{-4K + 27K^2}}{2}} \tag{3.111}$$

where K is:

$$K = \frac{Const}{2 \cdot L_x \cdot C_{11}} \tag{3.112}$$

as the critical strain $\varepsilon_{critical}$ is in general a small number, a good approximation is its Taylor series:

$$\varepsilon_{critical} = -K - 2K^2 - 7K^3 - 30K^4 - 143K^5 - 728K^6 + o\left(K^6\right) \tag{3.113}$$

$$\sim -K = -\frac{Const}{2 \cdot L_x \cdot C_{11}} \tag{3.114}$$

In Table 3.5 is shown how the critical strain values $\varepsilon_{critical}$ and the respective formation energies $E(\varepsilon_{critical})$ for different length L_x along the bending direction [1010]. These results clearly show that the critical strain/energy decrease as much as we increase the length L_x (*i.e.* the wavelength).
The last column of Table 3.5 show the corresponding formation energy of a square graphite planes ($L_x = L_y$).
As the corresponding formation energy is much lower with respect to the ambient temperature energy ($\frac{3}{2}k_bT = 0.026$ eV) graphene plane at room temperature are always bent.
The latter conclusion have been recently confermend by an experimental work appeared in Nature last week (7 of March 2007).

3.5 Mesoscale Elastic Properties of Graphite

3.5.1 Introduction

In this section I will extent the mesoscale elasticity to the graphite case *i.e.* several graphene plane stacked along the c-axis.
The goal of this section is to describe the disregistry energy *i.e.* the interactions between bent planes.
Although weak this energy is of paramount importance in order to describe the full set of the mesoscale elastic constants.
This section is organized as follow:

Section 3.5.1: The disregistry $\triangle d$ between graphite planes.

Section 3.5.2: The corresponding disregistry energy $E^d(\varepsilon_3, \overline{a}, \lambda)$

Section 3.5.3: The mesoscale elastic constants C_{ij}^M

3.5.2 The disregistry energy

When several graphite planes are bent we always introduce locally a range of different stacking fault disregistries $\triangle d$ between the planes. The disregistry $\triangle d$ is defined with respect to the perfect AB stacking.
In Figure 3.12 is shown how the disregistry $\triangle d$ changes with respect to the plane slope. Each box depicted in Figure 3.12 represents different slope regions of bent graphite projected along the $\{10\bar{1}0\}$. These boxes are enlarged in Figure 3.13 and projected on the $\{0001\}$ plane.
For nearly flat plane the disregistry is $\triangle d \sim 0$ while when the slope is negative (positive) the disregistry $\triangle d$ becomes negative (positive), respectively. As the bending slope is proportional to the amplitude $\overline{a}$ and inversely proportional to the wavelength λ, we can expect that the modulus of the disregistry value $|\triangle d|$ should be proportional to the ratio $\overline{a}/\lambda$.

The disregistry function $\triangle d(\xi)$

In the following discussion I use Roman letters to describe functions (lines and trigonometric functions) and Greek letters to describe specific points (ξ, χ).
Recalling the fundamental solution of a bent plate along the x-axis (see equation 1.2) and replacing $\zeta(x)$ with $z(x)$, I have:

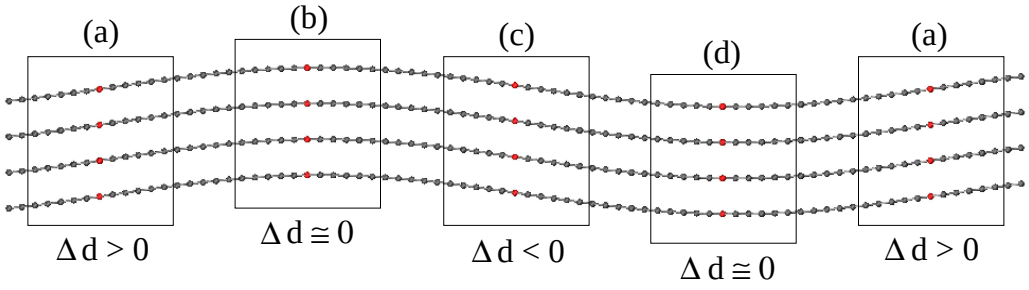

Figure 3.12: Perfect graphite bended along the [0001] direction. The boxes depicted show regions with different slopes. The top (b) and bottom (d) regions nearly conserve the perfect AB stacking $\triangle d \sim 0$ while the regions in between (a, c) show a noticeable stacking fault disregistry $\triangle d$.

$$z\left(x\right) = \overline{a} \cdot \sin\left(\frac{2\pi \cdot x}{\lambda}\right) \tag{3.115}$$

the latter equation represents the displacement functions of any points in a single plane. In graphite the planes are stacked along the [0001] direction (z-axis) with the well-know Bernard stacking fault AB (see Figure 3.13 caption b, d). As the distance between the plane is $c_0/2$, where c_0 is the lattice parameter, the displacement functions of any pair of bent graphite planes are:

$$\begin{cases} z_u(x) = \dfrac{1}{2}c_0 + \overline{a} \cdot \sin\left(\dfrac{2\pi \cdot x}{\lambda}\right) & (3.116) \\ z_l(x) = \overline{a} \cdot \sin\left(\dfrac{2\pi \cdot x}{\lambda}\right) & (3.117) \end{cases}$$

where the subscript u and l describe the upper and lower planes, $\overline{a}$ is the amplitude and λ is the wavelength of the bending mode.
The slope (or gradient) of the upper and lower planes is:

$$m(x) = \frac{\delta z_u(x)}{\delta x} = \frac{\delta z_l(x)}{\delta x} = \frac{2\pi \cdot \overline{a}}{\lambda} \cdot \cos\left(\frac{2\pi \cdot x}{\lambda}\right) \tag{3.118}$$

while the tangent $t_l(x)$ and normal $n_l(x)$ lines of the lower plane in the point ξ along the x-axis are:

$$\begin{cases} t_l(x) = z_l(\xi) + m(\xi) \cdot x & (3.119) \\ n_l(x) = z_l(\xi) - \dfrac{1}{m(\xi)} \cdot x & (3.120) \end{cases}$$

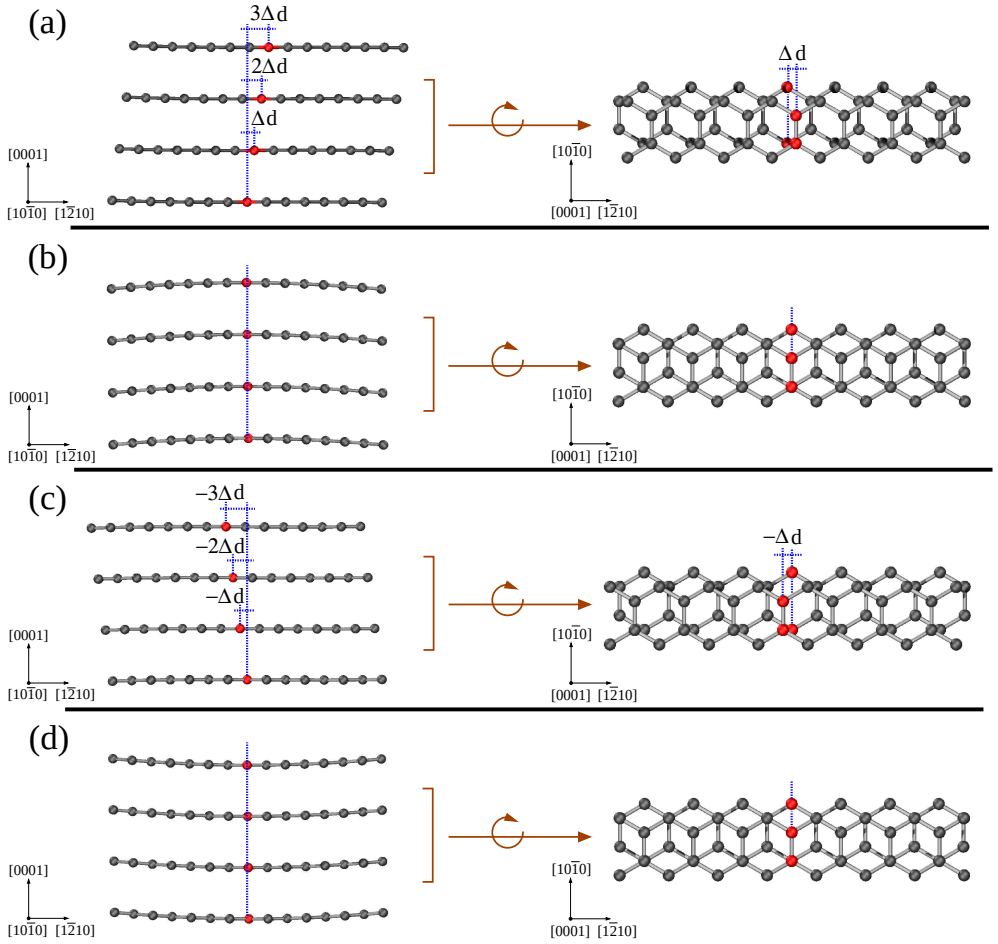

Figure 3.13: Different plane slopes correspond to different disregistries $\triangle d$. The four pictures (a-d) correspond to the box regions depicted in the previous figure. In each picture the disregistry $\triangle d$ corresponds to the distance between the lower and upper red atoms (center of each figure). Left: Projection on the $\{10\bar{1}0\}$ plane. Right: Projection on the $\{0001\}$ plane.

with $\xi \in [0, \lambda)$. The intersection point between the normal line $n_l(x)$ and the upper plane $z_u(x)$ is determined imposing:

$$z_u(x) = n_l(x) \qquad \longmapsto \qquad \overline{a} \cdot \sin\left(\frac{2\pi \cdot x}{\lambda}\right) + \frac{1}{m(\xi)} \cdot x + \frac{1}{2}c_0 - z_l(\xi) = 0 \tag{3.121}$$

the latter transcendental equation has no analytic solution and can be exactly solved only in a numerical way.

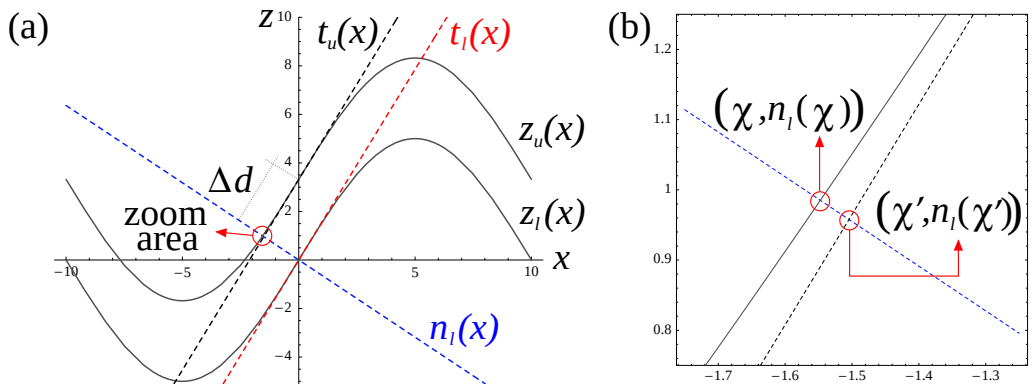

Figure 3.14: Geometrical construction of the disregistry $\triangle d$ in $\xi = 0$ (origin of the coordinate system). (a) The black $t_u(x)$ and red $t_l(x)$ dashed line are the tangent lines in $\xi = 0$ for the upper $z_u(x)$ and lower $z_l(x)$ plane respectively (black lines). The blue dashed line $n_l(x)$ is the normal line of the lower plane in $\xi = 0$. (b) Zoom of the cross area (red circle in caption a). The cross point $(\chi, n_l(\chi))$ is the intersection between the normal line $n_l(x)$ and the upper plane $z_u(x)$. The approximate cross point $(\chi', n_l(\chi'))$ is the intersection between the lower normal line $n_l(x)$ and the upper tangent line $t_u(x)$.

For simplicity, I have called this solution $(\chi, n_l(\chi))$, where $n_l(\chi)$ is:

$$n_l(\chi) = \frac{1}{2}c_0 + \overline{a} \cdot \sin\left(\frac{2\pi \cdot \chi}{\lambda}\right) \tag{3.122}$$

Now the disregistry Δd is defined as the distance between the cross point $(\chi, n_l(\chi))$ and $(\xi, z_u(\xi))$ by:

$$\Delta d(\xi) = \sqrt{(\chi - \xi)^2 + (n_l(\chi) - z_u(\xi))^2} \tag{3.123}$$

Then the transcendental equation 3.121 is solved in a numerical way and the disregistry $\Delta d(\xi)$ is calculated using the latter equation.
A convenient way to approximate the solution of the transcendental equation 3.121 is to approximate the values of $z_u(x)$ with its tangent line $t_u(x)$ at ξ. I have called this approximation as Δd approximation.
Therefore the approximate cross point is determined imposing $t_u(x) = n_l(x)$:

$$t_u(x) = n_l(x) \qquad \longmapsto \qquad z_u(\xi) + m(\xi) \cdot (x - \xi) = z_l(\xi) - \frac{1}{m(\xi)} \cdot (x - \xi) \tag{3.124}$$

with solution:

$$\chi'(\xi) = x = \xi + \frac{z_l(\xi) - z_u(\xi)}{m(\xi) + \frac{1}{m(\xi)}} = \xi - \frac{c_0}{2}\frac{m(\xi)}{1 + m(\xi)^2} \tag{3.125}$$

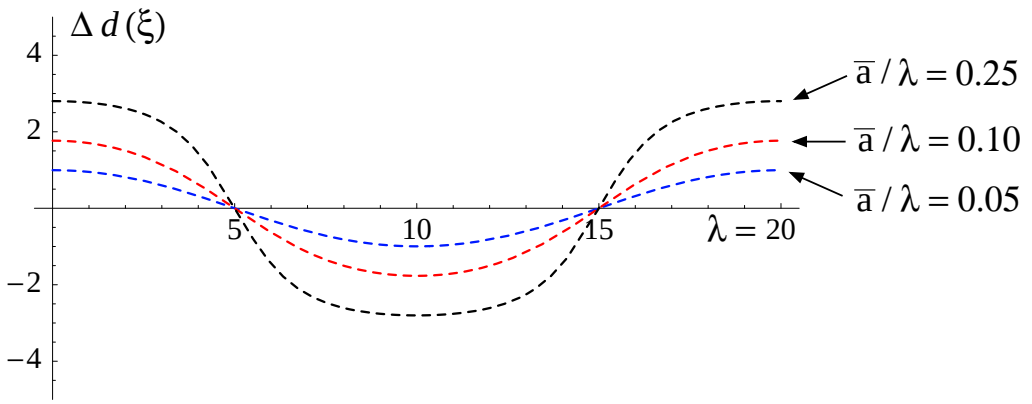

Figure 3.15: Disregistry function $\Delta d(\xi)$ for different $\overline{a}/\lambda$ ratio. For $\overline{a}/\lambda \sim 0$ the disregistry function is approaching a cosine function with amplitude $(\pi \cdot \overline{a} \cdot c_0)/\lambda$

where I have called this approximate cross point $\left(\chi^{'}, n_l\left(\chi^{'}\right)\right)$, where $n_l\left(\chi^{'}\right)$ is:

$$n_l(\chi^{'}) = z_l(\xi) - \frac{1}{m(\xi)} \cdot (\chi^{'} - \xi) = z_l(\xi) + \frac{c_0}{2}\frac{1}{1+m(\xi)^2} \tag{3.126}$$

Then the approximate disregistry $\Delta d(\xi)$ becomes:

$$\begin{aligned}
\Delta d(\xi) &= \sqrt{\left(\chi^{'} - \xi\right)^2 + \left(n_l\left(\chi^{'}\right) - z_u\left(\xi\right)\right)^2} = \\
&= \sqrt{\left(-\frac{c_0}{2}\frac{m\left(\xi\right)}{1+m\left(\xi\right)^2}\right)^2 + \left(z_l\left(\xi\right) + \frac{c_0}{2}\frac{1}{1+m\left(\xi\right)^2} - z_u\left(\xi\right)\right)^2} = \\
&= \sqrt{\left(-\frac{c_0}{2}\frac{m\left(\xi\right)}{1+m\left(\xi\right)^2}\right)^2 + \left(\bar{a}\cdot\sin\left(\frac{2\pi\cdot\xi}{\lambda}\right) + \frac{c_0}{2}\frac{1}{1+m\left(\xi\right)^2} - \frac{1}{2}c_0 - \bar{a}\cdot\sin\left(\frac{2\pi\cdot\xi}{\lambda}\right)\right)^2} = \\
&= \sqrt{\left(-\frac{c_0}{2}\frac{m\left(\xi\right)}{1+m\left(\xi\right)^2}\right)^2 + \left(+\frac{c_0}{2}\frac{1}{1+m\left(\xi\right)^2} - \frac{1}{2}c_0\right)^2} = \\
&= \sqrt{\left(-\frac{c_0}{2}\frac{m\left(\xi\right)}{1+m\left(\xi\right)^2}\right)^2 + \left(-\frac{c_0}{2}\frac{m\left(\xi\right)^2}{1+m\left(\xi\right)^2}\right)^2} = \\
&= \frac{c_0}{2}\sqrt{\frac{m\left(\xi\right)^2}{\left(1+m\left(\xi\right)^2\right)^2}\left(1+m\left(\xi\right)^2\right)} = \frac{c_0}{2}\frac{m\left(\xi\right)}{\sqrt{1+m\left(\xi\right)^2}}
\end{aligned} \tag{3.127}$$

where I have chosen the positive solution imposed by the condition $\Delta d(0) \geq 0$. Taking in account the slope $m(\xi)$:

$$m(\xi) = \frac{2\pi \cdot \overline{a}}{\lambda} \cdot \cos\left(\frac{2\pi \cdot \xi}{\lambda}\right) \tag{3.128}$$

I have found the general analytical formula $\Delta d(\xi)$:

$$\Delta d(\xi) = \frac{\pi \cdot \overline{a} \cdot c_0}{\lambda} \cdot \cos\left(\frac{2\pi \cdot \xi}{\lambda}\right) \frac{1}{\sqrt{1 + \left(\frac{2\pi \cdot \overline{a}}{\lambda} \cos\left(\frac{2\pi \cdot \xi}{\lambda}\right)\right)^2}} \tag{3.129}$$

this disregistry function $\Delta d(\xi)$ possesses the same periodicity λ of the bended graphite with an amplitude given by:

$$\Delta d(0) = \frac{\pi \cdot \overline{a} \cdot c_0}{\lambda} \cdot \frac{1}{\sqrt{1 + \left(\frac{2\pi \cdot \overline{a}}{\lambda}\right)^2}} \tag{3.130}$$

In Figure 3.15 I have showed the disregistry function $\Delta d(\xi)$ for different $\overline{a}/\lambda$ ratio. As the $\overline{a}/\lambda$ becomes smaller, the disregistry function tends to a cosine function with amplitude $(\pi \cdot \overline{a} \cdot c_0)/\lambda$.
Later in section 3.5.2 I have calculated the disregistry energy of a bent plane using the exact numerical solution and the approximate solution. I have found that the approximate solution is enough accurate to describe the disregistry energy.

The energy associated with the disregistry $\triangle d$ and ε_3

The disregistry function $\triangle d\,(\xi)$ represent the shear displacements between any couple of graphite planes in the ξ coordinate along the x-axis.
In this section I have studied the formation energies associated with the disregistry $\triangle d\,(\xi)$ and the strain ε_3 along the c-axis ([0001]direction).
The primitive lattice vectors of the 4 atoms unitcell are (blue lines in Figure 3.16):

$$\begin{pmatrix} a_1 \\ a_2 \\ a_3 \end{pmatrix} = \begin{pmatrix} \frac{1}{2}a_0 & -\frac{\sqrt{3}}{2}a_0 & 0 \\ \frac{1}{2}a_0 & \frac{\sqrt{3}}{2}a_0 & 0 \\ 0 & 0 & c_0 \end{pmatrix} \tag{3.131}$$

where a_0, c_0 are the graphite lattice parameters. In order to describe the elasticity of a bent plate I use the following orthogonal lattice vectors (brown lines in Figure 3.16):

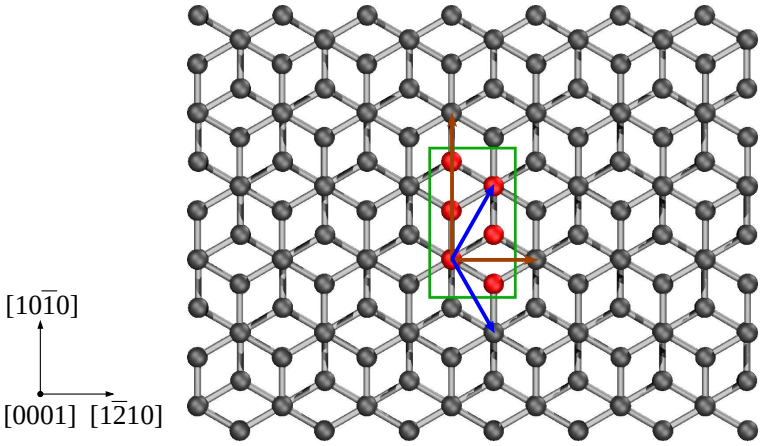

Figure 3.16: The primitive lattice vectors (blue line) of the 4 atoms unit cell (red atoms) and the lattice vectors (brown line) of 8 atoms the unitcell (green box). The latter unitcell is used to describe the mesoscale elastic properties.

$$\begin{pmatrix} a_1 \\ a_2 \\ a_3 \end{pmatrix} = \begin{pmatrix} a_0 & 0 & 0 \\ 0 & \sqrt{3}a_0 & 0 \\ 0 & 0 & c_0 \end{pmatrix} \tag{3.132}$$

these lattice vectors describe the 8 atoms unitcell highlighted by a green box in Figure 3.16. Under deformation these lattice vectors a_i are transformed into the new strained lattice vectors a_i' by:

$$\begin{pmatrix} a_1' \\ a_2' \\ a_3' \end{pmatrix} = \begin{pmatrix} a_1 \\ a_2 \\ a_3 \end{pmatrix} (I + \varepsilon) \tag{3.133}$$

where ε is the strain tensor and I is the identity matrix. In this case I want to describe how the formation energy of the system change with respect to the disregistry $\triangle d$ and the c_0 parameter lattice.
The new set of parameter lattice corresponding to the disregistry $\triangle d$ and the changed c parameter lattice correspond to the following strain tensor

$$\varepsilon = \begin{pmatrix} 0 & 0 & 0 \\ 0 & 0 & 0 \\ \varepsilon_5 & 0 & \varepsilon_3 \end{pmatrix} \tag{3.134}$$

and the new lattice vectors are:

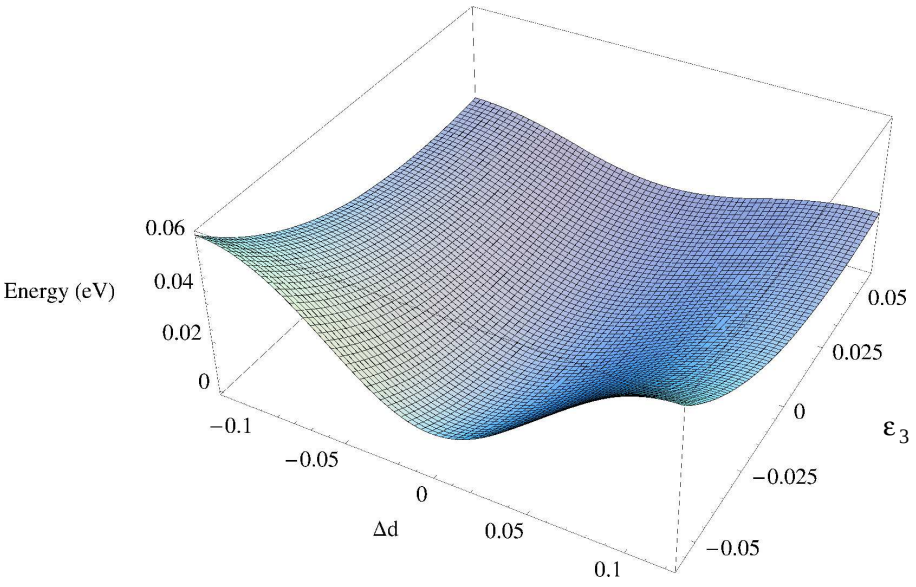

Figure 3.17: Energy surface with respect to the disregistry $\triangle d$ and the strain ε_3 applied along the c-axis ([0001] direction). This energy in referring to a unit cell of 8 host atoms AB graphite (green line in Figure 3.16).

$$\begin{pmatrix} a_1' \\ a_2' \\ a_3' \end{pmatrix} = \begin{pmatrix} a_1 \\ a_2 \\ a_3 \end{pmatrix} \begin{pmatrix} 1 & 0 & 0 \\ 0 & 1 & 0 \\ \varepsilon_5 & 0 & 1+\varepsilon_3 \end{pmatrix} = \begin{pmatrix} a & 0 & 0 \\ 0 & \sqrt{3}a & 0 \\ \varepsilon_5 & 0 & (1+\varepsilon_3)\cdot c_0 \end{pmatrix} \quad (3.135)$$

where the strain component ε_5 represent the disregistry $\triangle d$ and the component ε_3 describe the changing of the change the c_0 parameter lattice.
The disregistry $\triangle d$ is a periodic function along the $\left[1\bar{2}10\right]$ direction ($\triangle d\,(a) = \triangle d\,(0)$).
Thus in order to calculate the energy associated with this strain vector I have applied a grid of 26 displacements along $\left[1\bar{2}10\right]$ direction with increments 0.005 ranging from $\varepsilon_5 = 0.000$ to $\varepsilon_5 = 0.125$. For each of these displacement I have applied 24 strain ε_3 along [0001] direction with the same increment 0.005 ranging from $\varepsilon_3 = -0.060$ to $\varepsilon_3 = 0.060$.
The energies of each strained unitcells are calculated using density functional theory within the LDA approximation. The details of the calculations are the same as performed in section 3.1, except for the Brillouin zone integrations, where I have used a Monkhorst-Pack mesh of $16 - 10 - 8$ k-points instead of $16 - 16 - 8$ (as the lengths along the y lattice vector is $\sqrt{3}$ time larger than the primitive unit cell).
The energy surface with respect to the disregistry $\triangle d$ and the strain ε_3 is

shown in Figure 3.17.
Then this energy surface is fitted by a function of order $n+m$ defined by:

$$E^{fit}\left(\Delta d, \varepsilon_3\right) = \sum_{\alpha=0}^{n}\sum_{\beta=0}^{m} c_{\alpha,\beta} \cdot \left|\sin\left(\frac{\pi}{2}\frac{\Delta d}{a}\right)\right|^{\alpha} \cdot \varepsilon_3^{\beta} \cdot \delta_{\beta=1} \tag{3.136}$$

this function is a n-order power series of sine functions along the $[1\bar{2}10]$ direction and a m-order polynomial function along the [0001] direction (c-axis). The order of the function $E^{fit}\left(x,y\right)$ is then increased until the maximum error between fitted values and respective data are equal or less than the precision of the data themself (10^{-7}a.u.). In analytic form this requirement become:

$$\mathrm{Max}\left[\sum_{x=0.000}^{+0.125}\sum_{y=-0.060}^{+0.060}\left|E^{fit}(x,y) - data\left(x,y\right)\right|\right] \leq 10^{-7}\text{a.u.}$$

α	β										
	0	1	2	3	4	5	6	7	8	9	10
0	–	–	15.6310	-75.2299	+213.0540	-1.1534	2.1570	0.9877	1.0050	0.9998	0.9999
1	0.0035	0.0034	0.5786	-13.0148	70.0526	-0.0613	1.3869	0.9937	1.0017	0.9999	1.0000
2	0.0619	-1.0585	2.5517	1.4698	31.1676	0.1140	1.1740	0.9946	1.0008	1.0000	1.0000
3	0.4266	-1.6995	5.8002	6.2708	11.0443	0.1797	1.0646	0.9950	1.0003	1.0000	1.0000
4	0.9852	2.3557	1.6936	5.5687	1.1621	0.2113	0.9987	0.9952	1.0000	1.0000	1.0000
5	0.2827	0.8768	3.1384	3.0117	9.2054	0.2372	0.9558	0.9953	0.9998	1.0000	1.0000
6	1.7561	-2.0504	-5.1460	0.4432	14.7537	0.2672	0.9264	0.9956	0.9997	1.0000	1.0000
7	-0.8973	-1.8025	-3.8812	-1.4517	-18.6860	0.3032	0.9059	0.9958	0.9996	1.0000	1.0000
8	-2.3431	0.9025	-0.5485	-2.5695	-21.5204	0.3442	0.8913	0.9961	0.9996	1.0000	1.0000
9	0.3201	2.7241	3.0874	-3.0461	-23.5861	0.3884	0.8808	0.9963	0.9995	1.0000	1.0000
10	3.0260	1.4865	5.3378	-3.0819	-25.1025	0.4339	0.8733	0.9966	0.9995	1.0000	1.0000
11	0.7901	-1.9358	4.8840	-2.8633	-26.2208	0.4793	0.8679	0.9969	0.9995	1.0000	1.0000
12	-4.1948	-3.5775	0.8560	-2.5364	-27.0473	0.5235	0.8641	0.9972	0.9995	1.0000	1.0000
13	1.8728	2.6787	-7.2031	-2.2024	-27.6582	0.5658	0.8613	0.9974	0.9995	1.0000	1.0000

Table 3.6: Coefficient values $c_{\alpha,\beta}$ of the fitting function $E^{fit}(x,y)$. The values $c_{0,2}$ and $c_{0,3}$ correspond to the second order $\frac{1}{2}C_{33}$ and third order $\frac{1}{6}C_{333}$ elastic constants.

where $data\,(x,y)$ are the calculated energy values. I have found that $n=10$, $m=13$ reproduce the *ab-initio* data within the latter requirement. The coefficient values $c_{\alpha,\beta}$ of the function $E^{fit}\,(x,y)$ are listed in Table 3.6. In the next section I have calculated the disregistry energy of a bent plane.

The total disregistry energy of a bent plane

The mesoscale elastic properties have been studied using the basic 8 atoms unitcell (see green box in Figure 3.16) repeated n-time along the $[1\bar{2}10]$ direction. Therefore the studied unitcells have stoichiometry $C_{n\cdot 8}$ respectively. In this section I have calculated the disregistry energy for any n arbitrary unitcells using the exact value compared with the three different approximations.
The results so far found are:

1. The disregistry $\Delta d(\xi)$ for any ξ coordinate along the $[1\bar{2}10]$ direction. The exact numerical solution is found by solving the transcendental equation 3.121 and using the equation:

$$\Delta d(\xi)=\sqrt{(\chi-\xi)^2+\left(n_l(\chi)-z_u(\xi)\right)^2} \tag{3.137}$$

   The approximate analytic solution $\Delta d(\xi)$ is found using:

$$\Delta d(\xi)=\frac{\pi\cdot\overline{a}\cdot c_0}{\lambda}\cdot\cos\left(\frac{2\pi\cdot\xi}{\lambda}\right)\frac{1}{\sqrt{1+\left(\frac{2\pi\cdot\overline{a}}{\lambda}\cos\left(\frac{2\pi\cdot\xi}{\lambda}\right)\right)^2}} \tag{3.138}$$

   as the disregistry function $\Delta d(\xi)$ is defined with respect to the coordinate ξ, the strain ε_3, the amplitude $\overline{a}$ and the wavelength λ, I can write:

$$\Delta d(\xi,\varepsilon_3,\overline{a},\lambda)=\frac{\pi\cdot\overline{a}\cdot c_0\cdot(1+\varepsilon_3)}{\lambda}\cdot\frac{\cos\left(\frac{2\pi\cdot\xi}{\lambda}\right)}{\sqrt{1+\left(\frac{2\pi\cdot\overline{a}}{\lambda}\cos\left(\frac{2\pi\cdot\xi}{\lambda}\right)\right)^2}} \tag{3.139}$$

2. The energy associated with the disregistry $\Delta d(\xi,\varepsilon_3,\overline{a},\lambda)$ and the strain component ε_3 for each coordinate ξ along the $[1\bar{2}10]$:

$$E^{fit}\,(\xi,\varepsilon_3,\overline{a},\lambda)=\sum_{\alpha=0}^{n}\sum_{\beta=0}^{m}c_{\alpha,\beta}\cdot\left|\sin\left(\frac{\pi}{2}\frac{\Delta d(\xi,\varepsilon_3,\overline{a},\lambda)}{a}\right)\right|^{\alpha}\cdot\varepsilon_3^{\beta}\cdot\delta_{\beta=1} \tag{3.140}$$

	Total disregistry energy $E^d(\varepsilon_3, \overline{a}, \lambda)$			
approximation	$\lambda = a_0 \cdot 2^3$ Å	$\lambda = a_0 \cdot 2^4$ Å	$\lambda = a_0 \cdot 2^5$ Å	$\lambda = a_0 \cdot 2^6$ Å
Δd	0.01922566	0.00975695	0.00494696	0.00247348
Z.O.	0.01921577	0.00975571	0.00494680	0.00247346
Δd + Z.O.	0.01921576	0.00975571	0.00494680	0.00247346
E.N. solution	0.01922567	0.00975695	0.00494696	0.00247348
Relative error %	0.0515 %	0.0127 %	0.0032 %	0.0006 %

Table 3.7: The total disregistry energy $E^d(\varepsilon_3, \overline{a}, \lambda)$ with respect to the different approximations (Δd, Z.O.) and the exact numerical (E.N.) solution (In these calculation the amplitude is $\overline{a} = 0.20$ Å).

Now I have all I need in order to implement the disregistry energy $E^d(\varepsilon_3, \overline{a}, \lambda)$: The total disregistry energy $E^d(\varepsilon_3, \overline{a}, \lambda)$ represent is the sum of all the atom contributions of the disregistry energy $E^{fit}(\xi, \varepsilon_3, \overline{a}, \lambda)$ along the bent plane.

$$E^d(\varepsilon_3, \overline{a}, \lambda) = \sum_{i=1}^{n} E^{fit}(\xi, \varepsilon_3, \overline{a}, \lambda) \tag{3.141}$$

where n is the how many time the 8 atoms unitcell (see Figure 3.16) is repeat along the x-axis.
In the zero-order (Z.O.) approximation I assume that all the atoms along the bent plane possess the same distance along the x-axes. The Z.O. approximation always introduce an error because a bent plane always contract and expanded in a way that the distance between atoms are the same on the bent plane and not their projections on the x-axis. In the following discussion I evaluate the total disregistry energy $E^d(\varepsilon_3, \overline{a}, \lambda)$ for the Z.O. approximation compared with the exact numerical (E.N.) solution where the distances along the bent plane are the same.
In order to find the exact numerical solution we start to define the bond length along the $[1\bar{2}10]$ direction as:

$$bond = \sqrt{(\xi_{i+1} - \xi_i)^2 + (a/4)^2 + \left(\overline{a}\sin\left(\frac{2\pi \cdot \xi_{i+1}}{\lambda}\right) + \overline{a}\sin\left(\frac{2\pi \cdot \xi_i}{\lambda}\right)\right)^2} \tag{3.142}$$

where ξ_i is the position of the atom i on the plane. For simplicity I call the local displacement as: $\Delta\xi_{i+1} = (\xi_{i+1} - \xi_i)$. Solving (in a numerical way) the equation 3.142 with respect the variable local displacement:

$$\Delta\xi_{i+1}\left(\overline{a}, bond, \lambda\right) \tag{3.143}$$

I obtain the local displacement as a function of the amplitude $\overline{a}$, the bond length *bond* and the wavelength λ.
Now I impose the condition that the sum of $\Delta\xi_{i+1}$ over all the atom positions of the bent plane must be equal to the total wavelength λ of plane along x-axis:

$$\sum_{i=1}^{n} \Delta\xi_{i+1}\left(\overline{a}, bond, \lambda\right) = \lambda \qquad \text{per any } \bar{\text{a}} \tag{3.144}$$

By solving the latter equation I obtain the new bond length value and therefore the corresponding atomic positions ξ_i along the bent plane.
In Table 3.7 are reported the exactly numerical $\Delta d(\xi)$ for different values of the amplitude $\bar{a}$ and wavelength λ.

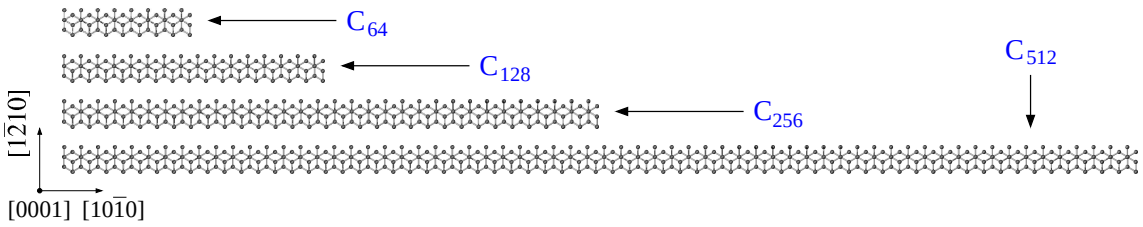

Figure 3.18: The mesoscale elastic properties of graphite are studied using different unitcell sizes. The stoichiometry of the unit cell are C_{64}, C_{128}, C_{256}, C_{512}.

3.5.3 Simulation of the mesoscale elasticity of graphite

In this section I have studied the mesoscale elasticity via density function theory compared with the meso-elastic theory. .
The exchange-correlation energy is parametrized within the local density approximation using the Perdew and Wang functional [84]. The wavefunction basis sets used is *pdpp*, the same basis used previously for the *classical* elastic theory. Norm-conserving pseudopotentials based on the Hartiwigsen-Goedecker-Hutter scheme were used [86]. The charge density is represented by a plane-wave basis in reciprocal space expanded up to 600 Ryd. To perform the Brillouin zone integrations I use a Monkhorst-Pack scheme [?] with mesh $1 \times 10 \times 8$ k-points. In order to take into account the possible dispersion of the levels inside the band gap, a metallic filling is used, where the number of electrons at each k-point can differ.
In the same way of the previous graphene study I have used different unitcell sizes with stoichiometry C_{64}, C_{128}, C_{256}, C_{512} (see Figure 3.18). The lattice vectors are orthogonal between each other with length:

$$\begin{cases} l_x = 8 \cdot a_0 \cdot (64 - n_{atom}) \\ l_y = \sqrt{3} \cdot a_0 \\ l_z = c_0 \end{cases} \tag{3.145}$$

where n_{atom} is the number of atoms of each unitcells.
The mesoscale elastic constants are determined by appling different strain

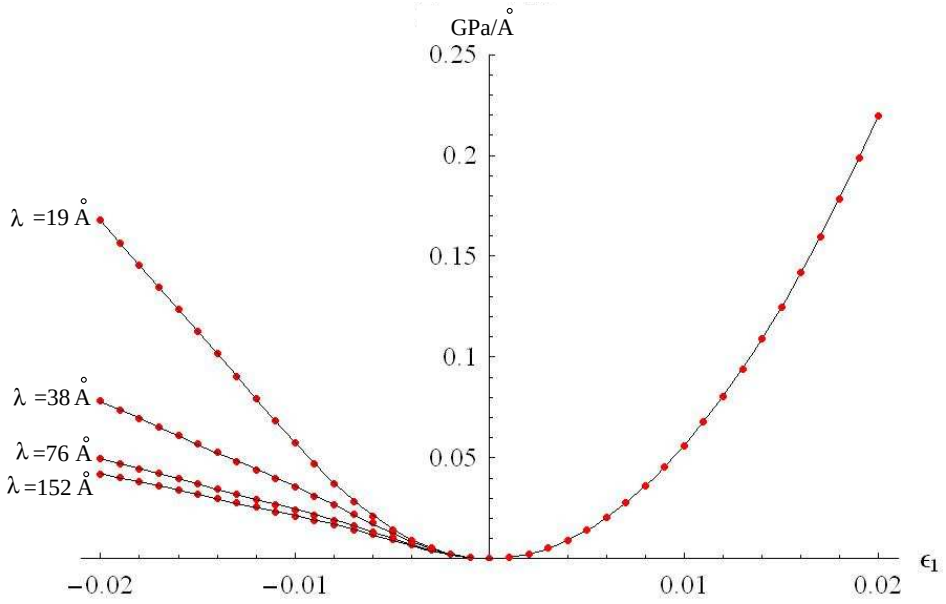

Figure 3.19: The formation energy per unit volume with respect to strain increments ε_1 along the $[1\bar{2}10]$ direction for the different unitcells shown in Figure 3.18. The linear behavior in the compression region is due to the plane bending. The respective fitting values represent the mesoscale elastic constant C_{11}^M.

vectors $\vec{\varepsilon}$ to the following perfect lattice parameters:

$$\begin{pmatrix} a_1 \\ a_2 \\ a_3 \end{pmatrix} = \begin{pmatrix} 8 \cdot a_0 \cdot (64 - n_{atom}) & 0 & 0 \\ 0 & \sqrt{3} \cdot a_0 & 0 \\ 0 & 0 & c_0 \end{pmatrix} \tag{3.146}$$

Under strain the primitive vectors a_i are transformed into the new lattice vectors a_i' b,y:

$$\begin{pmatrix} a_1' \\ a_2' \\ a_3' \end{pmatrix} = \begin{pmatrix} a_1 \\ a_2 \\ a_3 \end{pmatrix} (I + \varepsilon) \tag{3.147}$$

where I is the identity matrix and ε is the strain tensor:

$$\varepsilon = \begin{pmatrix} \varepsilon_1 & \frac{1}{2}\varepsilon_6 & \frac{1}{2}\varepsilon_5 \\ \frac{1}{2}\varepsilon_6 & \varepsilon_2 & \frac{1}{2}\varepsilon_4 \\ \frac{1}{2}\varepsilon_5 & \frac{1}{2}\varepsilon_4 & \varepsilon_3 \end{pmatrix} \tag{3.148}$$

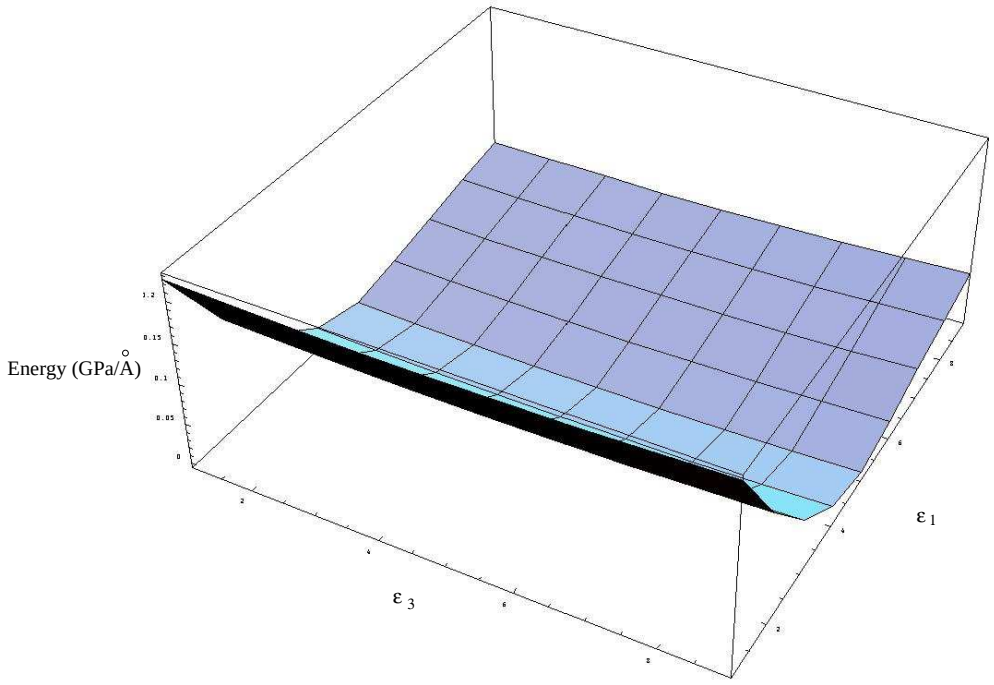

Figure 3.20: The formation energy per unit volume with respect to the strain increments ε_1 and ε_3 for the unitcell with lengh $L_x = 76$ Å. The respective fitting values represent the mesoscale elastic constant C_{13}^M.

the latter tensor is linked with the strain vector by: $\vec{\varepsilon} = (\varepsilon_1, \varepsilon_2, \varepsilon_3, \varepsilon_4, \varepsilon_5, \varepsilon_6)$. Then the mesoscale elastic constants C_{ij}^M are found by appling different strains components ε_i to the perfect lattice parameters. The strain chosen are 21 ranging between ± 0.02 with increment 0.001.
For the mesoscale elastic constants C_{11}^M and C_{33}^M the only non-zero strain components are ε_1 and ε_3, respectively. In Figure 3.19 the *ab-initio* results (red points) are compared with the meso-elastic theory previously developted (black curves). Like in graphene the agreement between the two theoretical approaches is excellent.
By fitting the respective *ab-initio* data with a polynomial functions of 10^{th}-order[12] I have found the respective mesoscale elastic constant.
I observe that the critical strain tend to decrease as I increase the length L_x until the value 76 Å. For longer L_x the critical strain $\varepsilon_{critical}$ remain fixed to the convergent value of 0.0026. This is the main different between the graphite and the graphene case.

[12] Test calculations shown that the fitting are well well convergent.

L_x	C_{11}	C_{12}	C_{33}	C_{13}	C_{44}
19 Å	1105	182	30.5	−2.3	4.8
38 Å	1043	172	31.0	2.8	4.8
76 Å	1040	171	31.2	4.5	4.8
152 Å	1040	171	31.2	4.5	4.8

Table 3.8: The resulting Mesoscale elastic constant with respect to the length L_x. In the first row (L_x=19 Å) the graphite plane are always flat and the mesoscale elasticity degenerate into the classical elasticity. For larger length L_x the planes when compressed tend to bend introducing the mesoscale elastic constant. The respective mesoscale elastic constant are convergent for length larger that 76 Å.

In graphene the critical strain $\varepsilon_{critical}$ decrease monotonically as we increase the length L_x.
In graphite after a length value of $L_x = 76$ Å the disregistry energy become predominant and freeze the critical strain to a fixed value of 0.0026. Further due to the frozen critical strain also the respective mesoscale elastic constant remain fixed after for unitcell longer than $L_x = 76$ Å.
The resulting mesoscale elastic constant C_{11}^M drop from 1104 GPa (*classical* elastic constant, *i.e.* flat plane) to convergent value 1040 GPa. I observe that both the values are in agreement with the experiment (1080 ± 20 GPa). The reason why C_{11}^M does not change appreciably is because is even-order elastic terms. The linearty behavior due to the bending is mainly given by the odd-order terms of the strain energy (C_{111}, C_{11111}...).
The mesoscale elastic constant C_{33}^M slightly increase from 30.6 GPa (*classical* elastic constant, *i.e.* flat plane) to the convergent value 31.2 GPa. This slightly changing is reflecting a weak plane bending when the c-axis expand.
For the C_{44}^M the only non-zero strain component is ε_5. In this case the planes are always flat and the resulting mesoscale elastic constant degenerate into the corresponding *classical* value C_{44}^M=C_{44}.
Figure 3.20 show the strain energy with respect the strain components ε_1, ε_3. This energy surface is fitted by a polynomial functions in two variables (ε_1, ε_3) and the reulting coefficient term $\varepsilon_1 \cdot \varepsilon_3$ is the C_{13}^M mesoscale elastic constant. The values found are negative when the plane is flat (under the critical strain) and they become positive above the critical strain with the convergent value +4.52 GPa (see Table 3.8). The agreement with the revised experimental value is perfect (7.9 ± 3.5 GPa).
Finally the elastic constant C_{12}^M is found using the meso-elastic theory with the following strain vector $\overrightarrow{\varepsilon} = (\varepsilon_1, \varepsilon_2, 0, 0, 0, 0)$. As for C_{11}^Mcase, the corre-

sponding value drop from 182 GPa to the convergent value 171 GPa, both in agrement with revised experimental value (180 ± 20).

Conclusion

In this thesis I have proposed two novel theories concerning the mechanical properties of silicon carbide and graphite.
The first theory is a milestone on the road to implementing robust, high performance SiC devices while the second theory has profound implications for the new field of graphite/graphene science.

- Theory of the Dislocation Glide Enhancements in Silicon Carbide

In this work, I have investigated the dislocation core effect on electrical activity and kink migration. I have shown that the symmetric reconstructions along the dislocation line are always electrically active and have glide activation energies lower than the respective asymmetric reconstructions.
Further, I have proposed a theoretical model, which can explain in details all the following experimental evidence:

1. Why under forward bias the dislocations can be electrically active:

Under electron-hole plasma injections (*i.e.* under forward bias), the free energy of the SR dislocations is dynamically lowered by continuous electron-hole transitions between the respective deep levels and valence/conduction

2. Why the 90° partials are immobile while the 30° partials can move:

To stabilize the SR 90° partials, a shear between the unfaulted and stacking fault regions along the dislocation line is required, while for the 30° partials the AR does not require a long ranged shear, but rather only requires flipping of alternate atoms in the core. Therefore, only for the 30° partials does the SR dislocation line becomes more stable than the AR with a strong dynamic charge screening provided by the continuous electron hole plasma injections. The deep levels provided by the SR are dynamically positive (hole recombination) and negatively (electron recombination) charged.
However, the strong charge screening of the dislocation line surrounded by electron-hole plasma freezes the deep levels inside the band gap, *i.e.* the

30° partial deep levels correspond to the respective neutral band structures. Therefore, both the 30° partials can provide band-gap level deep enough as required by the REDG mechanism.

3. Why only the Si(g) 30° dislocations move:

The band structure analysis have shown that both the 30° partials allow electrical transitions of indirect type, *i.e.* with electron-phonons coupling. These transitions can involve the creation of phonons at different points of the Brillouin zone. I have suggested that the reason why only the Si(g) 30° dislocations are mobile under electron-hole plasma injection is due to the different kind of phonons created that could hinder (for the C(g) 30° dislocations) or increase (for the Si(g) dislocations) the stability of the SR dislocation line.
The same reason explains why the radiative transition rate on the Si(g) dislocations is higher than the corresponding C(g) dislocations.

In conclusions this model can be applied to any semiconductor materials in order to predict the behaviour under electron-hole plasma and could inspire new experimental technique to reduce the degradation mechanism.

- Mesoscale elasticity in graphene/graphite material

In this study I have determinate the *classical* third- and second-order elastic constants. In agreement with previous theoretical studies I have found that the C_{13} elastic constant has a negative values in strongly disagreement with the positive value found experimentally.
The common opinion is that theory fail because does not include an important part of the physical interaction between layers, the van der Waals interaction and therefore should not be relied upon.
Contradicting this belief, I have demonstrated that theory performs excellently for graphite and reproduces with precision the all elastic properties.
I have developted a mathematical theory beyond the harmonic approximation that describe the elastic behaviour of graphite/graphene. Further I have confirmed this theory via density functional calculations.
I have shown that under compression graphite tends to bend and these bending modes introduce a new class of elastic constants, called *mesoscale elastic constants*, which reproduce with great accuracy the respective experimental values.
Therefore the elastic constants measured experimentally are the mesoscale elastic constants (the constants that really describe the elastic behaviour

of graphite), while the elastic constants determinate via *ab-initio* methods are the real (and common) elastic constants. The mesoscale elasticity in principle should extend to all the layered-materials.

List of Publications

- **Referred Articles:**

1. First Principles Simulations of Boron Diffusion in Graphite
   I. Suarez-Martinez, A.A. El-Barbary, G. Savini, and M.I. Heggie
   Physical Review Letter **98**, 015501 (2007)

2. Electrical Activity and Migration of 90° Partial Dislocations in SiC
   G. Savini, M. I. Heggie, S. Öberg and P. R. Briddon
   New Journal Physics **9**, 6 (2007)

3. Dislocations in Carbon Nanotube Walls
   Irene Suarez-Martinez, Gianluca Savini, Alberto Zobelli, Malcolm Heggie
   Journal of Nanotechnology and Nanomaterials, in press

4. Core structures and Kink Migrations of Partial Dislocations in 4H-SiC
   Gianluca Savini, Malcolm I Heggie and Sven Öberg
   Faraday Discussion 134, 353-367 (2007)

5. Scanning Electron Microscopy of Dopant distribution in Semiconductors
   P. G. Merli, V. Morandi, G. Savini, M. Ferroni and G. Sberveglieri
   Applied Physics Letters 86, 101916 (2005)

- **Referred Conference Articles:**

1. Dislocations of Burgers vector $c/2$ in Graphite
   I. Suarez-Martinez, G. Savini, G. Haffenden, J.-M. Campanera and M. I. Heggie
   Physica Status Solidi C, in press

2. Structure and Energy of Partial Dislocations in Wurtzite-GaN
   G. Savini, A. T. Blumenau, M. I. Heggie, and S. Öberg
   Physica Status Solidi C, in press

3. Theory of Partial Dislocations in SiC
   G. Savini Physica Status Solidi C, in press

4. Partial dislocations under Forward Bias in SiC
   G. Savini, A.A. El-Barbary, M.I. Heggie and S. Öberg
   Mater Science Forum, in press

5. First Principles Modelling of Scroll-to-Nanotube Defect: Screw-type Dislocation
   I. Suarez-Martinez, G. Savini and M.I. Heggie Materials Science Forum Vols. 527-529 pp. 1583-1586 (2006)
   Peierls Barriers and Core Properties of Partial Dislocations in SiC

6. Peierls Barriers and Core Properties of Partial Dislocations in SiC
   G. Savini, M.I. Heggie and S. Öberg
   Materials Science Forum Vols. 527-529 pp. 359-362 (2006)

7. Structure and Energy of the 90° Partial Dislocations in Wurtzite-GaN
   G. Savini, M.I. Heggie, C.P. Ewels, N. Martsinovich, R. Jones and A.T. Blumenau
   Materials Science Forum Vols. 483-485 pp. 1057-1061 (2005)

8. Combined HREM and Theoretical Analysis of SiC/Si Interfaces
   V. Grillo, S. Frabboni, G. Cicero, G. Savini and A. Catellani
   Inst. Phys. Conf. Ser. No 180, 69-72 (2004)

- **Book Chapter**

1. Irradiation Damage in Graphite from First Principles
   M.I. Heggie, I. Suarez-Martinez, G. Haffenden, G. Savini, A.A. El-Barbary, C. Ewels, R. Telling, C. Cousins
   Ageing Management of Graphite Reactor Cores. Edited by G.B. Neighbour, 342-363 (2006)

- **Others:**

1. Epitaxial Metallic Island: Charge Confinement and Template for Atomic Wires
   A.M. Mazzone, G. Savini Symposium T: Self-Organized Processes in Semiconductor Heteroepitaxy, MRS Proc. 794, pages 17-22, T3.5 (2004)

2. Theoretical Investigation of Si/SiC Interfaces
   G. Cicero, A. Catellani and G. Savini
   III SiC Workshop, Palazzo Einaudi, Chivasso (Torino)

- **Articles in preparation:**

1. Mesoscale Elastic Constant in Graphite
   G. Savini, M.I. Heggie *et al*

2. Radiation Damage in Graphite: a New Model
   M.I. Heggie, I. Suarez-Martinez, G. Savini, G.L. Haffenden, J.M. Campanera

3. Density Functional Calculations on the intricacies of the Moiré Patterns
   J. M. Campanera, G. Savini, I. Suarez-Martinez, and M. I. Heggie

4. SuperScrew Dislocation in Graphite
   I. Suarez-Martinez, G. Savini and M.I. Heggie

List of Publications

- **Talks:**

1. Elasticity Theory of Hexagonal Graphite
   Aimpro Meeting 2006 25-26 January 2006, University of Exeter, Exeter, UK
2. Core Structure and Kink Migrations of Partial Dislocations in 4H-SiC
   Faraday Discussion 134: Atomic Transport and Defect Phenomena in Solids 10-12 July, University of Surrey, Guildford, UK
3. The Elasticity of Hexagonal Graphite via Aimpro Carbon 2006
   The International Carbon Conference 16-21 July 2006, The Robert Gordon University, Aberdeen, Scotland
4. Theory of Partial Dislocation in SiC Extended Defects in Semiconductors EDS 2006 17-22 September 2006, Halle, Germany
5. Enhancement of the Dislocation Velocity in Semiconductors (Invited Talk)
   HPC User Meeting 01 December 2006, London, UK
6. Mesoscale Elastic Constants in Graphite
   Aimpro Meeting 2006 12-14 December 2006, University of Exeter, Exeter, UK
7. Elastic Properties in Graphite
   Ageing Management of Graphite Reactor Cores 2007, 14 February 2007, Manchester, UK
8. Mesoscale Elastic Constants in Graphite (Invited Talk)
   NanoTech Insight 2007 10-17 March 2007, Luxor, Egypt

- **Prizes:**

1. HPC Prizes 2006 in the category Novel Research
   for: "Enhancement of the Dislocation Velocity in Semiconductors"

Acknowledgements

First I would like to thank my wife Erminia for her patience and support during all these years.

Secondly, I would like to thank all my supervisors Prof. Anna Cavallini, Prof. Malcolm Heggie, Dr. Pier Giorgio Merli and Prof. Giulio Pozzi for their strong support over all these years.

I wish also to thank my family which have been supporting and root for me. A special thank to my grandmother Angiulina for her love and strength.

I would like to thank all my friends, each one supporting and accompanied me in these years in their own way:
Franco Corticelli (the cow), Irene (the boss), Gemma (the smile), Ahlam, Chris Ewels, Campanera, Peter, Ewan Main (the Irish) and Leonardo (the good).
Finally, I will play my "joker" or "wild card": since there are so many I would like to acknowledge, I shall acknowledge one, a very special person who shall remain anonymous here, but whose identity shall be revealed by me from time to time.

Bibliography

[1] M. Stoneham, *Defects in Solids*, Oxford University press, London (1975).

[2] E.K.U. Gross, R.M. Dreizler, *Density Functional Theory*, Nato ASI Series N, Vol. 37 (1985).

[3] P.R. Briddon and R. Jones, *Phys.Status Solidi B*, 2000, **217**, 131.

[4] O. Gunnarsson, M. Jonson, B.I. Lundqvist *Phys. Rev. B* **20**, 3136 (1979).

[5] O. Gunnarsson, B.I. Lundqvist *Phys. Rev. B* **13**, 4274 (1976).

[6] M. Stoneham, *Defects in Solids*, Oxford University press, London (1975).

[7] E.K.U. Gross, R.M. Dreizler, *Density Functional Theory*, Nato ASI Series N, Vol. 37 (1985).

[8] P.R. Briddon and R. Jones, *Phys.Status Solidi B*, 2000, **217**, 131.

[9] O. Gunnarsson, M. Jonson, B.I. Lundqvist *Phys. Rev. B* **20**, 3136 (1979).

[10] O. Gunnarsson, B.I. Lundqvist *Phys. Rev. B* **13**, 4274 (1976).

[11] **F. A.** Stahl, *Am. J. Phys.* **71**, 1170 (2003).

[12] H. Morkoc¸ , S. Strite, G. B. Gao, M. E. Lin, B. Sverdlov and M. Burns, *J. Appl. Phys.* **76**, 1363 (1994).

[13] J. P. Bergman, H. Lendenmann, P. Ú . Nilsson, U. Lindefeldt and P. Skytt, *Mater. Sci. Forum* **299**, 353-356 (2001).

[14] A. Galeckas, J. Linnros and P. Pirouz, *Appl. Phys. Lett.* **81**, 883 (2002).

[15] S. Ha, M. Skowronski, J. J. Sumakeris, M. J. Paisley and M. K. Das, *Phys. Rev. Lett.* **92**, 175504 (2004).

[16] M. H. Hong, A. V. Samant and P. Pirouz, *Philos. Mag. A* **80**, 919 935 (2000).

[17] J. Q. Liu, M. Skowronski, C. Hallin, R. So¨ derholm and H. Lendenmann, *Appl. Phys. Lett.* **80**, 749 (2002).

[18] S. Ha, K. Hu, M. Skowronski, J. J. Sumakeris, M. J. Paisley and M. K. Das, *Appl. Phys. Lett.* **84**, 5267 (2004).

[19] S. Ha, M. Skowronski and H. Lendenmann, *J. Appl. Phys.* **96**, 393 (2004).

[20] A. Galeckas, J. Linnros and P. Pirouz, *Phys. Rev. Lett.* **96**, 025502 (2006).

[21] S. I. Maximenko, P. Pirouz and T. S. Sudarshan, *Appl. Phys. Lett.* **87**, 033503 (2005).

[22] S. Ha, M. Benamara, M. Skowronski and H. Lendenmann, *Appl. Phys. Lett.* **83**, 4957 (2003).

[23] M. Skowronski, J. Q. Liu, W. M. Vetter, M. Dudley, C. Hallin and H. Lendenmann, *J. Appl. Phys.* **92**, 4699 (2002).

[24] M. E. Twigg, R. E. Stahlbush, M. Fatemi, S. D. Arthur, J. B. Fedison, J. B. Tucker and S. Wang, *Appl. Phys. Lett.* **82**, 2410 (2003).

[25] P. Pirouz, M. Zhang, J. L. Demenet and H. M. Hobgood, *J. Appl. Phys.* **93**, 3279 (2003).

[26] J. D. Weeks, J. C. Tully and L. C. Kimerling, *Phys. Rev. B* 12, 3286 (1975).

[27] H. Sumi, *Phys. Rev. B* **29**, 4616 (1984).

[28] K. Maeda, S. Takeuchi, in *Dislocation in Solids*, ed. F. R. N. Nabarro and M. S. Duesbery, North-Holland, Amsterdam vol. 10, pp. 443-504 (1996).

[29] A. T. Blumenau, C. J. Fall, R. Jones, S. Öberg, T. Frauenheim and P. R. Briddon, *Phys. Rev. B* **68**, 174108 (2003).

[30] J. P. Perdew and Y. Wang, *Phys. Rev. B* **45**, 13244 (1992).

[31] P. R. Briddon and R. Jones, *Phys. Status Solidi B* **217**, 131 (2000).

[32] C. Hartwigsen, S. Goedecker and J. Hutter, *Phys. Rev. B* **58**, 3641 (1998).

[33] H. J. Monkhorst and J. D. Pack, *Phys. Rev. B* **13**, 5188 (1976).

[34] G. L. Harris, in *Properties of Silicon Carbide*, ed. G. L. Harris, Institution of Electrical Engineers, London, U.K. **4** (1995).

[35] M. M. de Araújo, J. F. Justo and R. W. Nunes, Appl. Phys. Lett. **85**, 5610 (2004).

[36] D. B. Laks, C. G. Van de Walle, G. F. Neumark, P. E. Blöchl and S. T. Pantelides, *Phys. Rev. B* **45**, 10965 (1992).

[37] F. Bernardini and L. Colombo, *Phys. Rev. B* **72**, 085215 (2005).

[38] J. P. Hirth and J. Lothe, Theory of Dislocations, Wiley, New York, 2nd edn p. 244. (1982).

[39] G. M. Amulele, M. H. Manghnani, B. Li, D. J. H. Errandonea, M. Somayazulu and Y. Meng, *J. Appl. Phys.* **95**, 1806 (2004).

[40] S. Karmann, R. Helbig and R. A. Stein, *J. Appl. Phys.* **66**, 3922 (1989).

[41] N. Oyama and T. Ohno, *Phys. Rev. Lett.* **93** 195502 (2004).

[42] U. Lindefelt, H. Iwata, S. Öberg and P. R. Briddon, *Phys. Rev. B* **67**, 155204 (2003).

[43] M. S. Miao, S. Limpijumnong and W. R. L. Lambrecht, *Appl. Phys. Lett.* **79**, 4360 (2001).

[44] M. I. Heggie and R. Jones, *Philos. Mag. B* **48**, 365 (1983).

[45] M. I. Heggie, R. Jones and A. Umerski, *Phys. Status Solidi A* **138**, 383 (1993).

[46] R. W. Nunes, J. Bennetto and D. Vanderbilt, *Phys. Rev. Lett.* **77**, 1516. (1996).

[47] C. P. Ewels, S. Leoni, M. I. Heggie, P. Jemmer, E. Hernández, R. Jones and P. R. Briddon *Phys. Rev. Lett.* **84**, 690 (2000).

[48] J.M. Campanera, G. Savini, I. Suarez-Martinez, M.I. Heggie, Physical Review B, To be submitted

[49] B.T. Kelly, *Physics of Graphite*, (Applied Science Publishers 1981)

[50] M. S. Dresselhaus, M. Endo, Carbon Nanotubes, Synthesis, Structure, Properties and Applications, vol. **80**, (Springer publishers, 2000)

[51] P.L. Walker, *Chemistry and Physics of Carbon*, vol. **2** (Edward Arnold Ltd. , London 1966).

[52] A.R. Ubbelohde and F.A. Lewis, *Graphite and its Crystal Compouds* (Clarendon Press, Oxford 1960).

[53] C. Baker and A. Kelly, *Phil. Mag.* **9**, 927 (1964).

[54] R.H. Telling and M.I. Heggie, *Phil. Mag.* **83**, 411 (2003).

[55] J.-C. Charlier, T.W. Ebbesen and P. Lambin, *Phys. Rev. B.* **53**, 11108, (1996).

[56] O.L. Blakslee, C.G. Proctor, E.J. Seldin, G.B. Spence, T. Weng, *J. Appl. Phys.* **41**, 3373 (1970).

[57] M. Grimsditch, Phys. Status Solidi B **193**, K9 (1996).

[58] M. Grimsditch, J. Phys. C **16**, L143 (1983).

[59] S.A. Lee, S.M. Lindsay, Phys. Status Solidi B, **157**, K83 (1990).

[60] You Xiang Zhao and I.L. Spain, Phys. Rev. B. **40**, 993 (1989).

[61] J.C. Boettger, *Phys Rev B* **55**, 11202 (1997)

[62] PhD Cousin

[63] R.W. Lynch and H.G. Drickamer, *J. Chem. Phys.* 44, **181** (1986).

[64] S. Morita, S. Tsukada and N. Mikoshiba, *J. Vac. Sol. Technol. A*, vol. **6**, No. 2 (1988).

[65] J.D. Bernal, *Proc. R. Soc. London Ser. A* **106**, 749 (1924).

[66] L. Samuelson and I.P. Batra. *J. Phys. C* **13**, 5105 (1980)

[67] J.-C. Charlier, J.-P. Michenaud, Ph. Lambin, *Phys Rev B* **46**, 8, 4540 (1992)

[68] N. Mounet, N. Marzari, *Phys Rev B* **71**, 205214 (2005)

[69] J.C. Boettger, *Phys Rev B* **55**, 11202 (1996).

[70] M.T. Yin, M.L. Cohen, *Phys Rev B* **29**, 6996 (1984).

[71] S.B. Trickey, F. Muller-Plathe, G.H.F. Diercksen, J.C. Boettger, *Phys Rev B* **45**, 4460 (1992).

[72] M. Hasegawa, K. Nishidate, *Phys Rev B* **70**, 205431 (2004).

[73] H.J.F. Jansen, A.J. Freeman, *Phys Rev B* **35**, 8207 (1987).

[74] C.S.G. Cousins, M.I. Heggie, *Phys Rev B* **7**, 024109 (2003).

[75] C. Baker and A. Kelly, *Phil. Mag.* **9**, 927 (1964).

[76] J.P. Perdew and Y. Wang, *Phys. Rev. B*, 1992, **45**, 13244.

[77] P.R. Briddon and R. Jones, *Phys.Status Solidi B*, 2000, **217**, 131.

[78] C. Hartwigsen, S. Goedecker and J. Hutter, *Phys. Rev. B*, 1998, **58**, 3641.

[79] H. J. Monkhorst and J. D. Pack, *Phys. Rev. B*, 1976, **13**, 5188.

[80] M. Hanfland, H. Beister, and K. Syassen, *Phys. Rev. B*, 1976, **13**, 5188.

[81] Y. Baskin, L. Meyer, *Physical Review* **2**, 544 (1955).

[82] K.S. Novoselov, A.K. Geim, S. V. Morozov, D. Jiang, Y. Zhang et al. Science **306**, 666-669 (2004).

[83] J.C. Mayer, A.K. Geim, M.I. Katsnelson, K.S. Novoselov, T.J. Booth, S. Roth, Nature **446**, 60-63 (2007)

[84] J.P. Perdew and Y. Wang, *Phys. Rev. B*, 1992, **45**, 13244.

[85] P.R. Briddon and R. Jones, *Phys.Status Solidi B*, 2000, **217**, 131.

[86] C. Hartwigsen, S. Goedecker and J. Hutter, *Phys. Rev. B*, 1998, **58**, 3641.

[87] H. J. Monkhorst and J. D. Pack, *Phys. Rev. B*, 1976, **13**, 5188.